RICE UNIVERSITY

A Search for the Lightest Supersymmetric Partner of the Top Quark at DØ

by

Dennis S. Mackin, Jr.

A THESIS SUBMITTED
IN PARTIAL FULFILLMENT OF THE
REQUIREMENTS FOR THE DEGREE

Doctor of Philosophy

Approved, Thesis Committee:

Marjorie D. Corcoran, Chair
Professor of Physics and Astronomy

B. Paul Padley
Professor of Physics and Astronomy

David W. Scott
Noah Harding Professor of Statistics

Houston, Texas

August 2010

Abstract

We report the result of a search for the pair production of the lightest supersymmetric partner of the top quark ($\tilde{t}_1$) in 5.4 ± 0.3 fb^{-1} of data from the DØ detector at a $p\bar{p}$ center-of-mass energy of 1.96 TeV at the Fermilab Tevatron collider. The scalar top quarks are assumed to decay into a b quark, a charged lepton and a scalar neutrino ($\tilde{\nu}$), and the search is performed in the electron plus muon final state. No significant excess of events above the standard model prediction is detected and new exclusion limits at the 95% C.L. are set for a portion of the ($m_{\tilde{t}_1}$,$m_{\tilde{\nu}}$) mass plane.

Contents

List of Figures

List of Tables

Chapter 1

The Standard Model, the Fine Tuning Problem, and Supersymmetry

In this chapter, we will start by giving an overview of the Standard Model of Fundamental Particles and Interactions (SM) with an emphasis on aspects that are relevant to our search. Next, we will explain the Fine-tuning Problem and show how Supersymmetry could provide a natural solution. Finally, we discuss the Minimal Supersymmetric Standard Model and the scalar partner of the top quark.

1.1 The Standard Model

We describe the basic properties of the strong, weak, and electromagnetic forces using the group structure of the Standard Model, $SU(3)_c \times SU(2)_L \times U(1)_Y$. We then describe the properties of the matter particles, quarks and leptons. Finally, we explain how their properties and interactions are related to the group structure.

1.1.1 Strong Force

The strong force–also known as the color force since its three charge types are labeled red, green, and blue–is carried by the gluon, a spin 1, zero mass particle, and only affects quarks and the gluons themselves. The strength of the coupling between particles decreases as particles get closer together, a characteristic called asymptotic freedom [2]. When the particles move apart, the potential energy between them grows. Eventually, the particles either move back toward each other or the potential energy of the system reaches an unstable level and is spontaneously converted into new strongly interacting particles which then bind with the originals. This process, called hadronization, ensures quarks and gluons are always bound. The observed bound states are three quark and quark/anti-quark states known as baryons and mesons respectively, hadrons collectively. There have been claims that exotic hadrons have been observed, but none of the claims have been widely accepted. Due to hadronization, we do not detect individual quarks or qluons, known collectively as "partons". Instead, we detect "hadronic jets", cone shaped sprays of hadrons and their decay products [3]. Protons, quark content uud, and neutrons, quark content udd, are the most common baryons. The strong force is described by the group $SU(3)_c$, the group of all 3×3 unitary matrices with determinant equal to one. $SU(3)_c$ is non-Abelian which leads to gluon/gluon self interaction which produces asymptotic freedom[4].

1.1.2 The Electro-weak Force

At high energies, $\mathcal{O}(100\ \mathrm{GeV/c^2})$, the electromagnetic and weak forces are described in a unified fashion are called the electro-weak force. The characteristics of the electro-weak force are described by its group structure, $SU(2)_L \times U(1)_Y$. $SU(2)_L$ is known as weak isospin and its fundamental representation is the weak isospin doublet. The subscript $_L$ indicates that

weak isospin only operates on left chiral fermions. Fermions have four degrees of freedom, particle/anti-particle and two spin states. The two spin degrees of freedom correspond to chirality values ± 1[1] [5]. Like the group $SU(3)$, $SU(2)$ is non-Abelian and the electro-weak bosons interact with themselves. The group $U(1)_Y$ describes Weak hypercharge which is defined as

$$Q = T_3 + \frac{Y}{2} \tag{1.1}$$

where Q is the electromagnetic charge and T_3 is isospin charge with the values $\pm\frac{1}{2}$ for left chiral fermions and 0 for right chiral fermions [4]. The three generators of the group $SU(2)$ represent the two charged and one neutral weak isospin boson, which we label W^1,W^2, and W^3. The one generator of the group $U(1)$ represents the weak hypercharge boson, B. Electroweak unification combines these four bosons to produce the SM bosons $W^{\pm}$, Z, and γ, the photon. The charged bosons $W^{\pm}$ are given by the mixture

$$W^{\pm} = \sqrt{\frac{1}{2}}\left(W^1 \mp W^2\right) \tag{1.2}$$

and couples only to left handed fermions. The two neutral bosons are given by the mixture of the neutral weak isospin and hypercharge bosons:

$$\gamma = B\cos\theta_W + W^3 \sin\theta_W \tag{1.3}$$

$$Z = -B\sin\theta_W + W^3\cos\theta_W \tag{1.4}$$

[1]Helicity is determined by projecting a particles spin into its direction of motion. If the spin and the direction of motion are parallel, the particle is given helicity value 1. If the directions are anti-parallel, then the helicity is given the value -1. For massless particles, helicity and chirality are equivalent. For massive particles, helicity depends on the frame of reference, while chirality is Lorentz invariant[5]. We avoid use of the terms left-handed and right-handed because they can refer to chirality or helicity.

where θ_W, is the electro-weak mixing angle[4]. $\sin^2\theta_W = 0.23$ for interactions with momentum transfer equal to the mass of the Z boson, 91.2 GeV/c^2 [6]. The properties of the SM bosons are summarized in Table 1.1.

Bosons (spin=1)			
symbol	**force**	**mass** (GeV/c^2)	**charge**
γ (photon)	Electromagnetic	0	0
W-	weak	80.4	-1
W+	weak	80.4	+1
Z	weak	91.2	0
g (gluon)	strong	0	0

Table 1.1: The Standard Model force carrying bosons with their charges and masses. The common particle names are given in parentheses where appropriate.

1.1.3 Quarks and Leptons

Matter particles are divided into two classes, quarks and leptons, which both have anti-matter analogs. Quarks have three generations and each generation has an up type and down type. The generations have the same quantum numbers but successive generations have more massive particles, see Table 1.2. In some cases, most notably the case of the top quark, the extra mass significantly changes the properties of the quark. All quarks interact strongly and with the neutral Z and γ bosons. Right chiral quarks (left chiral anti-quarks) form weak isospin singlets. The up and down type, left chiral quarks (right chiral anti-quarks) for each generation form weak isospin doublets. The weak isospin eigenstates of the quarks are a mixture of the mass eigenstates:

$$\begin{pmatrix} d' \\ s' \\ b' \end{pmatrix} = \mathbf{U} \begin{pmatrix} d \\ s \\ b \end{pmatrix} \tag{1.5}$$

where **U**, know as the CKM (Cabibbo-Kobayashi-Maskawa) matrix, is a 3×3 unitary matrix characterized by three mixing angles and one complex phase. The parameters of the CKM matrix are not specified by the SM but must be measured experimentally [5]. The SM quarks and their masses are listed in Table 1.2.

There are also three generations of leptons, see Table 1.2. Left chiral leptons (right chiral anti-leptons) form weak isospin doublets of a charged and a neutrino type lepton. Right chiral (left chiral anti-leptons) charged leptons form isospin singlets[4]. Right chiral neutrinos (left chiral anti-neutrinos) are not in the Standard Model and may not exist[2]. Since leptons do not interact strongly, their color quantum number is zero. Neutrinos also have electromagnetic charge zero, which means that they only interact weakly. Thus, they are difficult to detect and escape detection at the DØ detector.

Quarks (spin=$\frac{1}{2}$)		
generation	**mass** (GeV/c^2)	**charge**
u (up)	0.003	2/3
d (down)	0.006	-1/3
c (charm)	1.3	2/3
s (strange)	0.1	-1/3
t (top)	172.0	2/3
b (bottom)	4.3	-1/3

Leptons (spin=$\frac{1}{2}$)		
flavor	**mass** (GeV/c^2)	**charge**
e (electron)	0.000511	-1
ν_e	$< 1^{-8}$	0
μ (muon)	0.106	-1
ν_μ	< 0.0002	0
τ (tau)	1.7771	-1
ν_μ	< 0.02	0

Table 1.2: The Standard Model fermions with their charges and masses. The common particle names are given in parentheses where appropriate.

1.2 The Fine-tuning Problem

In the Standard Model the Z and $W^{\pm}$ bosons get their mass through the Higgs Mechanism[5], proposed in 1964 by Peter Higgs and others [7][8][9]. It is also possible that the the Standard Model fermions get their mass through their interactions with the Higgs field [10]. However,

[2]Because neutrinos are known to have mass, right helicity neutrinos do exist, at least in some reference frames.

the Higgs Mechanism has two particularly troubling problems. The first is that the associated Higgs boson has yet to be detected. The second is the Fine-tuning problem [11], which we describe here.

From searches for the Standard Model Higgs boson and precision measurements of the electro-weak parameters, the mass of the Higgs boson is expected to be less than 200 GeV/c^2 [12]. In the Standard Model the mass of the Higgs boson is

$$m_H = \nu\sqrt{\frac{\lambda}{2}} \tag{1.6}$$

where $\nu/\sqrt{2}$ is the Higgs field vacuum expectation value and λ is the Higgs self interaction strength [13]. Fermion loops, see Figure 1.1, produce corrections to the Higgs mass, δm_H^2,

$$\delta m_H^2 = -2N(f)\lambda_f^2 \int \frac{d^4k}{(2\pi)4}\left[\frac{1}{k^2 - m_f^2} + \frac{2m_f^2}{(k^2 - m_f^2)^2}\right] \tag{1.7}$$

where $N(f)$ is 1 for leptons and 3 for quarks, λ_f is the Higgs/fermion interaction strength, k is the four momentum, and m_f is the mass of the fermion [14][15]. The first term in this correction is quadratically divergent. Applying a cut-off to the integral such as the reduced Plank mass, $\Lambda_{mp} = 2.4 \times 10^{18}$ GeV/c^2, gives an integral which is finite

$$\delta m_H^2 = -2N(f)\lambda_f^2 \int^{\Lambda_{mp}} \frac{d^4k}{(2\pi)4}\left[\frac{1}{k^2 - m_f^2} + \frac{2m_f^2}{(k2 - m_f^2)^2}\right]. \tag{1.8}$$

However, this approach requires agreement between the uncorrected Higgs boson mass and the correction to the first 30 significant digits. Requiring such agreement seems to be an unnatural fine-tuning and, therefore this problem is known as the fine-tuning problem [13].

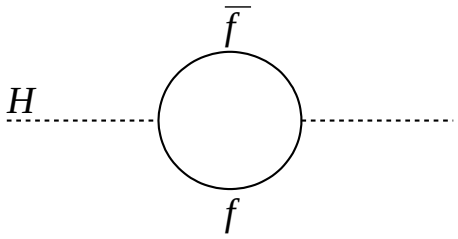

Figure 1.1: Fermion loop correction to the Standard Model Higgs boson self energy.

1.3 Supersymmetry

Supersymmetry (SUSY) [16] is a class of theories which pair Standard Model (SM) particles with partner particles that differ in spin by $\frac{1}{2}$ but have otherwise identical quantum numbers. Thus, standard model fermions have spin zero, or "scalar", partners and the partners of the SM bosons have spin $\frac{1}{2}$[13]. The scalar partners of the SM fermions also contribute to the Higgs self energy, see Figure 1.2. The correction from the scalar term has the form

$$\delta m_H^2 = -N(f)\tilde{\lambda}_f \int \frac{d^4k}{(2\pi)^4} \left[\frac{1}{k^2 - m_{\tilde{f}}^2}\right] + ... \tag{1.9}$$

which is again quadratically divergent. The ellipsis replaces the terms which are not divergent. The scaler and vector couplings are expected to differ in sign such that [14]

$$\tilde{\lambda}_f = -\lambda_f^2. \tag{1.10}$$

Therefore, the quadratic divergences from the fermion and scalar loops cancel. Because of this cancelation, SUSY extensions to the Standard Model provide more natural solutions to the fine-tuning problem. It turns out that the cancelation is not perfect because the symmetry is "broken"; the particles and their partners have different masses [13]. The SUSY particles, with the exception of the supersymmetric partner of the 172.0 GeV/c^2 top quark,

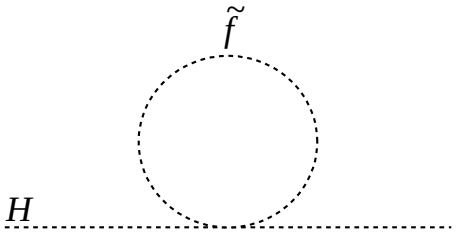

Figure 1.2: Supersymmetric scalar partner loop correction to the Standard Model Higgs boson self energy.

must be more massive than their partners to explain why they have not been detected to date. In fact, there is no direct experimental evidence in support of SUSY, so any discovery would be a grand achievement.

1.3.1 The Minimal Supersymmetric Standard Model

Generally, when searching for SUSY particles a framework is chosen that constrains the number of free parameters and the likely parameter values. The Minimal Supersymmetric Standard Model (MSSM), which we use in this search, is commonly chosen because it adds the minimal number of new parameters and can be broken softly, i.e. without introducing new quadratic divergences [17]. The names of the scalar SUSY particles are derived by adding the prefix "s" to the SM model analog. Adding the suffix "ino" to the name of a SM boson gives the SUSY analog. Symbolically, a SUSY particle is differentiated with a tilde. For example, q and $\tilde{q}$ represent a quark and a squark. t and $\tilde{t}$ represent the SM top quark and top squark. ν_e and $\tilde{\nu}_e$ represent the electron type neutrino and sneutrino. γ and $\tilde{\gamma}$ represent the photon and photino.

MSSM predicts the existence of separate Higgs boson for interacting with up type and down type quarks. Both types come in charged an uncharged varieties yielding four Higgs bosons. The Higgsinos mix with the partners of the electroweak bosons to form two charginos

and four neutralinos. These eigenstates of the charginos and neutralinos are represented by $\tilde{\chi}_1^{\pm}$, $\tilde{\chi}_2^{\pm}$ and $\tilde{\chi}_1^0$, $\tilde{\chi}_2^0$, $\tilde{\chi}_3^0$, $\tilde{\chi}_4^0$ respectively[18].

MSSM assumes the conservation of R-parity, defined by $R = (-1)^{2j+3B+L}$ where j =spin, B = baryon number, and L = lepton number [19]. All SM particles have $R = 1$, while SUSY particles have $R = -1$. Though proton decay constraints provide evidence for R-parity conservation [15], it is not assumed in all SUSY models. In order to conserve R-parity, interaction vertices must contain an even number of Supersymmetric particles. Therefore, the lightest Supersymmetric particle must be stable and is a leading dark matter candidate.

1.3.2 The Light Scalar Top Quark

In the MSSM the partner particles of the left and right chiral fermions are distinct particles labeled with $_L$ and $_R$. Since the SUSY particles are scalar, the subscript refers to the chirality of the Standard Model partners. The $_L$ and $_R$ scalars mix to form mass eigenstates. This mixing is determined by the mass matrices, which for the quark sector, are given by [14][20]:

$$M_{\tilde{q}}^2 = \begin{pmatrix} m_q^2 + m_{\tilde{q}_L}^2 + m_Z^2(\frac{1}{2} - e_q \sin^2\theta_w)\cos 2\beta & m_q(A_q - \frac{\mu}{\tan\beta}) \\ m_q(A_q - \frac{\mu}{\tan\beta}) & m_q^2 + m_{\tilde{q}_R}^2 + m_Z^2(e_q \sin^2\theta_w)\cos 2\beta \end{pmatrix} \quad (1.11)$$

where

- m_q, $m_{\tilde{q}_L}$, $m_{\tilde{q}_R}$, and m_Z are the masses of the quark, the left and right squarks, and the Z boson.

- e_q is the electromagnetic charge of the quark.

- θ_w is the electroweak mixing angle.

- $\tan\beta$ is the ratio of vacuum expectation values of the up and down type neutral Higgs bosons.

- μ is the Higgs mass parameter.

- A_q is the trilinear coupling.

The mass states $m^2_{\tilde{q}_1}$ and $m^2_{\tilde{q}_2}$ are given by the eigenvalues of the mass matrix,

$$\begin{aligned} m^2_{\tilde{q}_{1,2}} &= \frac{1}{2}(m^2_{\tilde{q}_L} + m^2_{\tilde{q}_R} + m_Z 2\cos 2\beta) + m^2_q \\ &\mp \frac{1}{2}\sqrt{[m^2_{\tilde{q}_L} - m^2_{\tilde{q}_R} + m^2_Z(\frac{1}{2} - 2e_q \sin^2\theta_w)\cos 2\beta]2 + 4m^2_q(A_q - \mu\cot\beta)^2}, \end{aligned} \tag{1.12}$$

and the rotation $\mathcal{R}$, which diagonalizes the mass matrix, relates $\tilde{q_L}$ and $\tilde{q_R}$ to $\tilde{q}_1$ and $\tilde{q}_2$ [20]:

$$\begin{pmatrix} \tilde{q_1} \\ \\ \tilde{q_2} \end{pmatrix} = \mathcal{R} \begin{pmatrix} \tilde{q_L} \\ \\ \tilde{q_R} \end{pmatrix} \tag{1.13}$$

where $\mathcal{R}$, $\cos\theta_q$, and $\sin\theta_q$ are given by

$$\mathcal{R} = \begin{pmatrix} \cos\theta_q & \sin\theta_q \\ \\ -\sin\theta_q & \cos\theta_q \end{pmatrix}, \tag{1.14}$$

$$\sin\theta_q = \frac{-m_q(A_q - \mu\cot\beta)}{\sqrt{(M^2_{\tilde{q}(1,1)} - m^2_{\tilde{q}_1})^2 + m^2_q(A_q - \mu\cot\beta)^2}}, \tag{1.15}$$

and

$$\cos\theta_q = \frac{M^2_{\tilde{q}(1,1)} - m^2_{\tilde{q}_1}}{\sqrt{(M^2_{\tilde{q}(1,1)} - m^2_{\tilde{q}_1})^2 + m^2_q(A_q - \mu\cot\beta)^2}}. \tag{1.16}$$

The mass of the Standard Model quark appears in the mixing term in the equation for the mass eigenstates, see Equation 1.12. Due to the large mass of the top quark, ∼172.0 GeV/c^2, these quark mass terms will contribute most significantly in the top quark sector, and if $(A_t - \mu \cot \beta)^2$ is large, then the light scalar top may be the lightest squark. As the lightest squark, it may also have the largest cross-section making it the easiest to detect at DØ.

As a consequence of R-parity conservation, proton/anti-proton collisions would produce top squarks in pairs via quark/anti-quark annihilation and gluon/gluon fusion, see Figures 1.3 and 1.4 respectively. Searches for the two body decay $\tilde{t}_1 \rightarrow c\ \chi_i^0$ [21] and the three

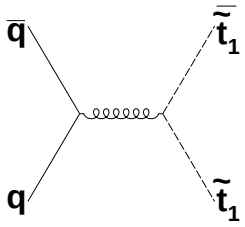

Figure 1.3: Quark/anti-quark annihilation diagram for stop quark pair production.

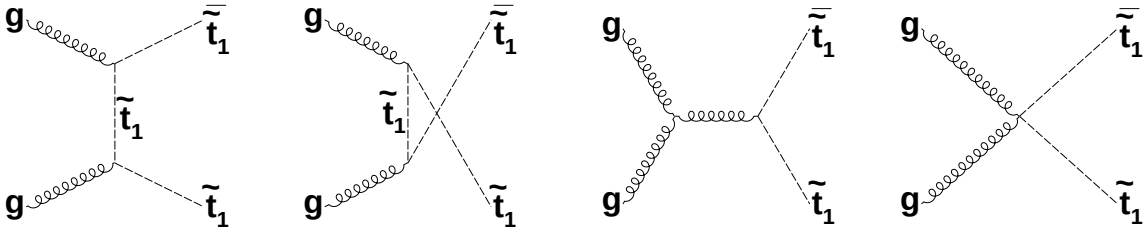

Figure 1.4: Gluon/gluon interaction diagrams for stop quark pair production.

body decay $\tilde{t}_1 \rightarrow b\ l\ \bar{\tilde{\nu}}_l$ [1], see Figure 1.5, have been published by the DØ Collaboration for 1.1 fb^{-1} of data. We describe a new search for three body decay $\tilde{t}_l\,\bar{\tilde{t}}_l \rightarrow b\bar{b}\ e\ \tilde{\nu}_e\ \mu\ \tilde{\nu}_\mu$ in 5.4 fb^{-1} of data collected at the DØ detector. In our search we assume a one hundred percent branching fraction to $bl\tilde{\nu}$ with lepton universality. Thus, we take the branching fraction for

$\tilde{t}_l \bar{\tilde{t}}_l \rightarrow b\bar{b}\ e\ \tilde{\nu}_e\ \mu\ \tilde{\nu}_\mu$ to be 2/9. We also assumed that the sneutrino either decays invisibly or is the lightest supersymmetric particle.

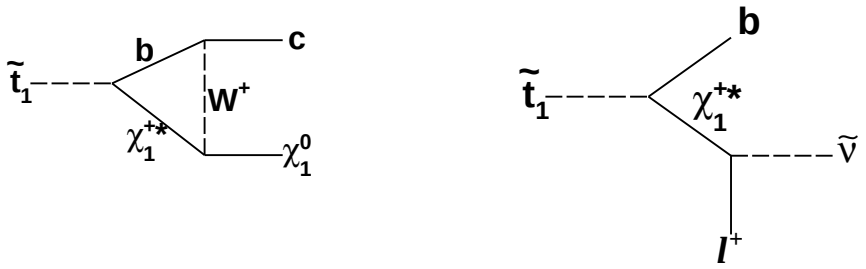

Figure 1.5: Scalar top quark two body decay into a charm quark and a neutralino (left) and three body decay into a bottom quark, a charged lepton, and a sneutrino via the exchange of a virtual chargino (right).

Chapter 2

The DØ Experiment

2.1 The Tevatron

The DØ experiment is named after its location on the main ring of the Tevatron 1.96 TeV proton/antiproton accelerator at Fermilab, shown in Figure 2.1. The Tevatron multi-stage accelerator chain begins accelerating H^- ions with a Cockcroft-Walton generator, a series of high voltage capacitors, to 750 KeV. Next the ions pass through a linear accelerator (LINAC) which increases their energy to 400 MeV. At the end of the LINAC, a series of dipole and quadrupole magnets guide the ions into the Booster synchrotron ring where they pass through carbon foil which strips off both electrons but allows the nuclei, protons, to continue accelerating around the ring until they reach 8 GeV. The next stage is the Main Injector[22] which accelerates the protons to 150 GeV and injects them into the Tevaton in 36 bunches spaced 396 ns apart.

The Main Injector also diverts some of the protons to the anti-proton source where they strike a nickel alloy target. For every 50,000 collisions, about two anti-protons are produced. The Debuncher accelerator applies stochastic and momentum cooling to reduce

the transverse and longitudinal momenta respectively[23]. From the Debuncher, the now 8 GeV anti-protons are injected into the the Accumulator. When enough anti-protons have been accumulated, they are sent to the Recycler via the Main Injector where they are stored and cooled through electron cooling. After storage, the anti-protons are returned to Main Injector where they are accelerated to 150 GeV and then injected into the Tevatron in 36 bunches spaced 396 nanoseconds apart. The accelerator chain is depicted in Figure 2.2.

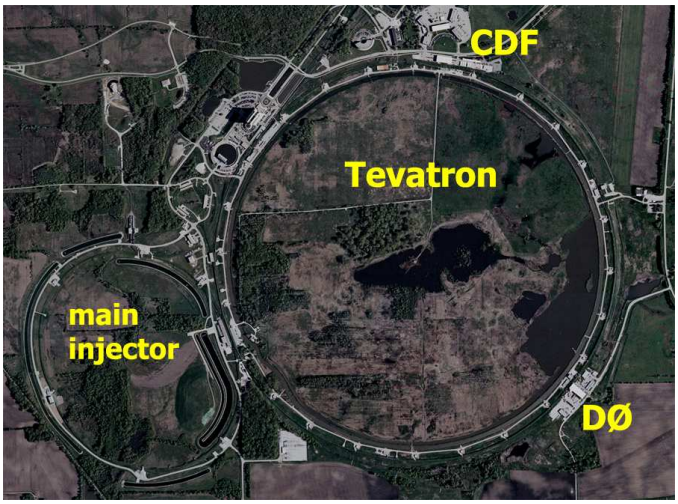

Figure 2.1: Aerial photo of the Tevatron at Fermilab in Batavia, Illinois. The DØ and CDF detectors are located on the 4 mile ring. The Main Injector accelerates protons and antiprotons to 150 GeV and injects them into the Tevatron.

2.2 The DØ Detector

The DØ detector is comprised of three subsystems. The tracking system identifies collision vertices and the paths of charged particles, the calorimeter measures energy, and the aptly named muon system identifies the tracks and measures the momentum of muons. A 3D illustration of the detector is provided in Figure 2.3. The data we use in our search comes from DØ run2. Run2 is broken into two parts: run2a which covers period from April 2002 until the shutdown in June 2006 and run2b which covers the period after the June

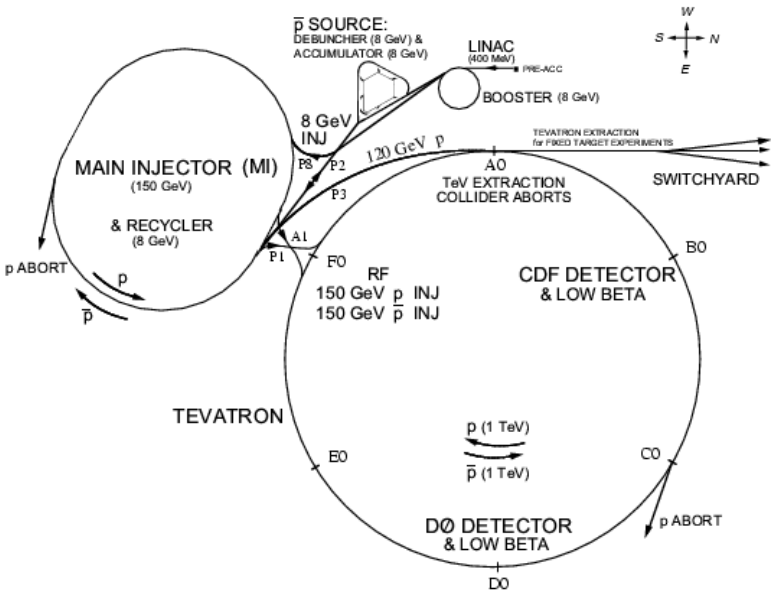

Figure 2.2: The Fermilab accelerator chain.

2006 shutdown. In this section we give an overview of the major detector subsystems. For a detailed discussion of the DØ detector, see [24].

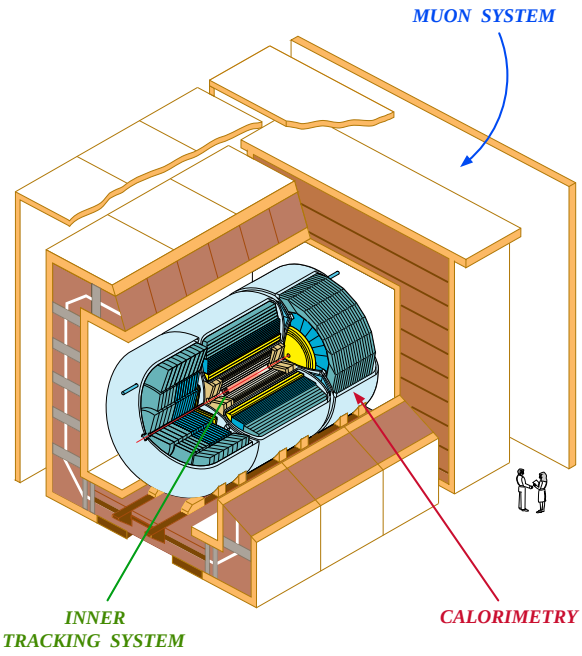

Figure 2.3: 3D cut-away drawing of the DØ detector shows the three subsystems, their relative sizes, and also the nearly hermetic coverage of the calorimeter. People are included in the drawing to show the immense scale of the detector.

At DØ we describe detected objects spatially using the coordinates $\hat{z}$, ϕ, and η. $\hat{z}$ is the

direction tangential to the proton's path around the ring. ϕ is the azimuthal angle measured in plane perpendicular to the beam direction. Rather than using the polar angle, θ, we use the pseudorapidity, η, where $\eta = -\ln[\tan\frac{\theta}{2}]$. Using pseudorapidity provides two significant benefits: the difference between two psuedorapidites is Lorentz invariant in the relativistic limit and the distribution of tracks in η is flatter than the distribution in θ which is peaked at $\theta = 0$ and π.

Particle collision events happen so rapidly at DØ that it is impossible to record them all. Instead, a three level triggering system uses inputs from all three subsystems to select the events which are most likely to contain interesting physics. The Level 1 and 2 triggers are hardware based and reduce the rate of selected events to approximately 300-1600 Hz and 200-850 Hz respectively. The software based Level 3 trigger makes the final selections which are written to tape at a rate of 25-100 Hz[1].

Writing an event to tape means writing out the measurements made by the detector. Since the variables used in our analysis are derived from the measurements, its imperative that we understand the detector and what it measures. This chapter describes the detector's major subsystems with more attention given to aspects that affect our search.

2.3 The Tracking System

The Silicon Microstrip Tracker (SMT), the Central Fiber Tracker (CFT), and the preshower detectors form the DØ tracking system. As shown in Figure 2.4, the SMT and the CFT are both inside a 2 Tesla superconducting solenoidal magnet. Just outside the magnet are the central and forward preshower detectors.

[1]Rates quoted come from the DØ run coordinator web page, http://www-d0.fnal.gov/runcoor/runplans/runplan.html

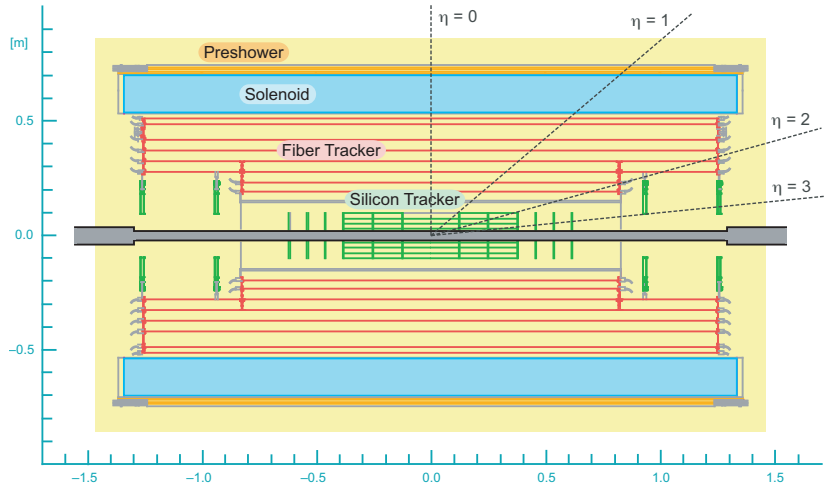

Figure 2.4: Cross section of the DØ tracking system. The forward preshower detector is not shown.

2.3.1 The Silicon Microstrip Tracker

The SMT provides both tracking and vertexing. The precise vertexing allows us to distinguish between primary and secondary decay products, enabling b-tagging, the process of identifying the high energy jets arising from the decay of bottom quark mesons. The silicon wafers are arranged to form 6 barrels and 16 disks centered along the $\hat{z}$ axis. The barrels measure (r,ϕ). For run2a the innermost barrel was located 2.7 cm away from the beam pipe. For run2b an additional layer, layer 0, was added at a distance of 1.6 cm from the beam pipe. The innermost 12 disks, called F-Disks, measure (r,$\hat{z}$) and (r,ϕ). The outermost four disks, called H-Disks, measure (r,$\hat{z}$) and (r,ϕ) for large η. All together the SMT has approximately 800,000 individual strips spaced 50 - 80 μm apart [25]. When used in conjunction with the CFT, the SMT locates the proton/anti-proton interaction position, called the primary vertex (PV), with resolution of 35 μm along the beamline. In $r-\phi$ the impact parameter resolution is better than 15 μm for particles of transverse momentum (p_T) $>$ 10 GeV/c at $|\eta| = 0$ [25]. As shown in Figure 2.4, the SMT provides coverage for $|\eta| < 3.0$. Figure 2.5 shows the design of the SMT.

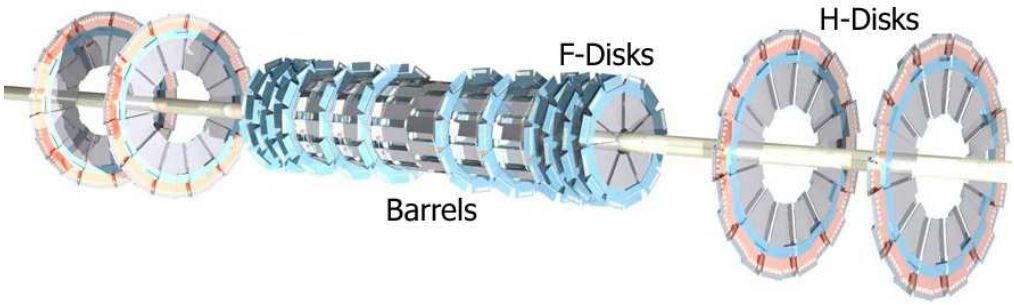

Figure 2.5: The 6 barrels, twelve F-Disks, and four H-Disks of the Silicon Microstrip Tracker.

2.3.2 The Central Fiber Tracker

The CFT has 70,000 fibers arranged in two doublet layers on each of eight concentric barrels, see Figure 2.6. The first doublet layer is axial, parallel to the beam direction. The second layer, referred to as the stereo layer, is arranged ± 3 degrees off axial. The fibers are made of polystyrene doped with the fluorescent dye paraterphenyl to make them scintillate when transversed by charged particles. The polystyrene also has 1500 ppm 3-hydroxyflavone which shifts emitted light to longer wavelengths that are more readily transmitted through the fibers. Each fiber is coated on one end with aluminum to reflect light. The other end is connected to a clear fiber wave guide which delivers the light to one of the Visible Light Photon Counters (VLPCs). The VLPCs provide greater than 75% quantum efficiency when operating at 9° Kelvin. The CFT provides coverage for $|\eta| < 2.5$ with a spatial resolution of approximately 100 μm in $r - \phi$ [25]. The momentum resolution, $\delta p_T/p_T$, is a function of η. $\delta p_T/p_T = 17\%$ for $p_T = 100$ GeV/c at $\eta = 0$ [26].

Charged particles create tracks through the CFT by causing fibers in successive layers to scintillate. Because of the solenoidal magnetic field, the tracks are curved and the direction of the curvature reveals the sign of the charge. Since the curvature is inversely proportional to the momentum transverse to the beam direction, the pattern of the fibers which scintillate reveals the momentum as well as the charge of the particle. The Level 1 and Level 2 triggers

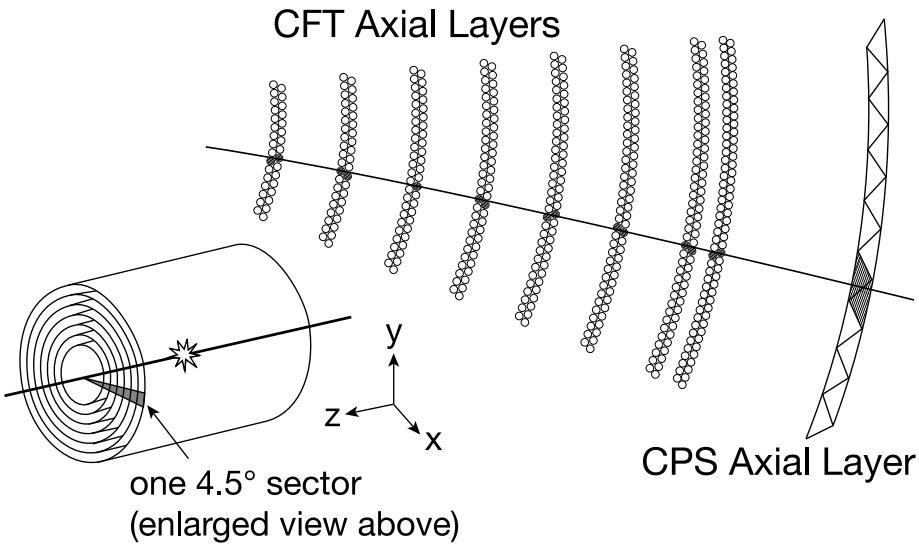

Figure 2.6: The eight concentric barrels of the Central Fiber Tracker. The CFT is divided logically into 80 sectors, each covering 4.5° in ϕ. A single sector is also indicated (lower left). A track through the eight axial doublet layers and Central Preshower axial layer is also shown (upper right). Not shown are the eight stereo doublet layers.

use the tracks from the axial fibers. The Level 3 triggers use the readout from the entire CFT.

2.3.3 The Central and Forward Preshower Detectors

The Central Preshower Detector (CPS) and the Forward Preshower Detector (FPS) provide fast electron identification for the Level 1 electron triggers. They help distinguish between photons, electrons, and heavier particles. In addition, they are used in offline reconstruction to recover some of the energy lost before an electron or photon reaches the calorimeter [25].

The CPS and FPS detectors both use scintillating triangular strips of polystyrene doped with 1% perterphynyl and 150 ppm diphenyl stilbene, see Figure 2.7. Wavelength shifting fibers, which run axially down the centers of the strips, pipe to the light to VLPCs for readout on one end and are polished and silvered on the other. The strips are made light tight by covering them in aluminized mylar and painting the ends white [25].

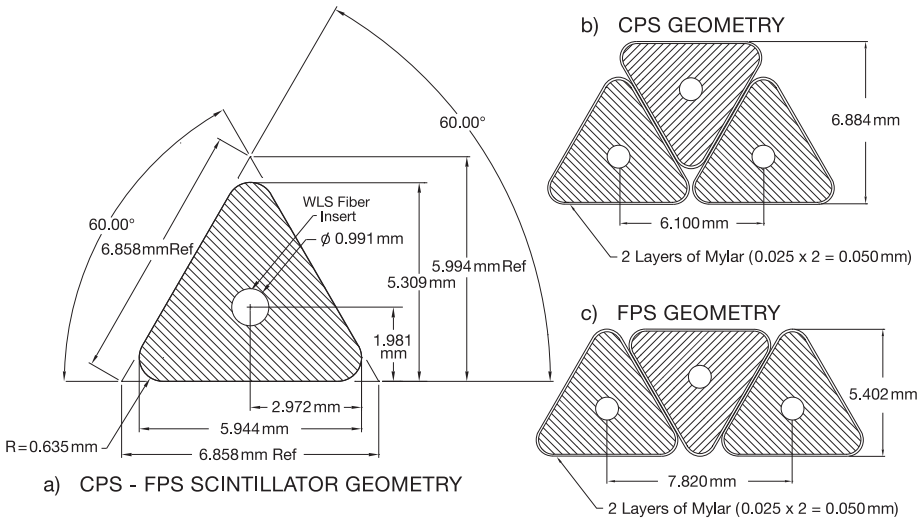

Figure 2.7: Both the central and forward preshower detectors use triangular scintillating strips. a) shows the cross-sectional dimensions of a strip. b) shows the geometry used for the strips in the CPS. C) shows the geometry used in the FPS. The circles at the center of the triangles indicate the location of the wave length shifting fibers.

The North and South FPS detectors are each divided into 16 22.5° wedges. The innermost portion of each wedge, known as the minimum ionizing particle (mip) layer, has 2 sub-layers of scintillating wedges offset by 22.5° with respect to each other. Following the mip layer is the showering material, a 2 radiation length (X_0) thick lead-stainless steel plate. This plate is followed by the showering layer, an additional 2 sub-layers of showering material. The layers are again offset by 22.5° with respect to each other. A five layers comprising a single 22.5° wedge are shown in Figure 2.8.

The three layers of the FPS work together to differentiate photons and electrons from heavier particles. As relativistic charged particles pass through the mip layer, they leave tracks but lose only a minimum amount of energy through ionization. Thus they are called minimum ionizing particles, mips, and this layer, designed to detect these tracks, is called the mip layer. As electrons pass through the showering material, they radiate energy in a process known as bremsstrahlung. The radiated photons interact with the atoms in the material to create lower energy electron/positron pairs. The newly created electrons and positrons also

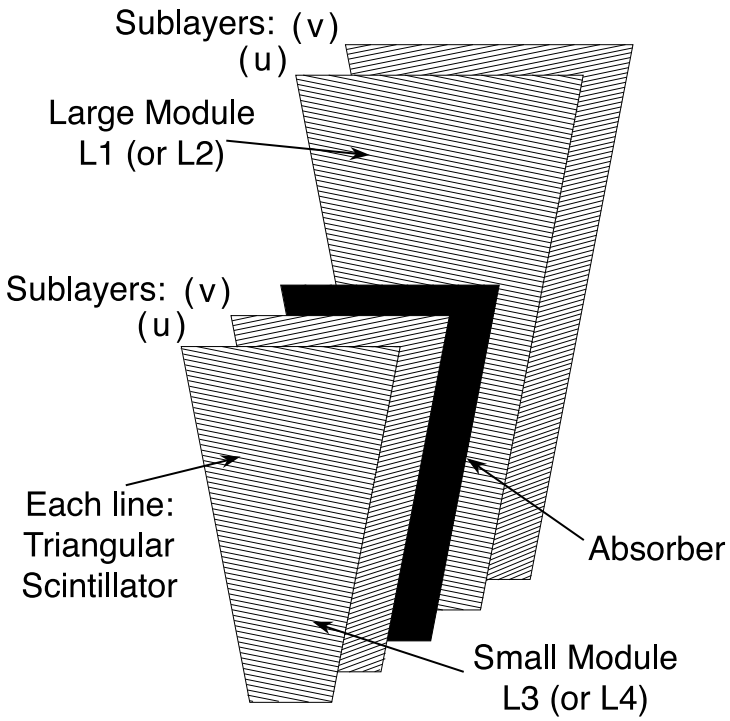

Figure 2.8: The two sublayers of FPS mip layers (front), the showering material (middle), and two sublayers of the shower layer (back) for one 22.5° section of the forward preshower detector.

radiate to create additional but lower energy photons. This radiation/pair creation cycle continues until the photons lack sufficient energy to pair create or the particles exit the material. Thus a single high energy electron is converted into a shower of lower energy particles. Since the probability of bremsstrahlung is inversely proportional to the square of the particle's mass, heavier charged particles usually pass through the material without showering. Thus, an electron produces a track in the mip layer followed by a shower in the shower layer. A heavier charged particle produces a single track which goes through both layers.

Photons generally pass through the mip layer with minimal scattering. Photons with energy > 1 MeV create showers in much the same fashion as electrons except that the showers begin with pair creation rather than bremsstrahlung [27]. This behavior gives the photon a unique FPS signature, a shower with no associated track.

The CPS uses three layers of strips, the first arranged axially and the next 2 offset by approximately $\pm 24^{\circ}$. In between the CPS and the solenoid is a layer of lead coated on both sides by stainless steel. Together the lead/steel and solenoid provide approximately 2 radiation lengths, X_0, of material to create the preshowers[25].

Particle detection in the CPS is similar to detection in the FPS. The CFT plays the role of the mip layer. The solenoid provides most of the showering material. The three layers of scintillating strips detect the shower or the continuing track.

2.4 The Calorimeter

The calorimeter measures the energy of photons, electrons, and sprays of high energy hadrons called jets. The calorimeter has three main sections, the central portion covering $|\eta| \leq 1$ and the two end-caps covering $1 \leq |\eta| \leq 4$. Each section is housed in a separate cryostat and kept at 90°K. The sections are subdivided into three types of cells which from innermost to outermost are electromagnetic (EM), fine hadronic (FH), and coarse hadronic (CH), see Figure 2.9.

All cells work using the same design principle. Alternating signal and absorber plates are held at a fixed distance apart in a cell filled with liquid argon. The signal plates are kept at a high voltage relative to the grounded absorber plates. Showers, produced when particles pass through the absorber plates, ionize the liquid argon producing free electrons. The high voltage of the signal plates attracts the electrons which produce a signal when they arrive. The electromagnetic cells use thin, depleted uranium absorber plates. The fine hadronic calorimeter cells use plates of uranium-niobium alloy. The coarse calorimeter cells use copper and stainless steel in the central and end cap calorimeters respectively.

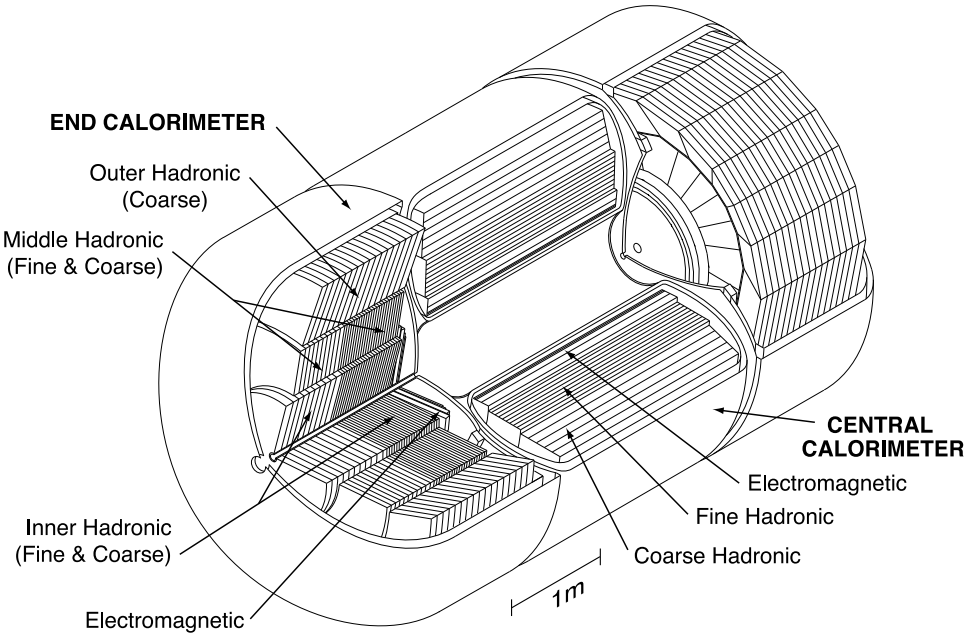

Figure 2.9: The DØ calorimeter.

The calorimeter output is used in all three trigger levels. Cells from the EM, FH, and CH calorimeters are arranged along psuedorapidity lines to form "towers" as shown in Figure 2.10. The spatial resolution of the towers is approximately 0.1 in both $\Delta\eta$ and $\Delta\phi$. Measuring

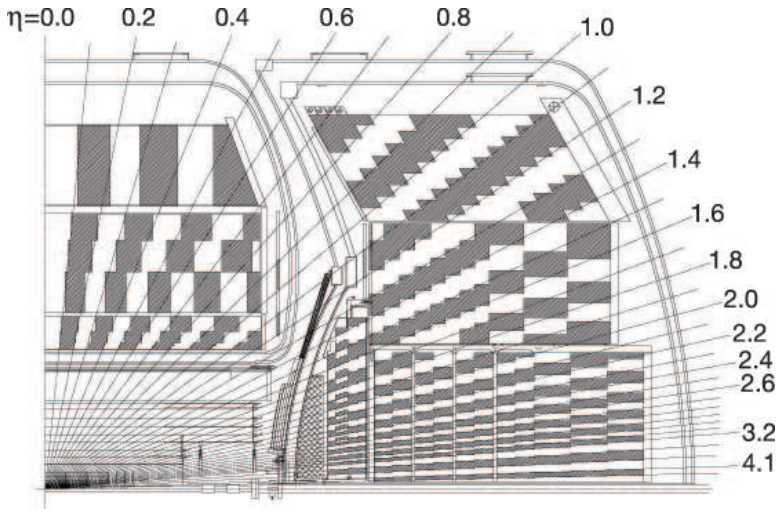

Figure 2.10: One quadrant of the DØ Calorimeter. Electromagnetic, fine hadronic, and coarse hadronic cells are arranged along pseudorapidity lines into "towers", the alternating shaded and unshaded regions in the drawing.

energy, a scalar quantity, in towers gives it a direction and allows us to define "transverse

energy" as $E_T = E \sin\theta$ where theta is the angle between the tower and the beam direction. The energy resolution $\frac{\sigma_E}{E}$ for single particles is given by

$$\frac{\sigma_E}{E} = \sqrt{C^2 + \frac{S^2}{E} + \frac{N^2}{E^2}} \tag{2.1}$$

where C is the calibration error, S is the sampling fluctuations, and N is the noise. For jets in the central calorimeter, $C = 0.072 \pm 0.021$, $S = 1.13 \pm 0.12$ GeV$^{1/2}$, and $N = 5.12 \pm 0.53$GeV [28]. For the electromagnetic calorimeter, $C = 0.005 \pm 0.0003$, $S = 0.218 \pm 0.002$ GeV$^{1/2}$, and $N = 0.488 \pm 0.019$ GeV [29].

The jet energy scale (JES) corrects the measured jet energy using the formula

$$E_{corrected} = \frac{E_{measured} - O}{R \cdot S} \tag{2.2}$$

where $E_{corrected}$ is the corrected jet energy; $E_{measured}$ is the amount of energy measured in the calorimeter; O is the "offset" which corrects for energy sources such as calorimeter noise and multiple scattering; R is the calorimeter response to the jet which includes an η dependant and an absolute component; and S is the fraction of the shower expected to leak outside of the cone $\sqrt{\Delta\phi^2 + \Delta\eta^2} > 0.5$ due to effects such as calorimeter showers or path bending due to magnetic fields [30, 31, 32].

The offset energy O is parameterized by jet η and the number of primary vertices and is typically less than 3 GeV. R is parameterized by jet energy and jet η with values between 0.9 and 1.15. Figure 2.11 shows the jet energy scale correction and the fractional uncertainty of the correction as a function of the uncorrected jet energy.

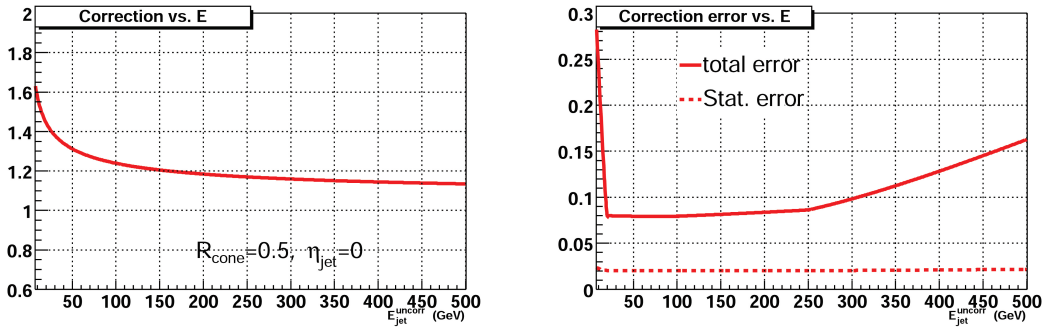

Figure 2.11: The jet energy scale correction (JES) versus E_T (left) and the uncertainty on the jet energy scale versus E_T (right). Correction is the ratio $E_{corrected}/E_{measured}$.

2.5 The Muon System

Unlike electrons which are 200 times lighter, muons are not slowed significantly by bremsstrahlung as they pass through the solenoid, the preshower detectors, or the electromagnetic calorimeter. Muons do not interact strongly, so they can pass through the calorimeter much more easily than hadrons. And, since their lifetime is 107 times longer than the tau and 10^{19} times longer than the W and Z boson, muons are likely to travel much farther before they decay. Thus, muons are the only charged particles which are likely to pass through the calorimeter into the outermost component of the detector, the muon system.

The muon system is divided into central and forward sections covering $|\eta| \lesssim 1$ and $|\eta| \lesssim 2$ respectively. Each section has three layers labeled A, B, and C with A being the closest to the interaction region. A 1.8 Tesla toroid separates layer A from layers B and C. For the A, B, and C layers, the central section uses 10 cm wide proportional drift tubes (PDTs). The cosmic cap, a layer of scintillation counters, covers the four outer sides. The Aϕ scintillation counters cover the inside of layer A. The forward sections has both 1 cm wide mini drift tubes (MDTs) and scintillation detectors for all three layers. The components of the scintillation detectors are shown in Figure 2.12.

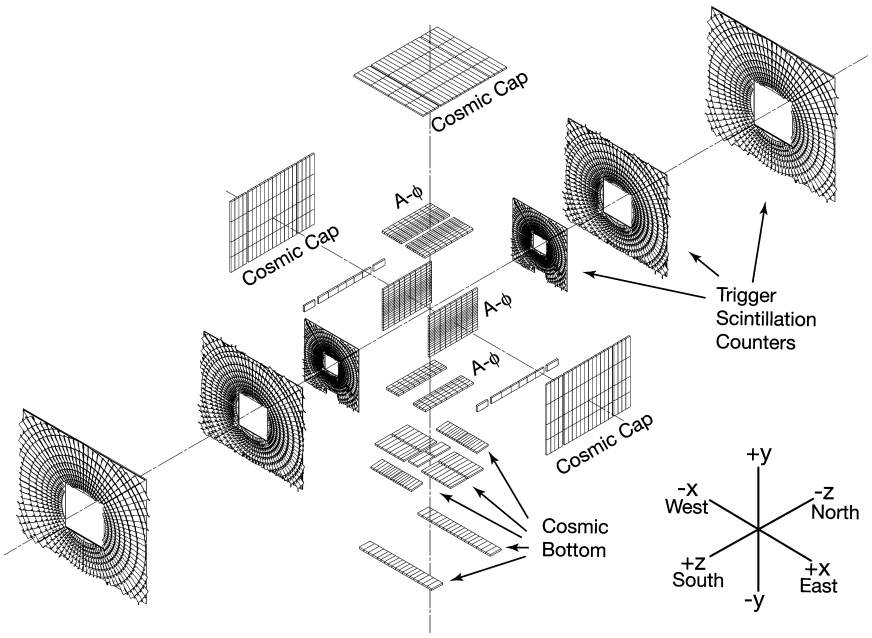

Figure 2.12: The muon system scintillation detectors.

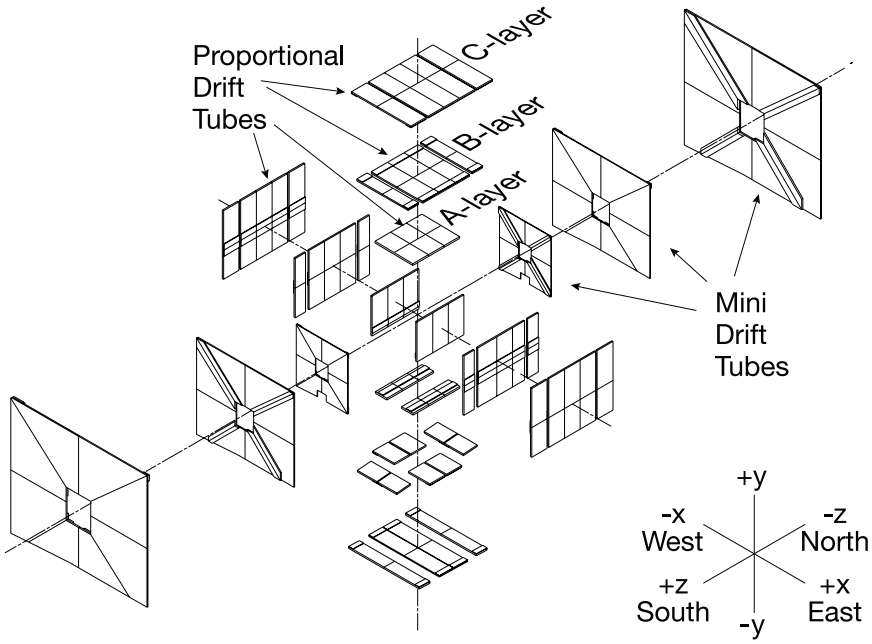

Figure 2.13: The muon system drift tubes.

The PDTs and MDTs are used to measure location and momentum. The spatial resolution of the PDTs and MDTs are 5 mm and 7 mm respectively. For particles with momentum less than 40 GeV/c, the momentum resolution, $\delta p/p$, is 0.2 for the forward section. The momentum resolution of muons with $|\eta| \lesssim 1.6$ and momentum less than 100 GeV/c is determined by the tracking system. For cases where the muon does not go through all the

layers of the CFT, $|\eta| \gtrsim 1.6$, the forward muon system is used to improve the resolution[25].

2.6 DØ Software

In this section we describe the software packages used at DØ in order to convert the readout from the detector and the events from Monte Carlo generators into the analysis ready format.

2.6.1 Detector Effects Modeling

As particles pass through the detector they continue to radiate, decay, and scatter. These processes are highly dependent on the detector geometry and the materials of which it is constructed. In order to simulate these effects in Monte Carlo events, we use the software DØ GEANT Simulation of the Total Apparatus Response (DØGSTAR) [33]. DØGSTAR provides a nearly complete model of the detector and the detector response so that Monte Carlo events will closely model data events recorded at the detector. All Monte Carlo events used in this analysis include full detector simulation.

2.6.2 Event Simulation

To simulate multiple interactions, event pile up, luminosity related affects, and detector noise, Monte Carlo events are overlayed with randomly selected detector "zero bias" events. Zero bias in this case means that the events are randomly triggered on a proton/anti-proton bunch crossing. DØSIM takes the DØGSTAR output, performs the event overlay, and then writes the events into a format compatible with the event reconstruction software.

2.6.3 Event Reconstruction

The DØ detector readouts must be converted back into physics objects such as tracks, photons, electrons, muons, and hadronic jets. This conversion is called "reconstruction" and is handled by the software package DØRECO.

Track Reconstruction

Charged particles passing through the central region of the detector leave a curved pattern of hits in the SMT and CFT. To convert the hit patterns into tracks, DØRECO uses two distinct algorithms and then combines the results. The first algorithm, Histogramming Track Finder (HTF) [34], first converts hits in (x,y) space into lines in (ρ, ϕ) space where ρ is the curvature of the track and ϕ is the initial angle of the track with respect to "beam spot", the spot where the proton and anti-proton beams are coincident. The 2D histograms are converted into tracks using a 2D Kalman filter [35]. The second algorithm, called the Alternative Algorithm (AA) [36], forms track candidates with each set of three SMT hits and then extrapolates the track candidate to the remaining layers of the SMT and the CFT looking for additional hits. As new hits are found, they are added to the set of hits and are kept if the χ^2 of a track fit to the points is less than 16 [36]. Track candidates are rejected if they contain too few hits, too many misses (track passes through sensitive detectors regions without producing hits), or too large of a χ^2 value.

Electromagnetic Clusters Reconstruction

Electrons and photons are reconstructed as clusters of energy in the electromagnetic (EM) calorimeter using a the Simple Cone Algorithm [37]. The clusters for electrons and photons the same except that electrons have a matching track in the tracking system. In the Simple

Cone Algorithm, clusters are seeded by any calorimeter towers with energy greater than 0.5 GeV. All energy from cells within the cone $\Delta R = \sqrt{\Delta\eta^2 + \Delta\phi^2} < 0.4$ is added to the initial seed. The cluster is kept as an object in the event record if the energy sum, E_{tot}, exceeds 1.5 GeV, has greater than 90% of the energy in the EM calorimeter, and is isolated. Isolation, which distinguishes a single electron or photon from one which is part of a hadronic jet, is calculated as

$$\frac{E_{tot} - E_{core}}{E_{core}} < 0.2 \tag{2.3}$$

where E_{core} is the energy in the EM towers in a the cone $\Delta R =< 0.2$ centered on the original seed tower [37].

Hadronic Jet Reconstruction

Hadronic jet reconstruction begins with creating a list of "items" which may indicate the presence a jet. In this case, "items" are energetic calorimeter towers for data events and can also be partons or particles for Monte Carlo events. Starting with the item with the largest transverse momentum, the Simple Cone Algorithm looks for additional items within the cone $\sqrt{\Delta Y^2 + \Delta\phi^2} < 0.4$ around the initial item. Here Y, the rapidity, is $Y = \frac{1}{2}\log\frac{E+p_T}{E-p_T}$. If the sum of the p_T of the items found in the cone is greater than 1 GeV, the set of items is considered a "precluster". The preclusters are used as the seeds to the RunII Cone Algorithm. This process of attempting to build precluster of items with a cone is repeated for each item in the list [38].

Starting with the hightest p_T precluster, the RunII Cone Algorithm forms a "protojet" by iterating through the list of items and adding the momentum of all items in the cone $\Delta R = \sqrt{\Delta Y^2 + \Delta\phi^2} < 0.5$. The cone is then recentered around the newly formed protojet

and a new protojet is formed by iterating through the items and summing the momentums again. This recentering and recalculating of the protojets continues until the protojet energy is < 4.0 GeV, $\Delta R < 0.001$ for a protojet and the previous iteration, or the number of protojets created from a single precluster reaches 50[38].

Before promoting protojets to jets, they are tested for overlap. If any protojets have more than half of their p_T in common with another protojet, then the protojets are merged. Otherwise the protojets are adjusted so that overlapping items are only included in the nearest protojet. The remaining protojets become the jets in the event record.

2.6.4 Muon Reconstruction

To reconstruct muons, wire chamber hit segments in the A layer PDTs and MDTs are coupled to hit segments in the BC layer PDTs and MDTs. A fit algorithm which takes into account the magnetic field, the energy loss, and the scattering caused by the iron toroid verifies that coupled segments are compatible with each other spatially and that they are compatible the interaction vertex [39]. Compatible segments form "local" muons and are matched to muon system scintillator hits. Finally, tracks formed by the coupled segments are extrapolated to the detector's central region and are matched to the central track which gives the lowest value for χ^2/(number degrees of freedom).

2.6.5 Common Analysis Format

The last layer of DØ software is called CAFe since it provides a Common Analysis Format for all analyzers [40][41]. This software is highly configurable and is used to apply the object corrections and re-weightings. It is also used for object selection and can also be used for generating plots and selection efficiencies. More details on the the object corrections,

re-weightings, and selections are given in Section 4.

2.7 DØ Data Sample

This analysis studies the data collected from April 19, 2002 through June 13, 2009 The events collected from this period were processed with DØ's Cafe software which applies the data quality requirements:

- Events from runs were removed if the experts from the SMT, CFT, calorimeter, or muon systems determined them to be bad.
- Events from luminosity blocks declared to be bad were removed.
- Events flagged as bad for the calorimeter were removed.
- Duplicate events were removed.

After data quality corrections, the luminosity for the entire sample is 5.36 fb^{-1} which includes 1.08 fb^{-1} of data from run2a and 4.28 fb^{-1} of data from run2b.

Chapter 3

Signal and Background Modeling

Ultimately in this analysis we will compare our current understanding, the SM, to the MSSM theory and test to see which model best describes the DØ data. To perform this comparison we generate the "signal" Monte Carlo events, S, to represent the MSSM theory as previously described. We also generate "background" Monte Carlo events B, to represent SM processes. For the comparison we will test statistically the degree to which the combined samples $B+S$ agree with the observed data D. We also test statistically the degree to which the sample B alone agrees with the observed data D. Before we can make this comparison, we first need to describe how we produced the samples representing S and B. In this chapter, we give that description first for the signal samples and then for each of the Standard Model processes represented by Monte Carlo.

In this search our signal is an isolated electron, an isolated muon, two bottom quark jets which may be too low in energy to be detected, and $\not\!\!E_T$ which can be small. Thus, many background processes can fake this signal for at least some of the top squark, sneutrino mass combinations.

3.1 Signal Monte Carlo Generation

We produced Monte Carlo events to represent the MSSM prediction for evenly spaced points on the stop mass, sneutrino mass plane. For each point, the MSSM particle mass and decay parameters were calculated with SuSpect version 2.3[42]. We varied the values of the parameters, $L1$, the first generation, left-chiral lepton mass, A_t, the top sector trilinear coupling constant, and μ, the Higgsino mass parameter in order to produce Susy Les Houches Accord (SLA)[43] parameter files with the desired top squark and sneutrino masses. The SuSpect output files are used as input to SDECAY 1.1a [44] which calculates the decay widths and branching ratios of the Supersymmetric particles. Madgraph/Madevent version 4.4.13 [45] was used to generate the four vectors for the signal events with Pythia version 4.09[46], to provide the parton showering and hadronization. The events were processed by the DØGSTAR, DØSIM, DØRECO, and Cafe software, see Section 2.2. The number of events produced, the cross sections, and the varied input parameters for Suspect are given for each point in Appendix C. We set the remaining SuSpect2 input parameters to the values listed in Table 3.1 for all signal points. The characteristics of this search are determined by the light top squark mass, the sneutrino mass, and the difference between these two masses. Therefore, even though the calculated sneutrino mass depends on the values of $L1$ and $\tan\beta$ and the top squark mass depends on the values of $\tan\beta$, A_T, and $M2$, the analysis is not sensitive to the exact combination of the parameters as long as the chosen combination produces the desired top squark and sneutrino masses.

3.1.1 Signal Monte Carlo Normalization

The next to leading order (NLO) cross section for light stop quark pair production was calculated by Prospino2.0 [47] with the CTEQ6.1M [48] parton distribution function. The

gaugino mass parameters (GeV/c^2)	M_1 $2 \times m(L1)$	M_2 400	M_3 500		
3^{rd} gen. mass parameters (GeV/c^2)	m_{τ_R} 250	m_{Q_L} 250	m_{t_R} 250	m_{b_R} 250	
1^{st} and 2^{nd} gen. mass parameters (GeV/c^2)	m_{e_R} 500	m_{qu} 250	m_{u_R} 250	m_{d_R} 250	
trilinear couplings (GeV/c^2)	A_τ 200	A_b 200	A_e 0	A_u 0	A_d 0
Higgs pseudoscalar mass (GeV/c^2)	M_{H_A} 800				
general MSSM parameters	$\tan\beta$ 20	sign(μ) 1			
SM terms	$1/\alpha$ 127.9	α_s 0.117	m_t 172.5	m_b 4.25	m_τ 1.78

Table 3.1: Suspect software input parameters used to generate MSSM particle masses and decay tables.

calculations were performed with the factorization and renormalization scales set to one, one half, and two times the stop mass in order to determine the nominal value and the negative and positive uncertainties due to the scale factor uncertainty. The uncertainty on the cross section due to the PDF uncertainty was computed using the formula

$$\Delta\sigma_{\text{PDF}} = \frac{1}{2}\left(\sum_{i=1}^{N_p}\left[\sigma(S_i^+) - \sigma(S_i^-)\right]^2\right)^{1/2} \tag{3.1}$$

where $N_p = 20$ (the number of theoretical parameters used in the PDF calculations), and $\sigma(S_i^\pm)$ are the values of the top squark cross section calculated using the PDF sets $S_i^\pm$ derived from the eigenvector basis of the Hessian matrix for the theoretical free parameters of the PDF. This method is explained in detail in [48]. The scale factor and PDF uncertainties are combined quadratically to produce the theoretical signal cross section uncertainty. The NLO cross sections and the uncertainties for the stop masses studied in this note are listed in Table 3.2.

Quark/anti-quark annihilation events (qq events) produce top squarks with larger amounts

stop mass (GeV/c^2)	NLO σ (pb)	fractional uncertainty +	−
100	15.10	0.19	0.19
110	8.87	0.18	0.19
120	5.45	0.18	0.19
130	3.46	0.18	0.19
140	2.25	0.17	0.20
150	1.51	0.18	0.19
160	1.03	0.19	0.19
170	0.71	0.18	0.20
180	0.50	0.18	0.20
190	0.35	0.17	0.20
200	0.25	0.17	0.20
200	0.25	0.17	0.20
210	0.18	0.17	0.20
220	0.13	0.17	0.19
230	0.10	0.17	0.20
240	0.07	0.17	0.19
250	0.05	0.17	0.20

Table 3.2: Prospino2.0 next to leading order cross sections for light stop quark pair production at the Tevatron. The nominal value and the positive and negative uncertainties were determined by setting the renormalization and factorization scales to 1, $\frac{1}{2}$, and 2 times the light stop mass. These values were combined quadratically with the PDF uncertainties to get the values shown here.

of transverse momentum than do gluon/gluon (gg events) fusion events. This extra transverse momentum is passed on to the decay products affecting not only the variable shapes, but also the efficiency of kinematic and topological cuts. As shown in Figure 3.1, the top squark pair production NLO cross sections for qq and gg events are different, especially for lower top squark masses. Therefore, when we scale the events to NLO, we need to scale the qq and gg events independently.

These differences between qq and gg events also effect the Madgraph/Madevent filter,

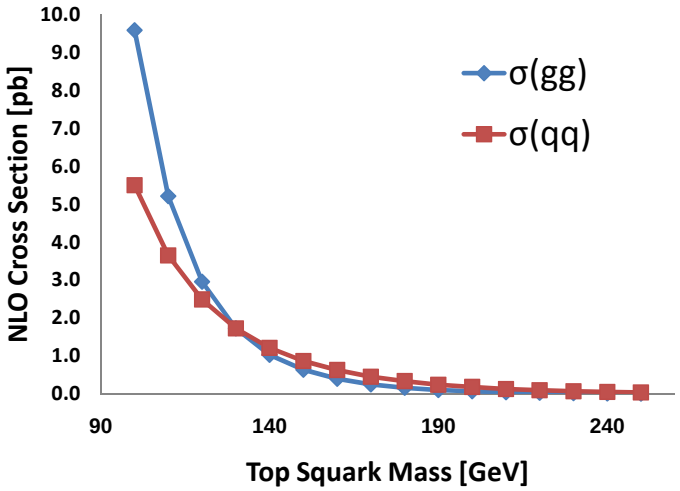

Figure 3.1: The next-to-leading order cross sections for top squark pair production as a function of top squark mass. For smaller top squark mass values, gluon/gluon fusion (gg) event cross section is much greater than the quark/anti-quark (qq) annihilation cross section.

which requires events to meet certain topological and/or kinematic requirements. For our signal, we set the filter to require that the charged leptons have transverse momentum of at least 7 GeV/c^2. The two filter efficiency factors, which are applied to events as part of the overall event scale factor, are given by the ratio of the Madgraph leading order cross sections with the filter on and off. The scale factors for gg and qq events are

$$S_{gg} = \frac{br \times \sigma_{gg} \times \epsilon_{gg}}{N_{gg}} \quad \text{and} \quad S_{qq} = \frac{br \times \sigma_{qq} \times \epsilon_{qq}}{N_{qq}} \tag{3.2}$$

where br is the branching fraction, σ_{gg} and σ_{qq} are the cross sections, ϵ_{gg} and ϵ_{qq} are the efficiencies, and N_{gg} and N_{qq} are the number of Monte Carlo events. Table C.4 in Appendix C lists S_{gg} and S_{qq} for both run2a and run2b.

3.2 Background Monte Carlo Samples

All of the generated background Monte Carlo events were processed by the DØGSTAR, DØSIM, DØRECO, and Cafe software, see Section 2.2. In this section we provide additional information about the Monte Carlo samples representing SM processes.

3.2.1 Diboson Monte Carlo

In events with two bosons, "diboson" events, the bosons can decay to produce electrons and muons and produce a similar signature similar to the signal with jets too soft for detection. The run2a WW, WZ, and ZZ samples were generated using a mixture of Pythia v6.323 and Pythia v6.409. The run2b samples are generated using Pythia v6.409. Table 3.3 lists the samples, the cross sections, and the number of events used to model the WW, WZ, and ZZ events.

background	σ (pb)	run2a events	run2b events
WW	12.0±0.67	2,457,974	709,879
WZ	3.68±0.25	600,263	632,296
ZZ	1.42±0.078	590,647	540,273

Table 3.3: The cross sections and the number of events for the diboson samples representing both run2a and run2b.

3.2.2 Z/γ^*+ jets Monte Carlo Samples

Z bosons and photons, Z/γ^*, can decay to two leptons of the same generation. $Z/\gamma^* \to \tau\bar{\tau}$ has a large cross section and a 6% branching fraction to the electron + muon final state making it the largest background in the electron + muon final state. $Z/\gamma^* \to \mu\bar{\mu}$ can fake the electron + muon final state if one muon is detected and the other radiates a photon and escapes detection. In this case the electromagnetic cluster from the photon can match to

track from the muon to fake an electron. $Z/\gamma^* \rightarrow e\bar{e}$ produces a real electron and can fake a muon by either having the second electron reach the muon system or a produce a real muon through a process associated with a hadronic jet.

We use Alpgen [49], a parton level event generator, to calculate the initial particle four vectors for Z/γ^*+ jets events. We use Pythia to perform the parton showering and hadronization. We also produce samples with either charm or bottom quark pairs in order to better match the jet spectrum observed at DØ. In order to mix these "heavy flavor" samples with the general samples, events from the original sample with charm or bottom quark pairs must be removed in a process referred to as "heavy flavor skimming"[50]. The initial cross section for the samples is calculated by Alpgen. We apply an additional factor of 1.3, called a K factor, to each of the samples in order to scale them to the next-to-next-to-leading order cross section (NNLO) given in [51]. In order to scale the heavy flavor samples to NNLO, additional scale factors of 1.52 and 1.67 are applied to the two bottom quark and two charm quark samples respectively. All three of these scale factors are used standardly at DØ and were originally presented in [52]. Table 3.4 lists the sample names, the cross sections, and the number of events for the $Z/\gamma^* \rightarrow ee$, $Z/\gamma^* \rightarrow \mu\mu$, and $Z/\gamma^* \rightarrow \tau\tau$ Monte Carlo samples for run2a and run2b. In order to generate adequate statistics to describe the tails of the distributions, the Z/γ^* samples are generated in four invariant mass bins.

Background	σ_{NNLO} (pb)	run2a events	run2b events
$Z/\gamma^* \to e\bar{e}$:			
15 GeV < M(e,$\bar{e}$) < 75 GeV	507	1,199,861	3,958,142
75 GeV < M(e,$\bar{e}$) < 130 GeV	242	6,400,741	2,143,483
130 GeV < M(e,$\bar{e}$) < 250 GeV	1.81	640,449	992,352
250 GeV < M(e,$\bar{e}$) < 1960 GeV	0.15	378,240	2,026,439
$Z/\gamma^* + 2b \to e\bar{e} + 2b$:			
15 GeV < M(e,$\bar{e}$) < 75 GeV	1.62	379,193	341,371
75 GeV < M(e,$\bar{e}$) < 130 GeV	1.35	337,281	332,279
130 GeV < M(e,$\bar{e}$) < 250 GeV	0.01	158,906	174,142
250 GeV < M(e,$\bar{e}$) < 1960 GeV	0.001	553,290	523,883
$Z/\gamma^* + 2c \to e\bar{e} + 2c$:			
15 GeV < M(e,$\bar{e}$) < 75 GeV	11.9	383,438	535,300
75 GeV < M(e,$\bar{e}$) < 130	3.63	355,666	319,135
130 GeV < M(e,$\bar{e}$) < 250	0.03	192,175	366,887
250 GeV < M(e,$\bar{e}$) < 1960 GeV	0.003	580,279	691,791
$Z/\gamma^* \to \mu\bar{\mu}$:			
15 GeV < M(μ,$\bar{\mu}$) < 75 GeV	506	1,204,151	2,839,715
75 GeV < M(μ,$\bar{\mu}$) < 130 GeV	242	6,702,428	2,665,356
130 GeV < M(μ,$\bar{\mu}$) < 250	1.77	1,358,420	823,713
250 GeV < M(μ,$\bar{\mu}$) < 1960 GeV	0.16	394,111	1,617,847
$Z/\gamma^* + 2b \to \mu\bar{\mu} + 2b$:			
15 GeV < M(μ,$\bar{\mu}$) < 75 GeV	1.54	444,310	348,689
75 GeV < M(μ,$\bar{\mu}$) < 130 GeV	1.38	329,494	346,753
130 GeV < M(μ,$\bar{\mu}$) < 250 GeV	0.01	192,024	174,142
250 GeV < M(μ,$\bar{\mu}$) < 1960 GeV	0.001	551,526	514,512
$Z/\gamma^* + 2c \to \mu\bar{\mu} + 2c$:			
15 GeV < M(μ,$\bar{\mu}$) < 75 GeV	12.2	394,590	369,109
75 GeV < M(μ,$\bar{\mu}$) < 130 GeV	3.76	346,255	337,949
130 GeV < M(μ,$\bar{\mu}$) < 250 GeV	0.03	192,771	173,296
250 GeV < M(μ,$\bar{\mu}$) < 1960 GeV	0.003	580,528	542,997
$Z/\gamma^* \to \tau\bar{\tau}$:			
15 GeV < M(τ,$\bar{\tau}$) < 75 GeV	506	1,203,009	2,618,579
75 GeV < M(τ,$\bar{\tau}$) < 130 GeV	243	2,564,263	6,854,001
130 GeV < M(τ,$\bar{\tau}$) < 250 GeV	0.15	368,473	849,931
250 GeV < M(τ,$\bar{\tau}$) < 1960 GeV	1.77	635,780	1,473,067
$Z/\gamma^* + 2b \to \tau\bar{\tau} + 2b$:			
15 GeV < M(τ,$\bar{\tau}$) < 75 GeV	1.59	378,140	352,721
75 GeV < M(τ,$\bar{\tau}$) < 130 GeV	1.38	339,326	334,768
130 GeV < M(τ,$\bar{\tau}$) < 250 GeV	0.0120	191,918	173,498
250 GeV < M(τ,$\bar{\tau}$) < 1960 GeV	0.001	707,584	513,462
$Z/\gamma^* + 2c \to \tau\bar{\tau} + 2c$:			
15 GeV < M(τ,$\bar{\tau}$) < 75 GeV	11.9	396,138	540,598
75 GeV < M(τ,$\bar{\tau}$) < 130 GeV	3.67	341,176	411,756
130 GeV < M(τ,$\bar{\tau}$) < 250 GeV	0.032	192,304	187,400
250 GeV < M(τ,$\bar{\tau}$) < 1960 GeV	0.003	588,407	549,209

Table 3.4: The cross sections and the number of events for the run2a and run2b γ^*/Z background samples.

3.2.3 $W + jets$ Monte Carlo Samples

As shown in Table 3.5, the production cross section for the W boson plus hadronic jets background is very large, more than 800 times larger than that of our signal. The W boson has a 21% branching fraction to a muon or an electron. The second lepton can come from hadronic decays, hadronic fakes, or photons matched to stray tracks.

As with the $\gamma^*/Z+$ jets samples, we use Alpgen + Pythia to generate light and heavy flavor $W + jets$ samples. Again, we apply heavy flavor skimming and use a K factor of 1.3 in order to scale the sample to the NNLO. The additional heavy flavor K factors for the $W + jets$ two bottom quark and two charm quark samples are both 1.47. These scale factors were originally presented in [52]. Table 3.5 lists the cross sections and the number of events for the $W + jets$ Monte Carlo samples.

background	σ_{NNLO} (pb)	run2a events	run2b events
W+jets→charged lepton + neutrino + jets	8060	33,046,933	62,977,228
W+2b+jets→charged lepton + neutrino + jets	31.22	2,662,633	2,823,364
W+2c+jets→charged lepton + neutrino + jets	98.13	2,734,849	2,697,098

Table 3.5: The cross sections and the number of events for the run2a and run2b $W + jets$ background samples.

3.2.4 Top Pair Production Monte Carlo Samples

Not surprisingly, the top quark pairs can fake the top squark pairs signal. Top quark pairs decay to produce two bottom quark jets and two W bosons. The largest portion of this background comes from events where one W boson decays to produce an electron and the other decays to produce a muon. The remainder comes from W bosons decaying to tau leptons which then decay to produce electrons or muons and from hadronic decays of the W faking a lepton.

We use Alpgen + Pythia to generate top quark pairs. We scale the top quark pairs sample using the NLO cross section given in [53], $7.48^{+0.56}_{0.73}$. Tables 3.6 lists the the cross sections and the number of events for the $t\bar{t}$ Monte Carlo samples.

background	σ_{NNLO} (pb)	run2a events	run2b events
$t\bar{t} \rightarrow$ 2b + charged lepton + neutrino + jets	3.30	1,529,900	1,458,935
$t\bar{t} \rightarrow$ 2b + 2 charged leptons + 2 neutrinos + jets	0.83	1,546,454	1,556,016
$t\bar{t} \rightarrow$ 2b + jets	3.35		

Table 3.6: The cross sections and the number of events for the run2a and run2b top pair background samples. The cross section for the process $t\bar{t} \rightarrow$ 2b + jets is included to show its contribution toward the total top pair production cross section of 7.48 pb.

Chapter 4

Preselection

This chapter describes the initial constraints and corrections which are applied to data and Monte Carlo events to produce samples which we understand in terms of normalization and distribution for our primary analysis variables. We call these constraints and corrections the "preselection". All of the data and Monte Carlo samples were processed the Common Analysis Framework (CAFe) software packages which applies the corrections and also applies the object definitions as described below.

4.1 Electron Selection

Electrons were required to have transverse momentum greater than 15 GeV/c and to have $|\eta| < 1.1$. The momentum is determined from the energy deposition in the calorimeter because it has a finer resolution than the tracking system. They were also required to meet the following criteria:

- The energy in the calorimeter cone $0.1 < \Delta\mathcal{R} < 0.5$ around the electron track divided by the electron energy must be less than 0.15 to discriminate against EM objects which

are part of hadronic jets.

- 90% of the energy must be deposited in the electromagnetic portion of the calorimeter to discriminate between electrons and hadronic jets.

- The shower shape H-matrix must be consistent with that of an electromagnetic shower. The H-matrix for the central region is the inverse of the covariance matrix relating the energy fractions in each of the four EM readout layers, the total EM energy, vertex z-position, and the transverse shower width in ϕ [54][55].

- Electrons must be matched to a central track within a window $\Delta\eta \times \Delta\phi = 0.05 \times 0.05$ around the electromagnetic cluster to distinguish them from photons matched to tracks from a charged particle [56][55].

- The central track is required to have transverse momentum > 5 GeV/c.

- $E_T/p_T < 2.5$ where E_T is the calorimeter transverse energy and p_T is the momentum of the associated track. This requirement distinguishes electrons from photons and neutral hadrons associated with a track from a low momentum charged particle.

- The eight-variable likelihood function, which discriminates between electromagnetic and hadronic showers, must be greater than 0.85. The eight variables included in the likelihood are the number of tracks, the sum of the track p_T, the spatial track match probability, $\frac{E_T}{p_T}$, distance of closest approach between the electron track and the primary vertex in $\hat{z}$, electromagnetic fraction of the calorimeter cluster associated with the electron, H-Matrix, and number of CPS strips / E_{EM} where E_{EM} is the energy of the electromagnetic cluster [54][57][55].

To create the likelihood function, the probabilities for an EM cluster to be an electron, P_e, or something else, P_n where n is for noise, are defined as

$$P_e(\mathbf{x}) = \prod_i^8 p_e(x_i) \qquad \text{and} \qquad P_n(\mathbf{x}) = \prod_i^8 p_n(x_i) \tag{4.1}$$

where $\mathbf{x}$ is vector of electron variables and $p_e(x_i)$ and $p_n(x_i)$ are the probabilities densities for each of the eight likelihood variables. The likelihood is

$$L(\mathbf{x}) = \frac{P_e(\mathbf{x})}{P_e(\mathbf{x}) + P_n(\mathbf{x})}. \tag{4.2}$$

$L(\mathbf{x})$ is close to 1 for electron-like clusters [57].

Events are required to have exactly one electron meeting these requirements, and the electron is required to have the opposite charge of the muon.

4.2 Jet Definition

Jets considered in this analysis are "good" jets in that they meet the standard good (cone $\Delta\mathcal{R} = \sqrt{(\Delta\phi)^2 + (\Delta\eta)^2} < 0.5$) jet requirements determined by the Jet ID group[58]:

- The transverse energy must be > 20.0 GeV.
- The Electromagnetic fraction of the energy must be greater than 5% but less than 95%.
- The coarse hadronic fraction must be less than 50%.
- $|\eta| < 2.5$.

- To reduce the effects of noisy cells faking a jet, no single calorimeter cell is allowed to have 90% or more of the total jet energy.
- We require $E_{L1}/\left(p_T \times \left(1 - \frac{E_{CH,T}}{E_T}\right)\right) > 0.4$ where E_{L1} is the energy read out by the first level of the triggering system, $E_{CH,T}$ is the transverse energy measured in the coarse hadronic portion of the calorimeter, and p_T and E_T are the transverse momentum and energies of the jets [59].

The jet energy scale correction was applied to all events. For Monte Carlo events the jet energy was smeared to better match the data and a jet identification efficiency correction was applied. Any jets for which $\Delta\mathcal{R}(jet, electron) < 0.5$ were removed. For run2b data and Monte Carlo, we require jets to have at least two tracks pointing to the primary vertex; this requirement reduces the correlation between the luminosity and the number of jets. This requirement is only needed for run2b because run2b data has a much higher average instantaneous luminosity. We did not require events to have a jet.

4.3 Muon Selection

Muons were reconstructed in the region $|\eta| < 2$. The muon identification is broken down into three parts: muon system quality, tracking system quality, and calorimeter isolation. Selected muons were required to have at least two A and BC layer wire hits, an A layer scintillator hit, and a BC layer scintillator hit unless the muon is in the central portion of the muon system and it has less than four hits in the BC layer scintillator. These criteria are relaxed to a scintillator hit and two wire hits if the muon is in the hole between $[\frac{4\pi}{3}, \frac{5\pi}{3}]$ (the hole corresponds to the break in the muons system to allow for the detector support structure). The muon tracks were required to meet the following criteria [60][61]:

- The χ^2/(degrees of freedom) of the matched central track and the extrapolated muon system track must be less than 4.0.

- If there were silicon microstrip tracker (SMT) hits, then the distance of closest approach (DCA) between the muon track and the primary vertex must be less than 0.02 cm.

- If there were no SMT hits, then DCA must be less than 0.2 cm.

Muons were required to meet the following isolation requirements:

- The transverse energy in the calorimeter cone $\Delta\mathcal{R} < 0.5$ around the muon track divided by the muon p_T must be less than 0.15.

- The sum of the transverse energy of the all the tracks in the hollow cone $0.1 < \Delta\mathcal{R} < 0.5$ divided by the p_T of the muon track must be less than 0.15.

In addition, muons were required to have $p_T > 10.0$ GeV/c. Events were required to have exactly one muon meeting these requirements. Further, events were rejected if $\Delta\mathcal{R}(e, \mu) < 0.5$.

4.4 $\not\!\!E_T$ and Primary Vertex Selection

The missing transverse energy, $\not\!\!E_T$, is calculated from the energy of the coarse hardronic calorimeter cells within the cone of "good" jets and all electromagnetic and fine hadronic calorimeter cells. This value is then corrected for all selected muons. We require run2a events to have $\not\!\!E_T > 20$ GeV because the Monte Carlo does not effectively model the data for events with low $\not\!\!E_T$. Run2b events are required to have $\not\!\!E_T > 7.0\ GeV$.

The absolute value of the z component of the primary vertex was required to be less than 60 centimeters.

4.5 Event re-weightings

The following re-weightings were applied to the Monte Carlo in order to improve its modeling of DØ data:

Luminosity re-weighting - Scales events to make the luminosity profile of the zero bias overlay events match the luminosity profile of the data [62].

Beam spot re-weighting - The acceptance of events at DØ is dependent upon the shape and location of the region in which the proton and anti-proton bunches interact. Beam spot re-weighting adds a correction factor to Monte Carlo events so that they will better model the effects the beam spot has on data events. The correction is parameterized by data epoch, instantaneous luminosity, and the cut on the z vertex [63].

W/Z $\mathbf{p}_T$ - Scales events to make the distributions of the transverse momentum of the W and Z bosons in Monte Carlo agree with the distribution of data events [64],[65].

EM ID efficiency - Scales events to make the electromagnetic object identification [66] efficiency for Monte Carlo match the efficiency for data.

Muon ID efficiency - Scales events to make the muon identification efficiency [61] for Monte Carlo match the efficiency for data.

Muon Isolation efficiency - Scales events to correct for the discrepancies between the Monte Carlo and data in efficiency for the muon isolation requirements [61].

Muon Track efficiency - Scales events to correct for the discrepancies between the Monte Carlo and data in efficiency for muon track requirements [61].

Lepton p_T oversmearing - In order to make the lepton p_T distributions consistent between Monte Carlo and data, the Monte Carlo charged leptons were "oversmeared" by adding a random Gaussian to the p_T [67][68][69].

4.6 Trigger Efficiency Correction

For this analysis we required events in the data sample to have fired at least one single EM or single muon trigger, see Appendix F for a list of the included triggers. We estimated the Monte Carlo trigger efficiency correction directly from the search data which has the benefit of naturally scaling the efficiency contributions of the various trigger sets to their luminosity contributions and including any effects of the preselection requirements (for example, requiring only one of each lepton, opposite sign charge, and $\Delta R(electron, muon) > 0.5$). We first estimated the efficiency of requiring at least one single EM trigger. We next estimated the efficiency of requiring at least one single muon trigger. Lastly, we combined these two estimates to form the correction we applied to the Monte Carlo.

4.6.1 Efficiency of the Single EM Triggers OR

To determine the parametrization for the correction to estimate the efficiency of the single EM triggers OR, we started by first selecting all events from the analysis data post preselection that fired a single muon trigger. From this sample, we plotted the single EM trigger efficiency as a function of the electron variables transverse momentum $p_T(e)$, calorimeter η, ϕ, and instantaneous luminosity, see Figure 4.1. These plots show that there is a clear dependence on electron transverse momentum. It also appears that there is no dependence on ϕ or instantaneous luminosity. There may be a slight dependence on η.

In order to estimate the trigger efficiency, we used a Generalized Linear Model (GLM) [70]. GLM's, which are commonly used in statistics, finance, medicine, biology, and the social sciences, extend the ubiquitous linear regression model, in which the response variable [1] has

[1] In order to better convey the relationship between variables used in models, modern statistics literature uses the terms explanatory and response rather than independent and dependent. The terms independent and dependent imply causality which is often not the case.

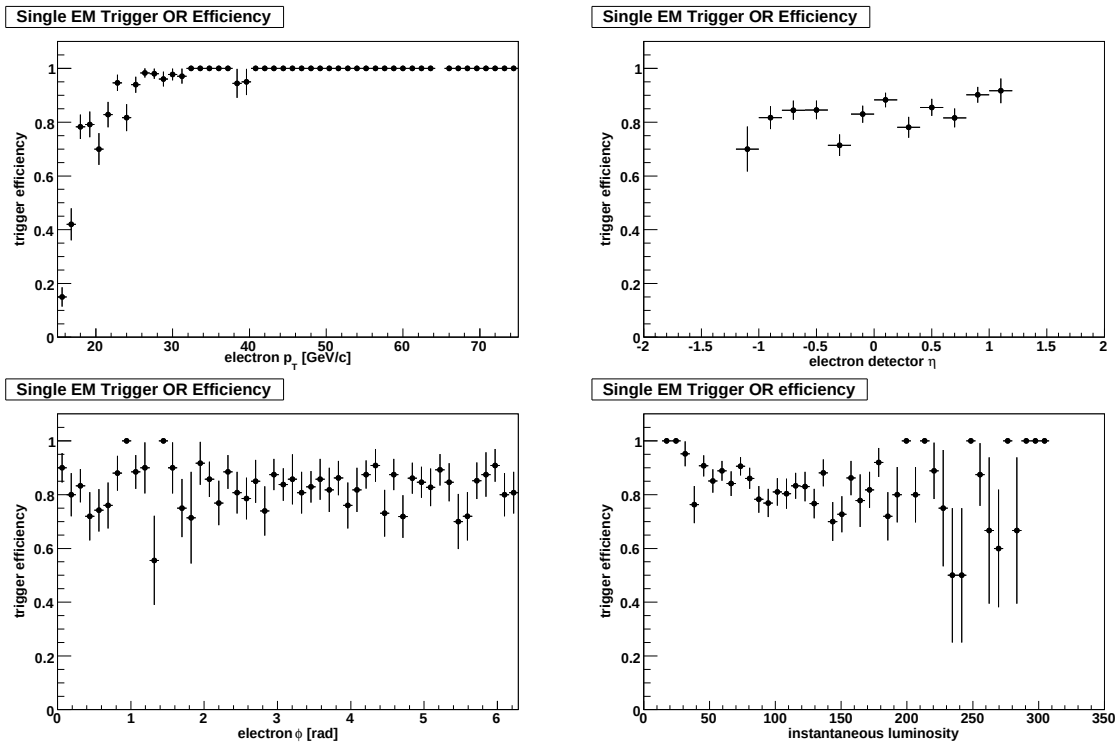

Figure 4.1: Plots show how the single EM triggers OR efficiency depends on the electrons variables transverse momentum (upper left), calorimeter η, ϕ, and instantaneous luminosity. Plots shown use run2b data.

a Gaussian uncertainty, to the exponential family of functions[2], which includes the cases where the response variable has Poisson and binomial uncertainties. The trigger efficiency, $\hat{\epsilon}_e$, is a binomial response variable and we model it using a GLM with a logit link function of the form

$$\text{logit}(\hat{\epsilon}_e) = \log(\frac{\hat{\epsilon}_e}{1-\hat{\epsilon}_e}) = \beta_0 + \sum_i^k \beta_i x_i \tag{4.4}$$

where ϵ_e is the trigger efficiency, the x_i's are explanatory variables from the data, k is the

[2]The exponential family includes functions with the general form

$$f(y|\theta,\phi) = \exp\left[\frac{y\theta - b(\theta)}{a(\phi)} + c(y,\phi)\right] \tag{4.3}$$

where θ and ϕ represent the location and dispersion of the distribution [71]. For a more complete discussion, see McCullagh Section 2.2.2 [70] or Faraway Chapter 6 [71].

number of explanatory variables, and the β_i's are linear coefficient determined by regression [72]. The uncertainty on logit($\hat{\epsilon}_e$) is

$$\hat{\sigma}_{\epsilon_e} = \sqrt{\mathbf{X}^T \mathbf{V} \mathbf{X}} \tag{4.5}$$

where $\mathbf{X}$ is a vector of explanatory variable values and $\mathbf{V}$ is the covariance matrix for the coefficients [73]. The utility of the logit form for the binomial case is apparent after solving eq. 4.4 for $\hat{\epsilon}_e$ and including a one $\hat{\sigma}_{\epsilon_e}$, 68%, confidence interval:

$$\hat{\epsilon}_e = \frac{e^{\boldsymbol{\beta}\mathbf{X} \pm \sqrt{\mathbf{X}^T \mathbf{V} \mathbf{X}}}}{1 + e^{\boldsymbol{\beta}\mathbf{X} \pm \sqrt{\mathbf{X}^T \mathbf{V} \mathbf{X}}}}. \tag{4.6}$$

The model specified in eq. 4.6 predicts values between 0 and 1 for both the trigger efficiency and its confidence interval. The confidence interval is appropriately asymmetric and heteroskedastic[3]. We used the R software package [74] to calculate both $\boldsymbol{\beta}$ and $\mathbf{V}$. For the Single EM Triggers OR efficiency model in particular, we determined the explanatory variable to be the natural log of the electron transverse momentum, $p_T(e)$, was expected based on Fig. 4.1. We tested the model with additional explanatory variables but none made significant improvements to the model.

The vector of the coefficients, $\boldsymbol{\beta}$, and the covariance matrix, $\mathbf{V} = \mathbf{SRS}$ for run2a and run2b respectively are

$$\boldsymbol{\beta} = \begin{pmatrix} -15.52 & 5.86 \end{pmatrix}, \tag{4.7}$$

[3]The uncertainty is a function of the explanatory variables in the model.

$$\mathbf{S} = \mathrm{diag}(4.215, 1.441); \quad \mathbf{R} = \begin{pmatrix} 1.0 & -0.998 \\ -0.998 & 1.0 \end{pmatrix} \tag{4.8}$$

and

$$\boldsymbol{\beta} = \begin{pmatrix} -22.03 & 7.71 \end{pmatrix}, \tag{4.9}$$

$$\mathbf{V} = \mathbf{SRS}; \quad \mathbf{S} = \mathrm{diag}(1.645, 0.557); \quad \mathbf{R} = \begin{pmatrix} 1.0 & -0.998 \\ -0.998 & 1.0 \end{pmatrix} \tag{4.10}$$

Here $\mathbf{S}$ is a diagonal matrix with the standard deviations for each variable along the diagonal. $\mathbf{R}$ is the correlation matrix[4]. The 95%, approximately two sigma, confidence interval is obtained by multiplying the uncertainty term by 1.96. A comparison of the trigger efficiency prediction of the GLM and the ratio of triggered to untriggered events in Figure 4.2. Figure 4.3 compares the distributions of data events passing the single EM triggers OR requirement to Monte Carlo events without and with the GLM applied as a correction.

[4]Reporting the covariance matrix a product of standard deviations and correlations provides more insight into the relationships between the variables and allows the reader to reconstruct the covariance matrix elements which would be zero to the precision reported here. Thanks to David Scott for this suggestion.

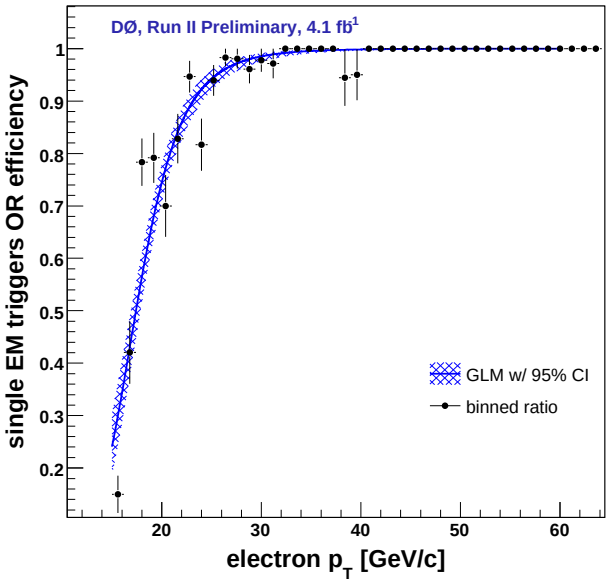

Figure 4.2: A comparison of the single EM triggers OR probability predicted by a GLM (smooth curve) compared to the ratio of triggered to untriggered points in 5 GeV/c bins. Both models are derived from the set of all events in the run2b data that fired at least one single muon trigger.

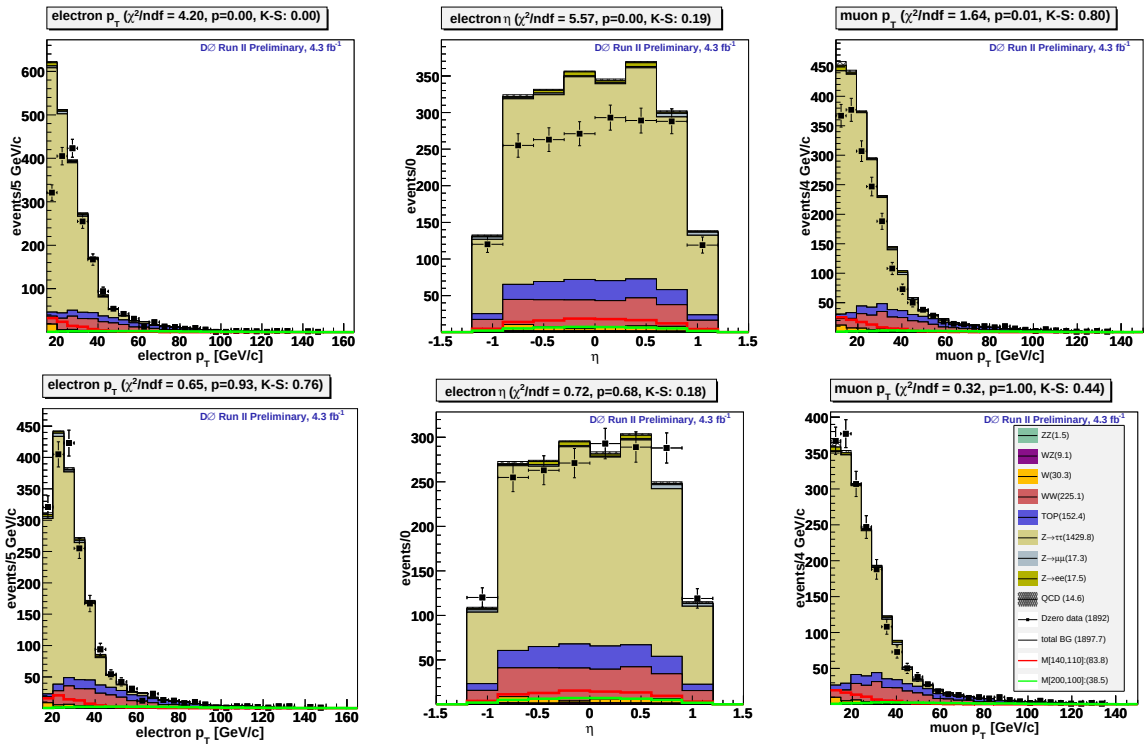

Figure 4.3: A comparison of data (points) to Monte Carlo estimates (colored histograms) without (top row) and with (bottom) the single EM triggers OR efficiency correction applied. The data events are required to have fired at least one single EM trigger. From left to right, the plots show electron transverse momentum, electron η, and muon transverse momentum. Plots shown use run2b data and Monte Carlo.

4.6.2 Efficiency of the Single Muon Triggers OR

To determine the explanatory variables for the single MU triggers OR efficiency model, we started by first selecting all events from the analysis data post preselection that fired at least one single EM trigger. From this sample, we plotted the single MU trigger efficiency, as a function of the muon variables transverse momentum, calorimeter η, ϕ, and instantaneous luminosity, see Figure 4.4. The plots show an apparent dependence on muon η and apparently

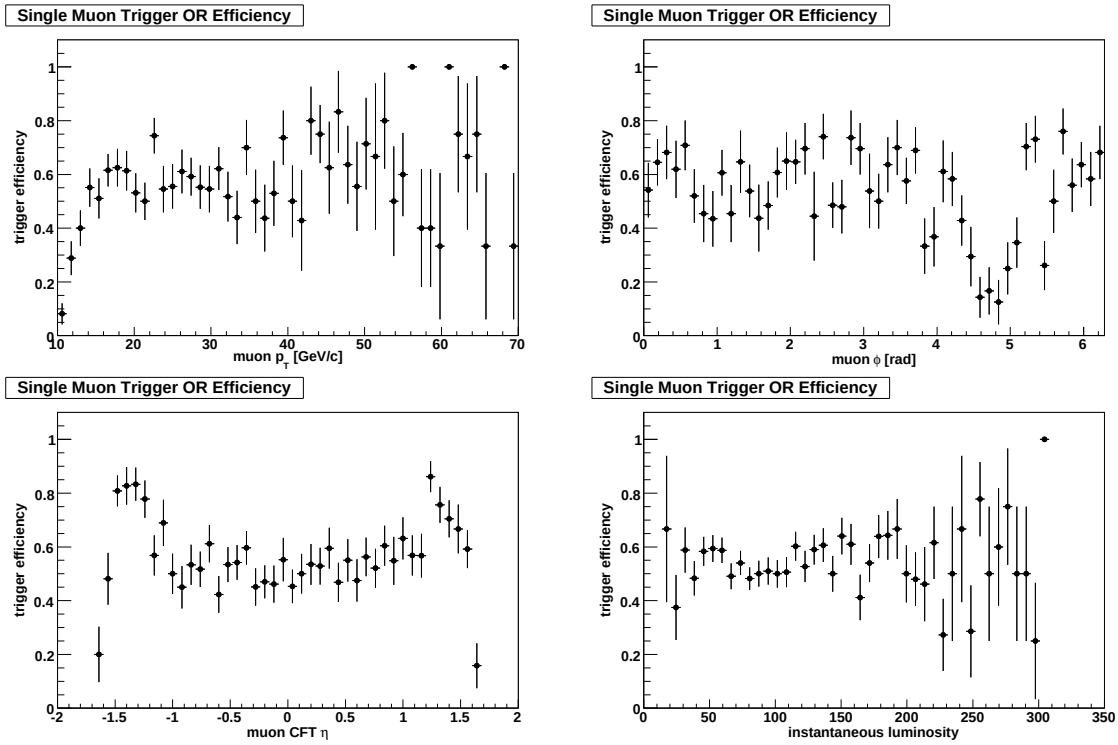

Figure 4.4: Plots show how the single MU triggers OR efficiency depends on the muon variables transverse momentum (upper left), CFT η, ϕ, and instaneous luminosity. Plots shown use run2b data.

no dependence on luminosity. The efficiency is not dependent on ϕ except in the region $\phi \in [\frac{4\pi}{3}, \frac{5\pi}{3}]$ where the muon system has a hole to make room for the detector support structure. So rather than treating this dependence as a continuous variable, we treat it categorically as a binary "in the hole" and represent it with H. Similarly, the efficiency is dependent on muon p_T but only from 10.0 to 15.0 GeV/c. Therefore, we use the categorical binary variable "is low p_T" and represent it with L. As shown in Figure 4.4, the muon trigger efficiency has a symmetric dependency on muon η. We found that this symmetric dependency is modeled well by a combination of the symmetric polynomial terms η^8, η^6, and η^4. For the linear equation for run2a, we use the variables η^8, η^6, η^4, H, and $\log p_T(\mu)$ where η refers the track η measured in the CFT and $p_T(\mu)$ is the transverse momentum of

the muon. The vector of the coefficients, $\boldsymbol{\beta}$, and the covariance matrix, $\mathbf{V} = \mathbf{SRS}$, are

$$\boldsymbol{\beta} = \begin{pmatrix} -2.05 & 0.12 & -0.78 & 1.14 & -2.80 & 0.79 \end{pmatrix} \tag{4.11}$$

$$\mathbf{S} = \text{diag}(0.143,\ 0.050,\ 0.289,\ 0.416,\ 0.167,\ 0.082) \tag{4.12}$$

$$\mathbf{R} = \begin{pmatrix} 1.00 & -0.39 & 0.44 & -0.52 & -0.15 & -0.34 \\ -0.39 & 1.00 & -0.99 & 0.94 & -0.02 & -0.03 \\ 0.44 & -0.99 & 1.00 & -0.98 & 0.02 & 0.03 \\ -0.52 & 0.94 & -0.98 & 1.00 & -0.01 & -0.03 \\ -0.15 & -0.02 & 0.02 & -0.01 & 1.00 & 0.01 \\ -0.34 & -0.03 & 0.03 & -0.03 & 0.01 & 1.00 \end{pmatrix} \tag{4.13}$$

In the model for run2b, we use the variables H, L, $\log p_T(\mu)$, η^8, η^6, and η^4, L*$\log p_T(\mu)$. L*$\log p_T(\mu)$, an interaction term, limits the contribution of the $\log p_T(\mu)$ term to the cases where the muon transverse momentum is low. In this case the intercept, β_0, is consistent with zero within two standard deviations and so we do not include it in the model. The vector of the coefficients, $\boldsymbol{\beta}$, and the covariance matrix, $\mathbf{V} = \mathbf{SRS}$, are

$$\boldsymbol{\beta} = \begin{pmatrix} -2.30 & 0.17 & -20.80 & -0.85 & 2.85 & -1.85 & 7.71 \end{pmatrix} \tag{4.14}$$

$$\mathbf{S} = \text{diag}(0.220,\ 0.024,\ 3.065,\ 0.126,\ 0.505,\ 0.502,\ 1.201) \tag{4.15}$$

$$\mathbf{R} = \begin{pmatrix} 1.00 & -0.18 & 0.01 & -0.01 & 0.02 & -0.03 & 0.00 \\ -0.18 & 1.00 & 0.01 & -0.41 & 0.46 & -0.53 & -0.02 \\ 0.01 & 0.01 & 1.00 & 0.09 & -0.09 & 0.07 & -1.00 \\ -0.01 & -0.41 & 0.09 & 1.00 & -0.99 & 0.94 & -0.09 \\ 0.02 & 0.46 & -0.09 & -0.99 & 1.00 & -0.98 & 0.09 \\ -0.03 & -0.53 & 0.07 & 0.94 & -0.98 & 1.00 & -0.07 \\ 0.00 & -0.02 & -1.00 & -0.09 & 0.09 & -0.07 & 1.00 \end{pmatrix} \tag{4.16}$$

Figure 4.5 shows a comparison of the trigger efficiency predictions of the GLM and the prediction of the ratio of triggered to untriggered events for the four permutations of the two binary variables. The muon p_T is set to 30.0 GeV/c and 12.5 GeV/c for the plots showing the high and low transverse momentum muon cases respectively. Figure 4.6 compares the distributions of data events passing the single MU triggers OR requirement to Monte Carlo

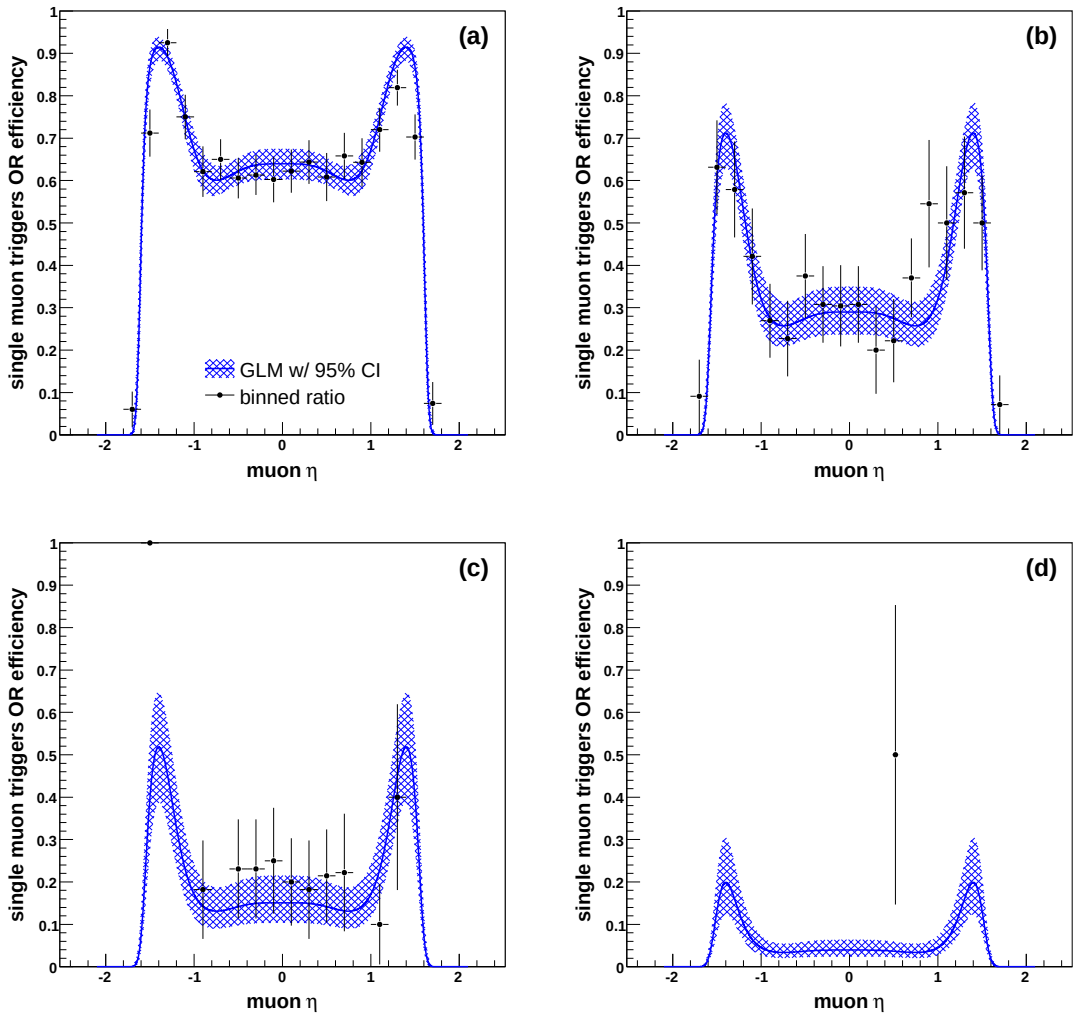

Figure 4.5: A comparison of the ratio of triggered to untriggered events (points) to the single MU triggers OR probability predicted by the GLM (smooth curve) for the cases: a) muon p_T = 30.0 GeV/c for the GLM, > 15.0 GeV/c for the points, and did not pass through the hole in the muon system; b) muon p_T = 12.5 GeV/c for the GLM, < 15.0 GeV/c for the points, and did not pass through the hole in the muon system; c) muon has p_T= 30.0 GeV/c for the GLM, > 15.0 GeV/c for the points, and did pass through the hole in the muon system; d) muon has p_T = 12.5 GeV/c for the GLM, < 15.0 GeV/c for the points, and did pass through the hole in the muon system. All models are derived from the set of all events in the analysis data that fired at least one single EM trigger. Plots shown use the run2b data.

events without and with the GLM applied as a correction.

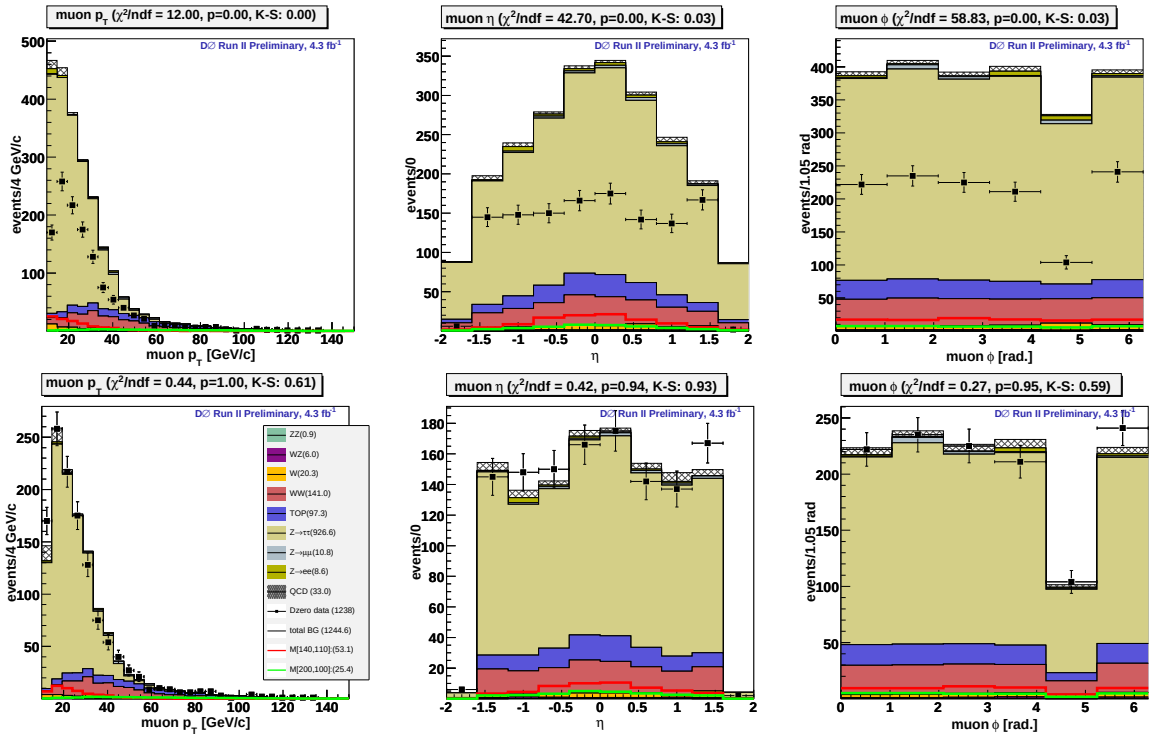

Figure 4.6: A comparison of data (points) to Monte Carlo estimates (colored histograms) without (top row) and with (bottom) the single muon triggers OR efficiency correction applied. The data events are required to have fired at least one single muon trigger. From left to right, the plots show muon transverse momentum, muon η, and muon ϕ. Plots shown use run2b data and Monte Carlo.

4.6.3 Single EM Triggers OR and Single Muon Triggers OR

In order to estimate the efficiency of requiring either a single EM or a single muon trigger, we need to first estimate the efficiency of requiring both. In the uncorrelated case, the "and" efficiency, $\hat{\epsilon}_{e\cap\mu}$, is the product of the individual efficiencies

$$\hat{\epsilon}_{e\cap\mu} = \hat{\epsilon}_e \hat{\epsilon}_\mu. \tag{4.17}$$

Figure 4.7 show the distributions of data events that fired a single EM trigger and a single muon trigger to Monte Carlo events without and with $\hat{\epsilon}_{e\cap\mu}$ applied as a correction. Even in this "and" case in which the trigger effects are the largest, the agreement between data and the corrected Monte Carlo is very good. These plots simultaneously test the single EM trigger OR GLM, the single muon triggers OR GLM, and the correlation between the two. The good agreement shows that both models are effective and that the correlations are small.

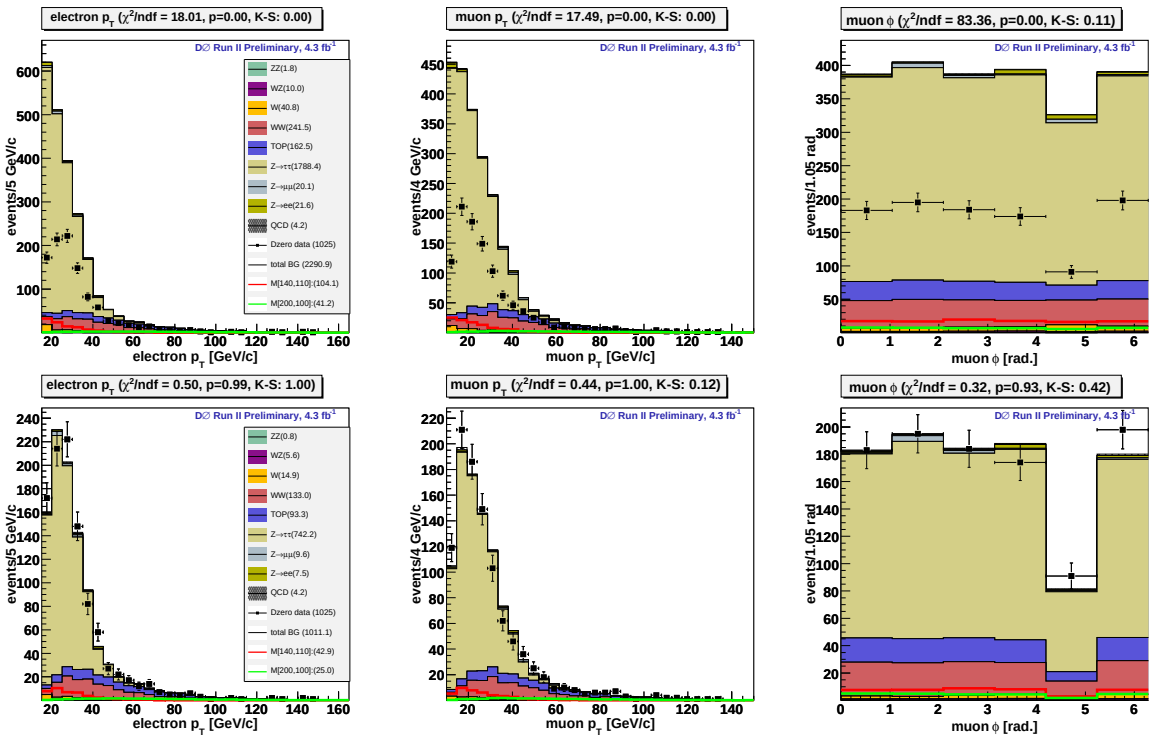

Figure 4.7: A comparison of data (points) to Monte Carlo estimates (colored histograms) without (top row) and with (bottom) $\hat{\epsilon}_{e\cap\mu}$ applied as a correction. The data events are required to have fired both a single EM trigger and a single muon trigger. From left to right, the plots show electron transverse momentum, muon transverse momentum, and muon ϕ. Plots shown use run2b data and Monte Carlo.

4.6.4 Single EM Triggers OR or Single Muon Triggers OR

Again assuming the uncorrelated case, the efficiency of requiring either a single EM trigger or a single muon trigger, $\epsilon_{e\cup\mu}$, is

$$\hat{\epsilon}_{e\cup\mu} = \hat{\epsilon}_e + \hat{\epsilon}_\mu - \hat{\epsilon}_e\hat{\epsilon}_\mu. \tag{4.18}$$

Figure 4.8 compares the distributions of data events that fired at least one single EM or single muon trigger to Monte Carlo events without and with $\hat{\epsilon}_{e\cup\mu}$ applied as a correction. For Monte Carlo events used in this analysis, we calculated $\hat{\epsilon}_{e\cup\mu}$ and applied it as a correction. The systematic uncertainties are given in Section 5.4.

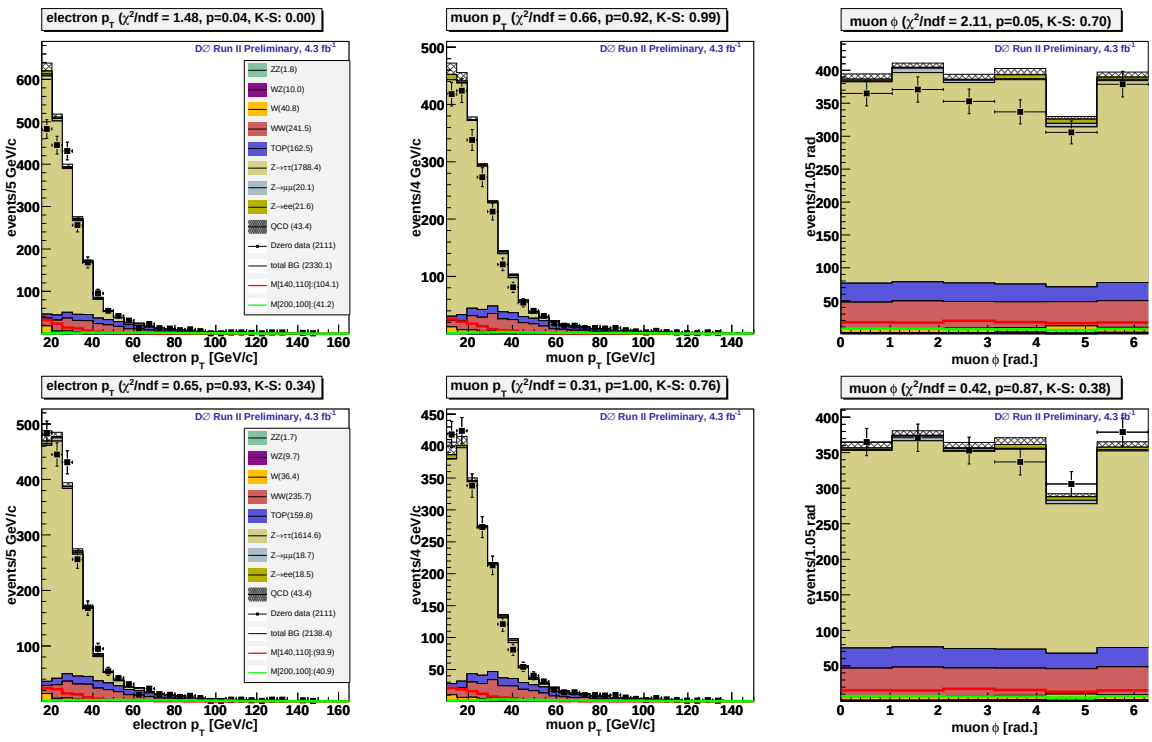

Figure 4.8: A comparison of data (points) to Monte Carlo estimates (colored histograms) without (top row) and with (bottom) $\hat{\epsilon}_{e\cup\mu}$ applied as a correction. The data events are required to have fired at least one single EM or single muon trigger. From left to right, the plots show electron transverse momentum, muon transverse momentum, and muon ϕ. Plots shown use run2b data and Monte Carlo.

4.7 QCD Sample

Because hadronic jets are sometimes reconstructed as electrons and often produce muons as decay products, events with multiple jets produce a significant background in the electron+muon decay channel. We refer to these events as QCD events since they are described by the theory of Quantum Chromodynamics. We model QCD events using a sample of DØ data events orthogonal to the analysis sample. To produce the orthogonal sample, we selected events which met all the preselection requirements except that the electron likelihood was required to be less than 0.2 and muons were required to have scaled track cone and scaled calorimeter halo values in the range [0.15,0.35]. As in the analysis sample, the electron and the muon were required to have opposite charge. We denote this sample $D_{RR}^{\pm\mp}$ since it is comprised of data events which have a rejected muon and a rejected electron of opposite sign. Rejected in this case means the leptons were rejected by the standard preselection requirements.

We determined the scale factor for this sample, $S_{\rm QCD}$, using the following procedure. We calculated the ratio of QCD events that pass the electron likelihood and muon isolation requirements to those that fail both sets of requirements. Because a limited number of SM processes produce two leptons with the same charge, we calculated this ratio from a same sign sample. The largest contributor to this sample other than QCD is W+jets. Figure 4.9 shows that most of the QCD-like events represented by the $D_{RR}^{\pm\pm}$ sample have $\not\!\!E_T$ less than 20 GeV in contrast to the W+jets events of which most have $\not\!\!E_T$ greater than 20 GeV. When calculating the ratio, we used events with $\not\!\!E_T$ less than 20 GeV. To account for any remaining non-QCD events in our samples, we subtracted the number of same sign events predicted by all of the Monte Carlo samples. Our QCD scale factor $S_{\rm QCD}$ is given by the

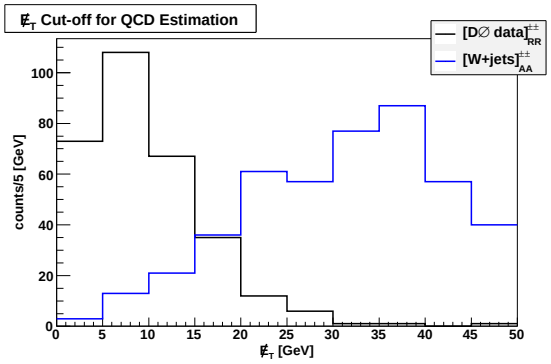

Figure 4.9: The distribution of $\not\!\!E_T$ for the $D^{\pm\pm}_{RR}$ and the W+jets same sign Monte Carlo samples.

formula

$$S_{\rm QCD} = \frac{N(D^{\pm\pm}_{AA}) - N(MC^{\pm\pm}_{AA})}{N(D^{\pm\pm}_{RR}) - N(MC^{\pm\pm}_{RR})}. \tag{4.19}$$

where N(X) indicates the number of events in sample X and the Monte Carlo (MC) and data (D) samples are labeled $\pm\pm$ for same charge leptons and RR or AA for leptons getting rejected or accepted by the electron likelihood and muon isolation requirements. Figure 4.10 compares the accepted and rejected same sign, combined run2a and run2b samples.

We estimate the uncertainty on the QCD scale factor, $\Delta S_{\rm QCD}$, using the general propagation of error formula treating the event counts for the numerator and the denominator as uncorrelated Poisson variables:

$$\Delta S^2_{\rm QCD} = \Delta[N(D^{\pm\pm}_{AA}) - N(MC^{\pm\pm}_{AA})]^2 \times \left(\frac{1}{N(D^{\pm\pm}_{RR}) - N(MC^{\pm\pm}_{RR})}\right)^2 \tag{4.20}$$

$$+\Delta\left[N(D^{\pm\pm}_{RR}) - N(MC^{\pm\pm}_{RR})\right]^2 \times \left(\frac{N(D^{\pm\pm}_{AA}) - N(MC^{\pm\pm}_{AA})}{\left[N(D^{\pm\pm}_{RR}) - N(MC^{\pm\pm}_{RR})\right]^2}\right)^2. \tag{4.21}$$

The scale factors for run2a and run2b respectively are $S_{\rm QCD} = 0.10 \pm 0.04$ and $S_{\rm QCD} = 0.14 \pm 0.04$. For the combined data set $S_{\rm QCD} = 0.13 \pm 0.03$.

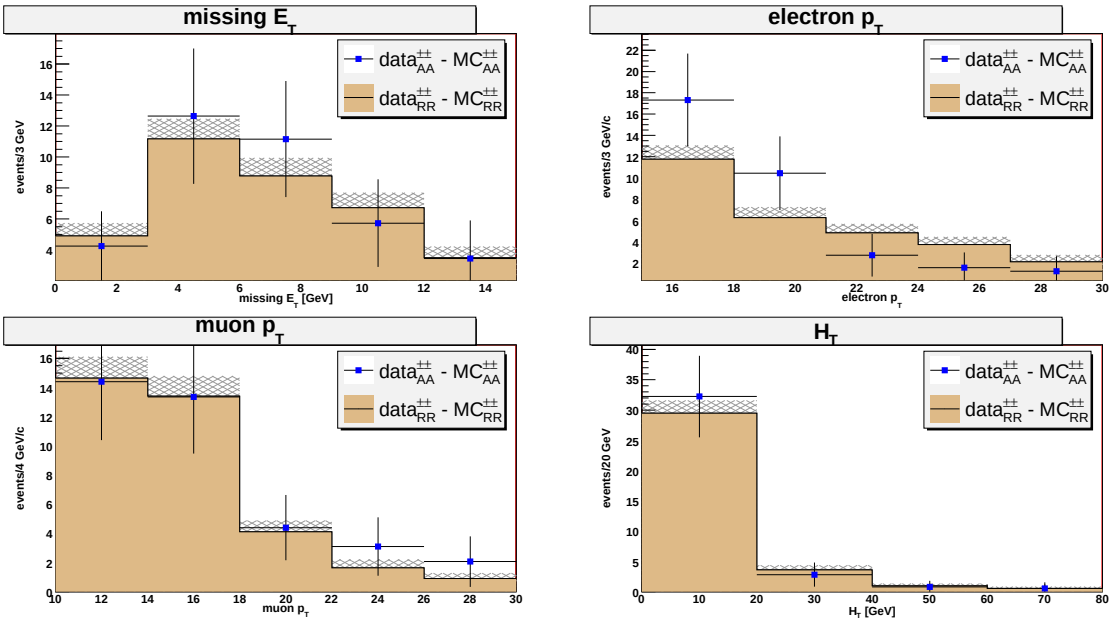

Figure 4.10: Comparison of the accepted and rejected same sign samples for combined run2a and run2b data set. The plots show $\not\!\!E_T$ (top left), electron p_T (top right), muon p_T (bottom left), and H_T (bottom right). H_T is the scalar sum the transverse momentum of the selected jets in the event. The ratio of accepted to rejected events for combination sample, 0.14, is applied to the rejected sample as a scale factor.

Using this method we estimate 1.7 ± 0.8, 23.9 ± 7.2, and 24.4 ± 6.2 QCD events for the run2a, run2b, and the combined samples after the entire preselection has been applied. The uncertainties listed here include both ΔS_{QCD} and the statistical uncertainty on the sample. The expected number of events for run2a is relatively low because the requirement that $\not\!\!E_T$ be greater than 20 GeV/c^2 applies only to that sample.

4.8 Comparison of data to background estimate at preselection level

After applying the preselection requirements to data events and the preselection requirements and corrections to the Monte Carlo events, we produced plots showing the event distributions of the run2a, run2b, and combined samples for each of the analysis variables. The combined plots (Fig. 4.11 - 4.17), are shown in this section. The plots for run2a and run2b are shown in Appendix D. In these figures we show the distribution for signal points [200,100] and [110,90] where the first number represents the top squark mass and the second sneutrino mass both in GeV/c^2. [200,100] is used as the "hard" signal benchmark since the large difference in mass causes the analysis objects to have relatively large amounts of transverse momentum. [110,90] is used as the "soft" signal benchmark since the small difference in mass causes the analysis objects to have relatively small amounts of transverse momentum.

4.8.1 Lepton and $\not\!\!E_T$ kinematic variables

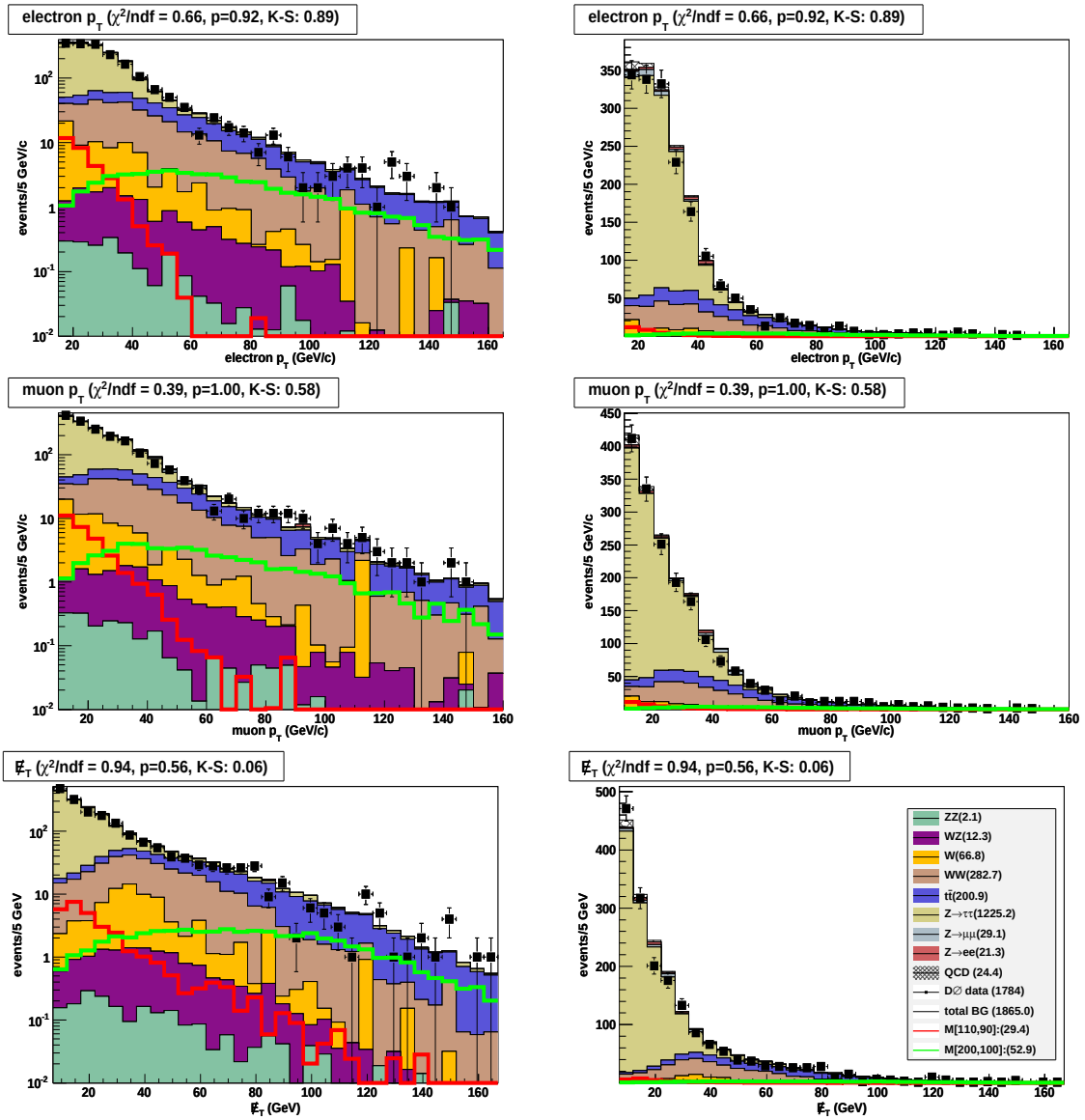

Figure 4.11: The transverse momentum of the electron (top) and muon (middle) and the missing transverse energy (bottom). M[200,100] (green) and M[110,90] (red) are the hard and soft benchmark signal samples. The DØ data event counts and the estimated events for the backgrounds and signal benchmarks are given in the legend. Plots show the combined run2a and run2b dataset.

4.8.2 Lepton and $\not\!\!E_T$ topological variables

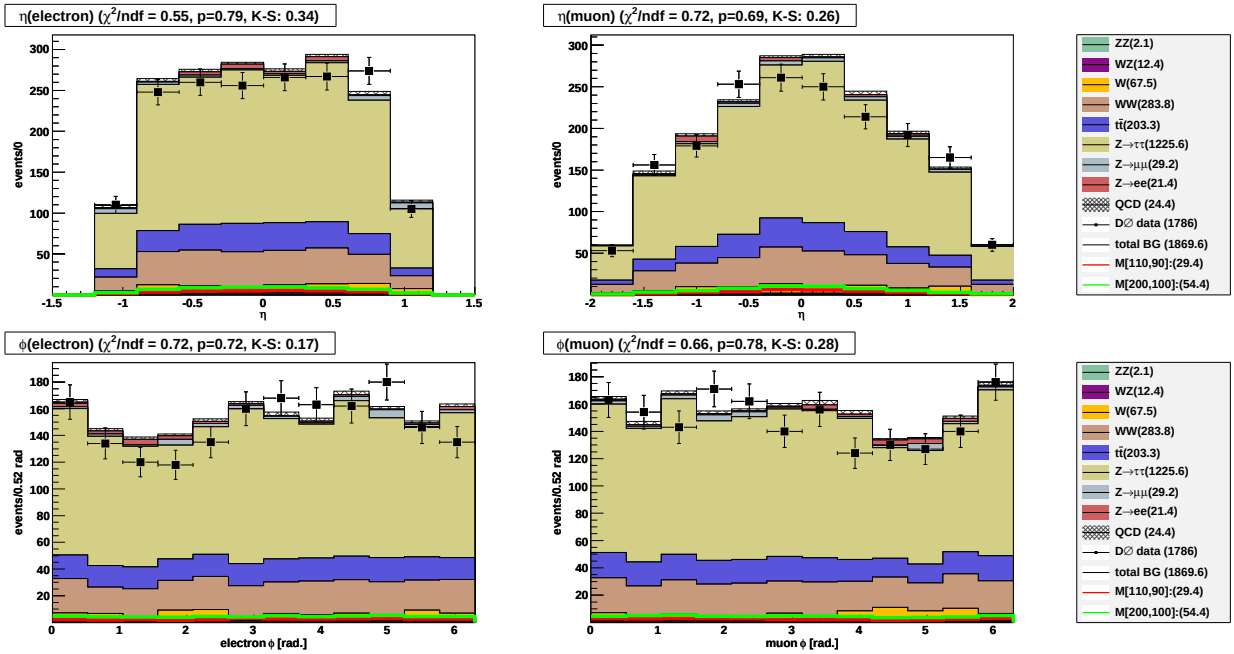

Figure 4.12: Electron (left) and muon (right) η (top) and ϕ (bottom). M[200,100] (green) and M[110,90] (red) are the hard and soft benchmark signal samples. The DØ data event counts and the estimated events for the backgrounds and signal benchmarks are given in the legend. Plots show the combined run2a and run2b dataset.

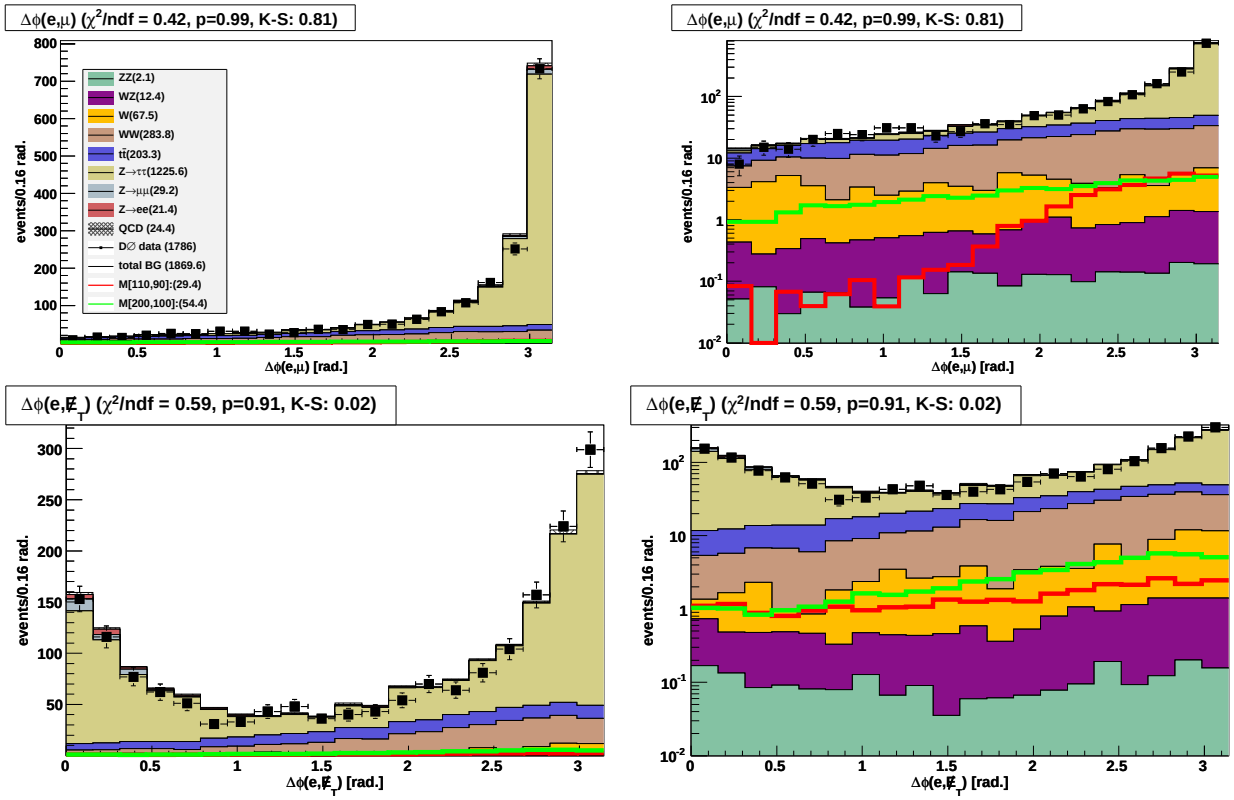

Figure 4.13: The transverse plane opening angles between the electron and the muon (top) and the electron and the missing transverse energy (bottom). M[200,100] (green) and M[110,90] (red) are the hard and soft benchmark signal samples. The DØ data event counts and the estimated events for the backgrounds and signal benchmarks are given in the legend. Plots show the combined run2a and run2b dataset.

4.8.3 Jets

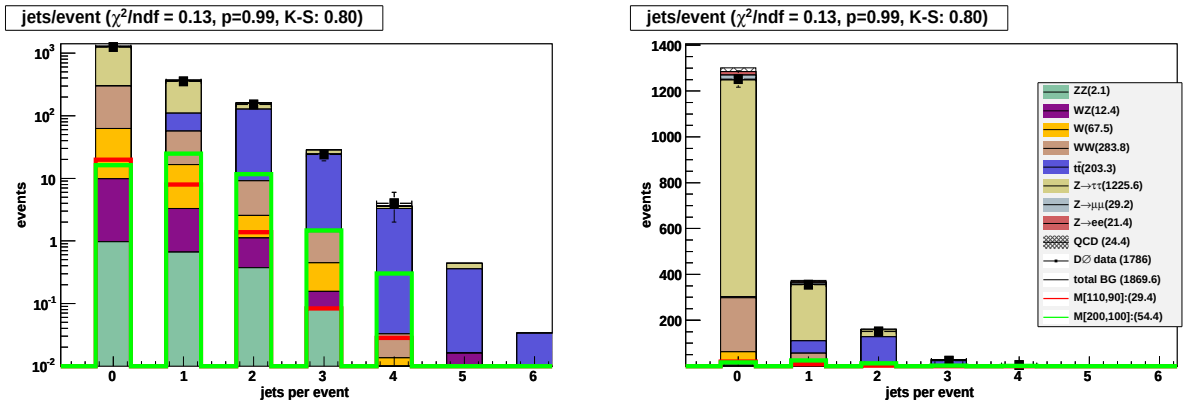

Figure 4.14: The number of jets in log (left) and linear (right) scale. M[200,100] (green) and M[110,90] (red) are the hard and soft benchmark signal samples. The DØ data event counts and the estimated events for the backgrounds and signal benchmarks are given in the legend. Plots show the combined run2a and run2b dataset.

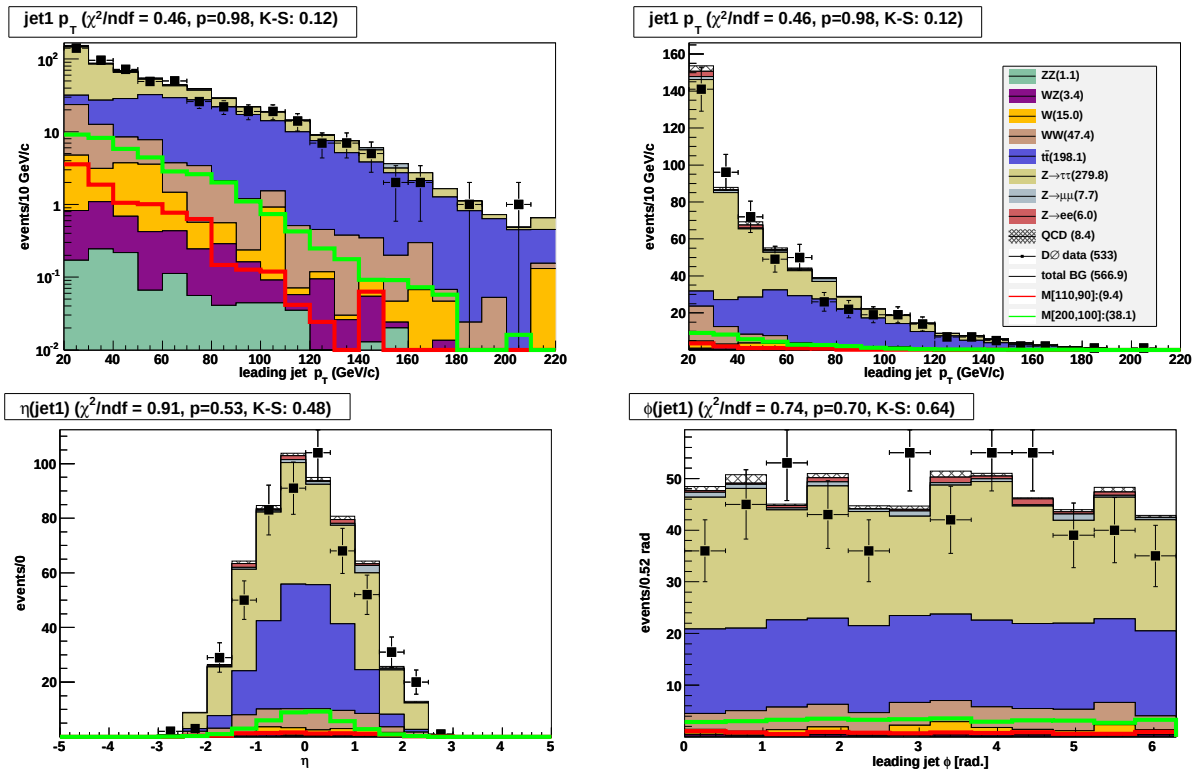

Figure 4.15: The transverse momentum of the leading jet (top) in log (left) and linear (right) scale. Also shown are the leading jet η (bottom left) and ϕ (bottom right) distributions. M[200,100] (green) and M[110,90] (red) are the hard and soft benchmark signal samples. The DØ data event counts and the estimated events for the backgrounds and signal benchmarks are given in the legend. Plots show the combined run2a and run2b dataset.

4.8.4 S_T and H_T

S_T is the scalar sum of the electron, the muon, and the $\not\!\!E_T$. H_T is the scalar sum of the transverse momentum of the jets.

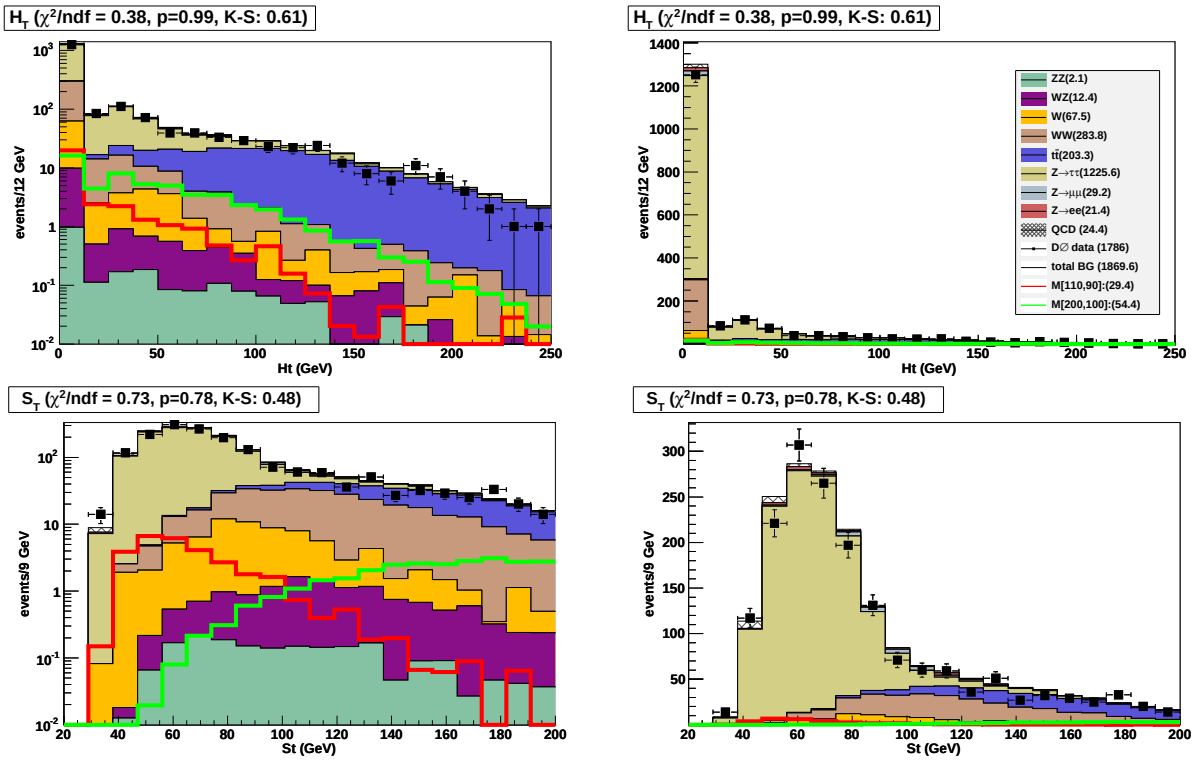

Figure 4.16: H_T(top) and S_T (bottom) in log (left) and linear(right) scale. M[200,100] (red) and M[110,90] (green) are the hard and soft benchmark signal samples The DØ data event counts and the estimated events for the backgrounds and signal benchmarks are given in the legend. Plots show the combined run2a and run2b dataset.

Luminosity

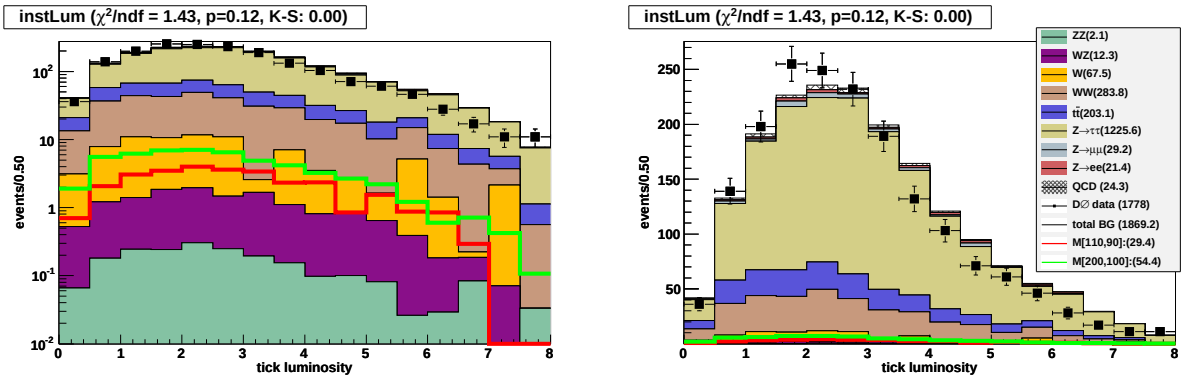

Figure 4.17: The luminosity per tick with log and linear scales for the combination data set. M[200,100] (green) and M[110,90] (red) are the hard and soft benchmark signal samples. The DØ data event counts and the estimated events for the backgrounds and signal benchmarks are given in the legend. Plots show the combined run2a and run2b dataset.

Chapter 5

Signal Selection

In our search we assume that top squarks are created in pairs and that each squark decays to a bottom quark, a sneutrino, and to either an isolated electron or an isolated muon. The difference between the masses of the top squark and the sneutrino determines the kinematics of the final state objects. A larger difference will lead to more missing energy, larger amounts of jet energy, and higher p_T charged leptons. Therefore, we optimize the selection cuts based on the value of the mass difference, ΔM, rather than the top squark and sneutrino masses. As mentioned previously, two benchmark points were chosen, [light stop mass in GeV/c^2, sneutrino mass in GeV/c^2] = [200,100] and [110,90], which will be referred to as the "hard", $\Delta M = 100$ GeV/c^2, and "soft", $\Delta M = 20$ GeV/c^2, benchmarks respectively.

The signal samples we are analyzing have ΔM values ranging from 20 to 190 GeV/c^2. For the smaller values of ΔM, $\gamma^*/Z \rightarrow \tau\bar{\tau}$ and WW are the dominant backgrounds. As ΔM gets larger, the kinematics and topology of the signal events become more like $t\bar{t}$. We needed a consistent, systematic, and powerful method for providing discrimination for the entire range of ΔM values against these three most significant backgrounds as well as several minor ones. Rather than target each background, we targeted the backgrounds in groups.

QCD, $\gamma^*/Z \to \mu\bar{\mu}$, and $\gamma^*/Z \to e\bar{e}$ along with $\gamma^*/Z \to \tau\bar{\tau}$ form Group 1. WZ, ZZ, $W+$jets and WW for Group 2. Group 3 consists of $t\bar{t}$ alone. For each value of ΔM we created three variables each customized to provide discrimination between signal events and events from one of the groups. We then used these three discriminating variables for removing background-like events and for building the histograms used in the limit setting procedure.

In this chapter we first explain a simple cut that targeted the largest background, $\gamma^*/Z \to \tau\bar{\tau}$. We then explain how we created the custom discriminant variables. Finally, we explain how we used the variables as input to the limit setting procedure.

5.1 Cut 1: Back-to-back leptons

$\gamma^*/Z \to \tau\bar{\tau}$ is the largest background after the preselection. Figure 5.1 shows that the electron and the muon in the $\gamma^*/Z \to \tau\bar{\tau}$ events are mostly back-to-back in ϕ and have relatively little amounts of $\not\!\!E_T$. To reduce this background we removed events in which

$$\Delta\phi(e,\mu) > 2.8 \qquad \text{and} \qquad \not\!\!E_T < 20 \text{ GeV}. \tag{5.1}$$

The values 2.8 and 20 GeV were initial chosen by eye. A test of the values 3.0 and 18 GeV showed no appreciable difference in the limits. The plots in Figures 5.2, 5.3, and 5.4 show that the agreement between SM expectation and the observed data was preserved after Cut 1.

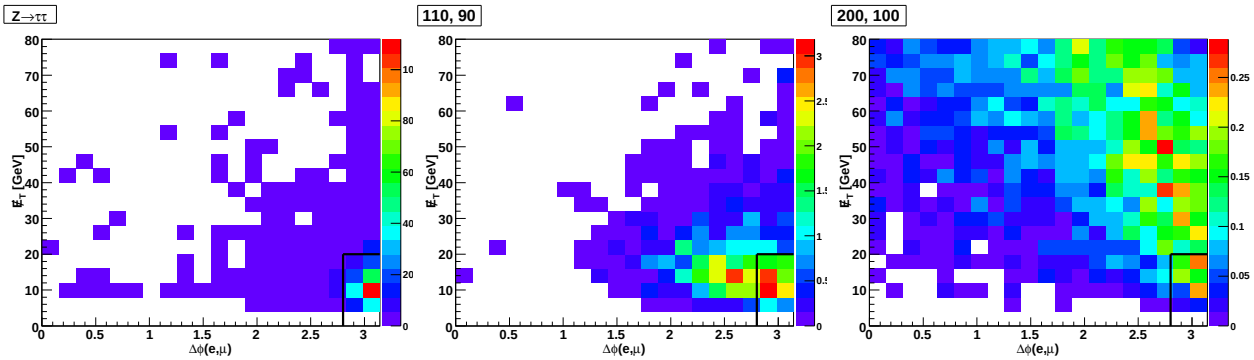

Figure 5.1: For the $\gamma^*/Z \rightarrow \tau\bar{\tau}$ Monte Carlo events the amount of $\not{E}_T$ is relatively small and the electron and muon are back-to-back, left plot. The soft (middle) and hard (right) benchmark Monte Carlo events are also shown for comparison. Cut one is represented by the black rectangle on the lower right corner of the plots. All events to the right and below the line are removed. Plots shown use the combined run2a and run2b dataset.

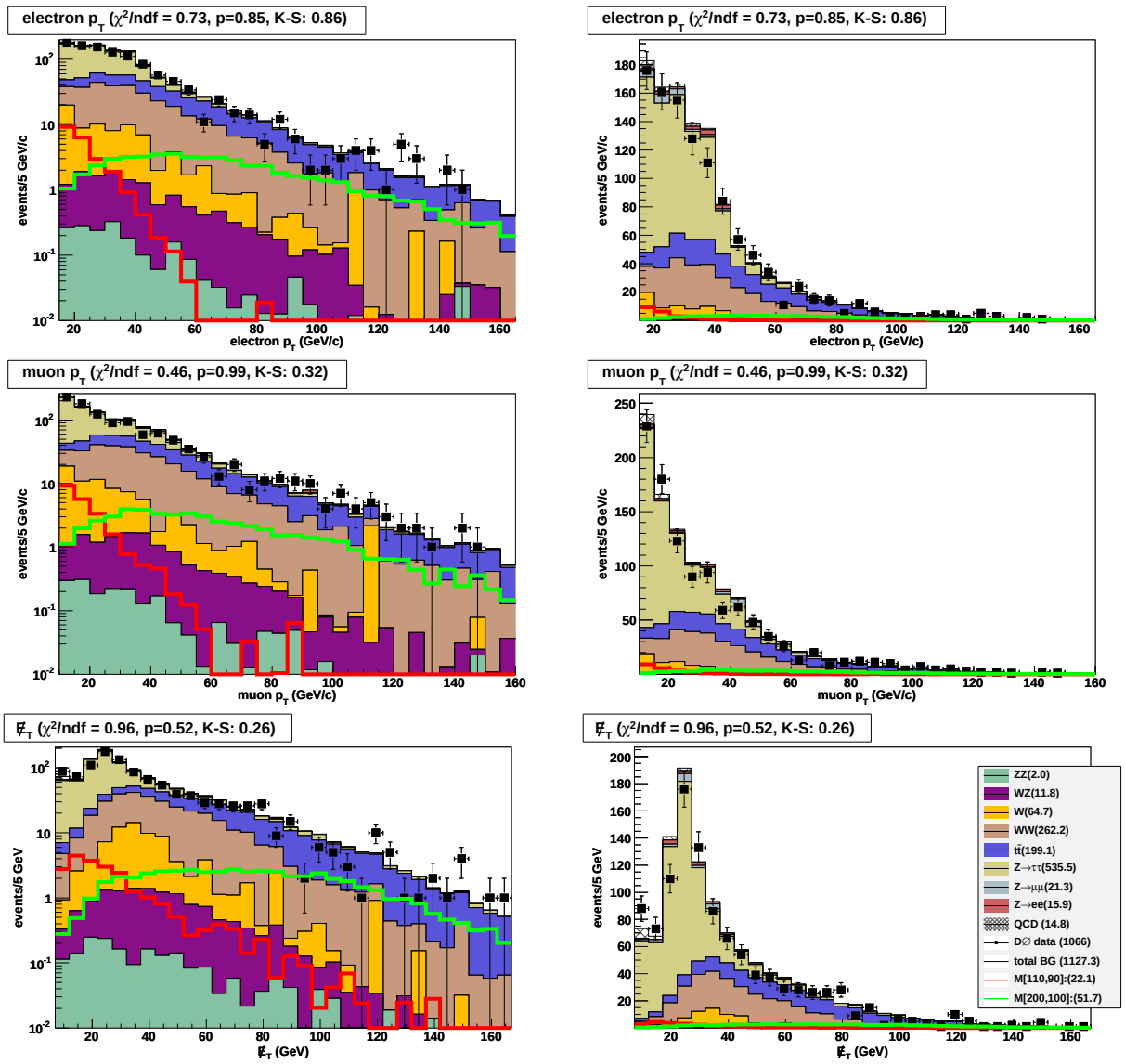

Figure 5.2: The transverse momentum of the electron (top) and muon (middle) and the missing transverse energy (bottom) for the combination data set after the analysis cuts have been applied. M[200,100] (green) and M[110,90] (red) are the hard and soft benchmark signal samples. The DØ data event counts and the estimated events for the backgrounds and signal benchmarks are given in the legend. Plots shown use the combined run2a and run2b dataset.

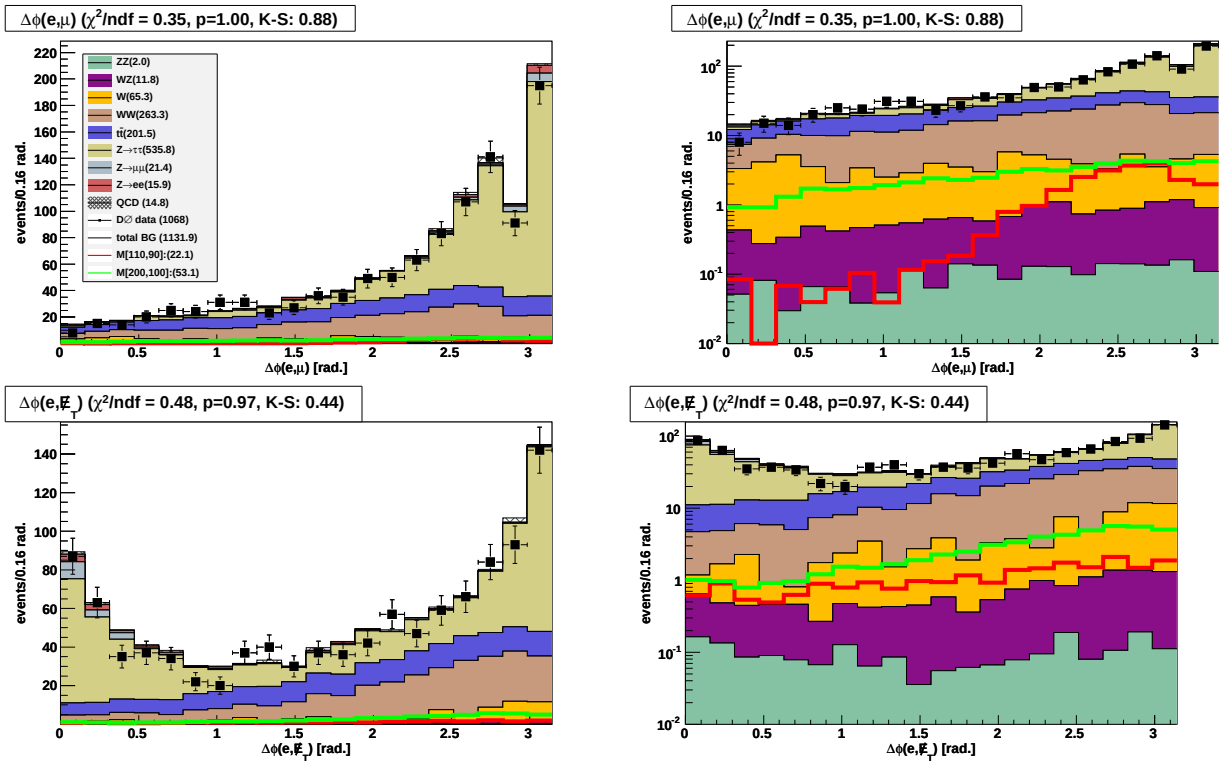

Figure 5.3: The transverse plane opening angles between the electron and the muon (top) and the electron and the missing transverse energy (bottom). M[200,100] (green) and M[110,90] (red) are the hard and soft benchmark signal samples. The DØ data event counts and the estimated events for the backgrounds and signal benchmarks are given in the legend. Plots shown use the combined run2a and run2b dataset.

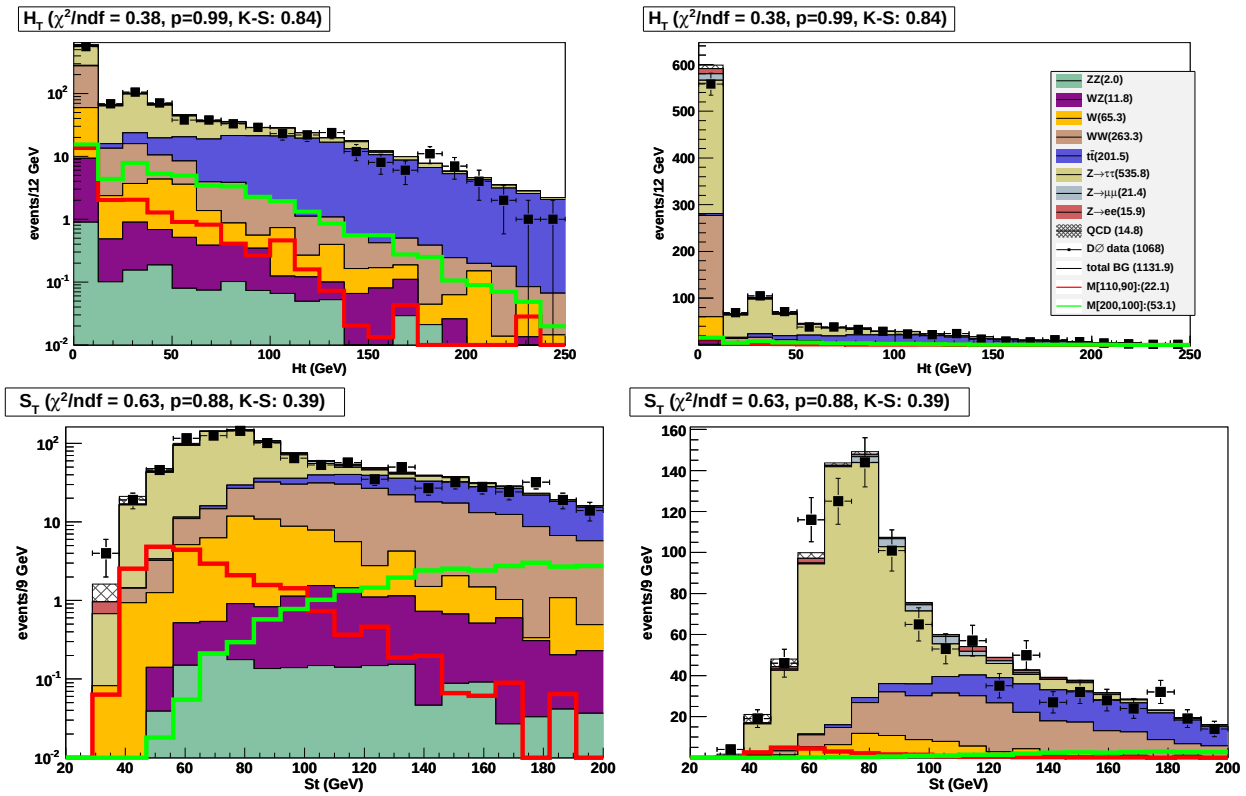

Figure 5.4: H_T(top) and S_T (bottom) in log (left) and linear(right) scale for the combination data set after the analysis cuts have been applied. M[200,100] (green) and M[110,90] (red) are the hard and soft benchmark signal samples. The DØ data event counts and the estimated events for the backgrounds and signal benchmarks are given in the legend. Plots shown use the combined run2a and run2b dataset.

5.2 Discriminant Variables

We created custom discriminant variables based on the physical characteristics of the three background groups. Group 1 (QCD, $\gamma^*/Z \rightarrow \mu\bar{\mu}$, $\gamma^*/Z \rightarrow e\bar{e}$, and $\gamma^*/Z \rightarrow \tau\bar{\tau}$) is comprised of the backgrounds which have characteristics similar to $\gamma^*/Z \rightarrow \tau\bar{\tau}$:

- The electron and the muon are usually back-to-back in ϕ.
- The measured amount of $\not\!\!E_T$ is relatively small.
- The $\not\!\!E_T$ is usually measured in the direction of one of the charged leptons.
- The charged leptons have relatively small amounts of transverse momentum.
- One or fewer selected jets.

Group 2 (WZ, ZZ, $W+$jets, and WW) is comprised of the backgrounds which have characteristics similar to WW:

- Large amounts of measured $\not\!\!E_T$.
- Usually zero jets.
- The charged leptons have relatively large amounts of transverse momentum.

Group 3 is $t\bar{t}$ which has the characteristics:

- One or more high energy jets.
- Large amounts of measured $\not\!\!E_T$.
- The charged leptons have relatively large amounts of transverse momentum.

The amount of $\not\!\!E_T$, the transverse momentum of the leptons, the transverse energy of jets, and the opening angles between the objects are the basic measured values from which we formed the analysis variables. In order to maximize the discrimination power, it is necessary to use more than one variable at a time. A linear combination of variables commonly used for discrimination is S_T, the sum

$$S_T = \not\!\!E_T + p_T(e) + p_T(\mu). \tag{5.2}$$

The coefficients in this linear combination are implicitly set to unity. We generalized the concept of using a linear combination of basic variables by allowing the coefficients to be different than unity. Additionally, we looked to tune the coefficients, to use more variables than the original three, and to apply simple transformations to the variables where appropriate. For our variable for Group 1, S'_T, we use the vector of variables

$$\mathbf{x} = \begin{pmatrix} 1 \\ \log p_T(e) \\ \log p_T(\mu) \\ \log \not\!\!E_T \\ \Delta\phi(e,\mu) \\ \Delta\phi(e,\not\!\!E_T) \\ \Delta\phi(\mu,\not\!\!E_T) \\ \Delta\phi(e,\not\!\!E_T) \times \Delta\phi(\mu,\not\!\!E_T) \end{pmatrix}. \tag{5.3}$$

We considered a large number of variables for use as discriminators but we only used those listed in Table 5.1 because they are relatively simple and highly effective. These variables were chosen to provide discrimination between the signal and Group 1.

In order to find an effective set of coefficients, we again consider a logistic Generalized Linear Model, but this time one that predicts the probability of an event being signal. This

variable name	description
$\not\!\!E_T$	missing transverse energy
$p_T(e)$	transverse momentum of the electron
$p_T(\mu)$	transverse momentum of the muon
$\Delta\phi(e,\mu)$	the opening angle in the transverse plane between the electron and the muon
$\Delta\phi(e,\not\!\!E_T)$	the opening angle in the transverse plane between the electron and the missing transverse energy
$\Delta\phi(\mu,\not\!\!E_T)$	the opening angle in the transverse plane between the muon and the missing transverse energy
$\Delta\phi(e,\not\!\!E_T) \times \Delta\phi(\mu,\not\!\!E_T)$	the product of the lepton, missing transverse energy opening angles
numJets	the number of selected jets in the event
$p_T(jet1)$	transverse energy of the most energetic jet
$p_T(jet2)$	transverse energy of the second most energetic jet
H_T	scaler sum of the transverse momentum of all the selected jets
$WWtag$	$\sqrt{(p_T(e)_x + p_T(\mu)_x + \not\!\!E_{T\,x})^2 + (p_T(e)_y + p_T(\mu)_y + \not\!\!E_{T\,y})^2}$

Table 5.1: The variables used for discriminating between signal and background events.

model takes the form

$$\text{logit}(p(s)) = \log\frac{p(s)}{1-p(s)} = \beta_0 + \sum_{i=1}^{k}\beta_i x_i \tag{5.4}$$

where k is the number of variables used in the model. $p(s)$ is the binomial probability that an event from the combined signal and background training samples is signal. We did not use $p(s)$ directly, but instead plugged $\mathbf{x}$ into the right-hand-side of eq. 5.4. We used the R software package [74] to calculate the coefficient vector β for a run2b signal Monte Carlo sample representing a ΔM value and an equal number of $\gamma^*/Z \to \tau\bar{\tau}$ events. The $\gamma^*/Z \to \tau\bar{\tau}$ events were chosen at random from the sample covering γ^*/Z mass range 75 to 130 GeV/c^2 and without charm or bottom quarks jets. We used this sample because it represents most of the $\gamma^*/Z \to \tau\bar{\tau}$ background events in our search data and because including other $\gamma^*/Z \to \tau\bar{\tau}$ event types would require event weighting in order to keep them in the proper proportions. Our variable S'_T is

$$S'_T = \beta_0 + \sum_{i=1}^{7}\beta_i x_i \tag{5.5}$$

We repeated this procedure for multiple values of ΔM. The coefficients for each and the signal used in the calculations are listed in Table 5.2.

ΔM GeV/c^2	signal [GeV/c^2,GeV/c^2]	intercept	$\log p_T(e)$	$\log p_T(\mu)$	$\log \not\!\!E_T$	$\Delta\phi(e,\mu)$	$\Delta\phi(e,\not\!\!E_T)$	$\Delta\phi(\mu,\not\!\!E_T)$	$\Delta\phi(e,\not\!\!E_T)\times$ $\Delta\phi(\mu,\not\!\!E_T)$
20	[150,130]	1.01	-1.96	-1.01	1.06	-0.33	1.16	1.25	1.37
30	[110,80]	-9.41	0.34	0.09	1.34	-1.07	1.47	1.57	1.23
40	[140,100]	-17.81	1.21	1.00	1.77	-0.70	1.45	1.52	1.29
50	[150,100]	-22.69	2.03	1.36	1.97	-0.31	1.07	1.14	1.39
60	[160,100]	-26.11	2.70	1.68	1.94	-0.46	1.28	1.40	1.12
70	[170,100]	-29.02	2.74	1.98	2.36	-0.37	1.23	1.30	1.20
80	[180,100]	-32.90	3.26	2.19	2.61	-0.48	1.45	1.53	1.03
90	[180,90]	-34.41	3.38	2.46	2.59	-0.10	1.05	1.06	1.29
100	[180,80]	-38.71	4.04	3.10	2.59	-0.70	1.66	1.57	0.80
140	[200,60]	-41.80	4.18	3.53	2.81	-0.57	1.45	1.26	0.85

Table 5.2: The values of the coefficient vector β used in discriminant variable δZ for each value of ΔM. The second column lists the [stop mass, sneutrino mass] signal sample which we used when determining the coefficients.

Since our variable S'_T is designed to discriminate between signal and $\gamma^*/Z \to \tau\bar{\tau}$ events, we gave it a more meaningful name, $\delta Z([\Delta M])$. The distributions for $\delta Z(20)$ and $\delta Z(100)$ are shown in Figures 5.5 and 5.6.

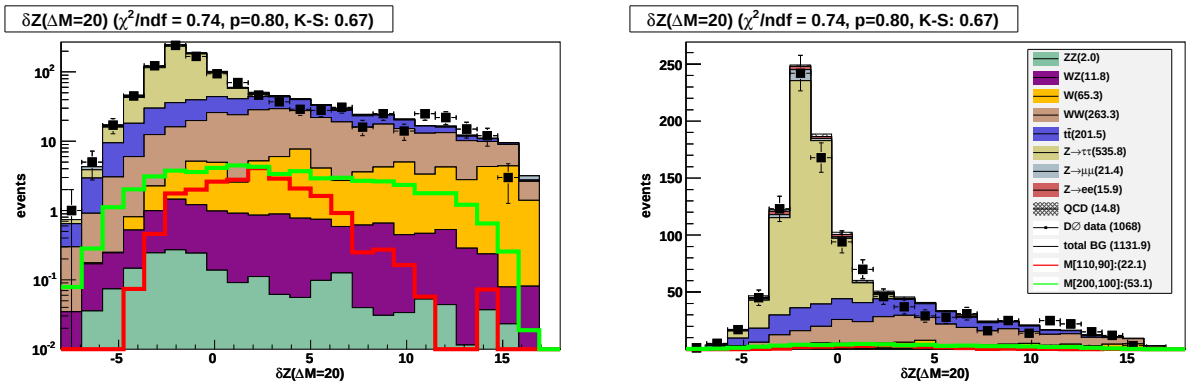

Figure 5.5: The distribution of events in log (left) and linear (right) scale for $\delta Z(20)$, a linear combination of variables designed to provide discrimination between $\Delta M = 20$ GeV/c^2 signal events and $\gamma^*/Z \to \tau\bar{\tau}$ background events.

We repeated the procedure used to create $\delta Z([\Delta M])$ to create $\delta WW([\Delta M])$ and $\delta t\bar{t}([\Delta M])$ which are designed to separate signal events from background groups 2 and 3 respectively. Since WW events usually do not have selected jets, only the charged leptons should signif-

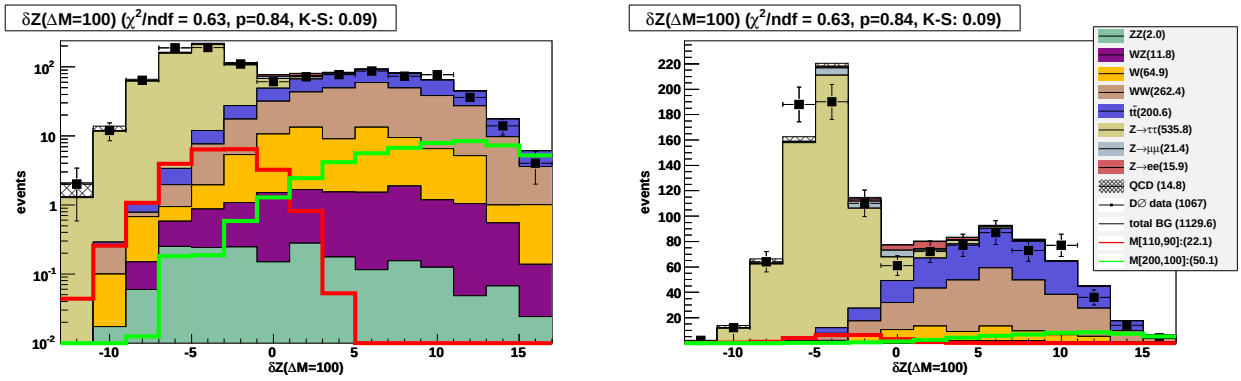

Figure 5.6: The distribution of events in $\delta Z(100)$, a linear combination of variables designed to provide discrimination between $\Delta M = 100$ GeV/c^2 signal events and $\gamma^*/Z \rightarrow \tau\bar{\tau}$ background events.

icantly contribute to the $\not\!\!E_T$ calculation. Thus, the vector sum of the $\not\!\!E_T$ and the lepton transverse momenta should be close to zero. We call this sum $WWtag$ and use it to discriminate against background group 2. In order to discriminate against top quark pair events, we use a variable called H_T which is the scalar sum of the transverse energies of the selected jets. The variables, coefficients, and signal samples for the discriminant variables are listed in Table 5.3 and Table 5.4. For $\Delta M = 110$ GeV/c^2 we use the $\Delta M = 100$ coefficients. For $\Delta M > 110$ GeV/c^2 we use the $\Delta M = 140$ GeV/c^2 coefficients. In the regression calculations we used events randomly selected from the WW and the top quark pairs to two charged leptons, two neutrinos, and two bottom quark samples.

ΔM GeV/c^2	signal [GeV/c^2,GeV/c^2]	intercept	numJets	$\log p_T(e)$	$\log p_T(\mu)$	$\log \not\!\!E_T$	$\Delta\phi(e,\mu)$	logWWtag
20	[150,130]	21.49	0.89	-4.24	-3.92	-0.72	2.96	0.09
30	[110,80]	13.59	0.55	-2.23	-2.01	-0.87	1.10	0.45
40	[140,100]	7.75	0.47	-1.34	-1.39	-0.32	0.71	0.51
50	[150,100]	2.01	0.63	-0.69	-0.65	0.09	0.36	0.59
60	[160,100]	-2.68	0.73	-0.04	-0.16	0.33	0.16	0.62
70	[170,100]	-6.42	0.82	0.40	0.24	0.56	-0.01	0.63
80	[180,100]	-9.95	0.90	0.85	0.55	0.74	-0.17	0.69
90	[180,90]	-12.75	1.01	1.09	0.82	0.93	-0.25	0.71
100	[180,80]	-14.59	1.00	1.28	0.99	0.99	-0.32	0.79
140	[200,60]	-20.74	1.12	1.84	1.55	1.28	-0.49	0.86

Table 5.3: The values of the coefficient vector β used for discriminant variable δWW for each value of ΔM. The second column lists the [stop mass, sneutrino mass] signal sample which we used when determining the coefficients.

ΔM GeV/c^2	signal [GeV/c^2,GeV/c^2]	intercept	$\log(1+H_T)$	$\log p_T(e)$	$\log p_T(\mu)$	$\log \not{E}_T$	$(numJets>1)$ $*jet2Pt$	WWtag
20	[150,130]	28.39	-0.46	-3.58	-2.62	-1.32	-0.06	-0.02
30	[110,80]	22.49	-0.51	-2.36	-1.86	-1.17	-0.06	-0.03
40	[140,100]	17.29	-0.41	-1.57	-1.32	-0.89	-0.06	-0.04
50	[150,100]	12.57	-0.32	-1.04	-0.82	-0.50	-0.05	-0.04
60	[160,100]	8.68	-0.34	-0.51	-0.43	-0.31	-0.05	-0.04
70	[170,100]	5.34	-0.29	-0.23	-0.17	-0.02	-0.04	-0.04
80	[180,100]	1.59	-0.28	0.12	0.13	0.27	-0.04	-0.04
90	[180,90]	-0.75	-0.28	0.30	0.31	0.46	-0.03	-0.03
100	[180,80]	-3.08	-0.28	0.63	0.42	0.54	-0.03	-0.03
140	[200,60]	-11.07	-0.26	1.32	1.00	1.01	-0.02	-0.02

Table 5.4: The values of the coefficient vector β used for discriminant variable $\delta t\bar{t}$ for each value of ΔM. The second column lists the [stop mass, sneutrino mass] signal sample which we used when determining the coefficients.

The distributions for $\delta WW(20)$, $\delta WW(100)$, $\delta t\bar{t}(20)$, and $\delta t\bar{t}(100)$ are shown in Figures 5.7 and 5.8.

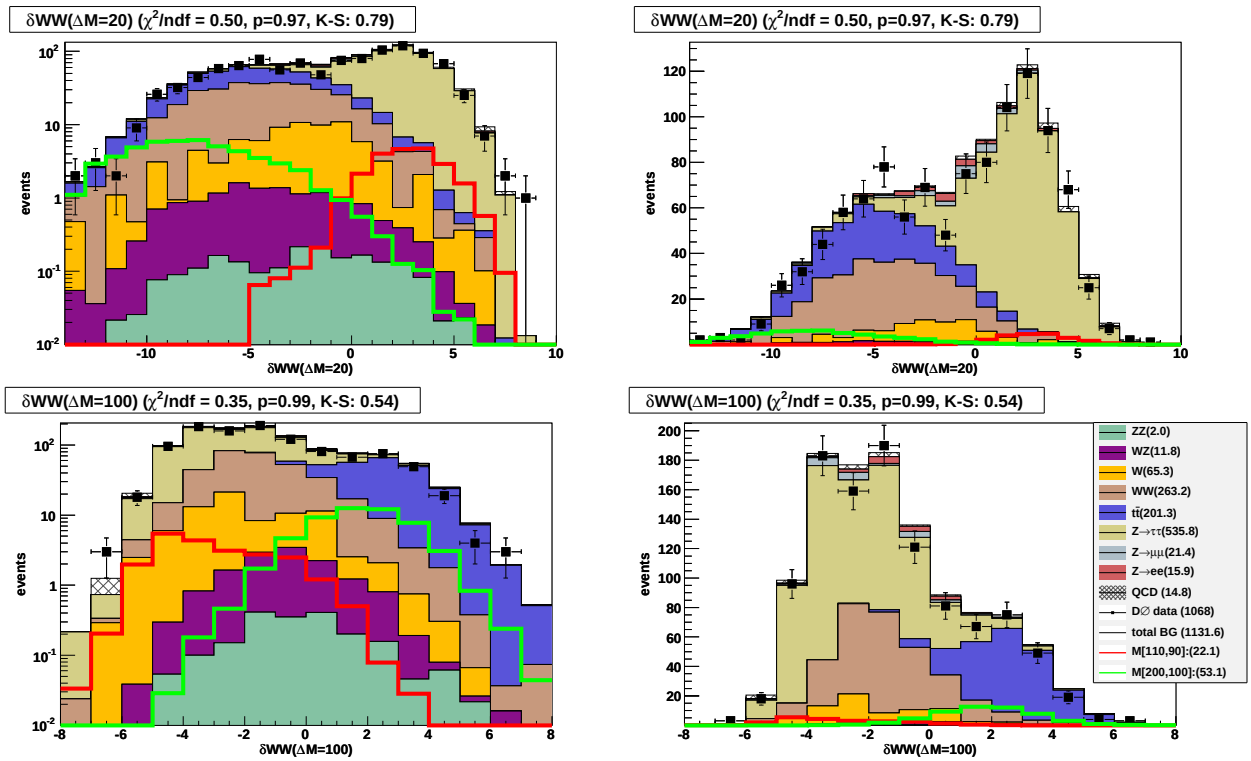

Figure 5.7: The discriminant variable $\delta WW(\Delta M)$ in log (left) and linear (right) scale for the $\Delta M = 20$ GeV/c^2 (top) and $\Delta M = 100$ GeV/c^2 (bottom) benchmarks.

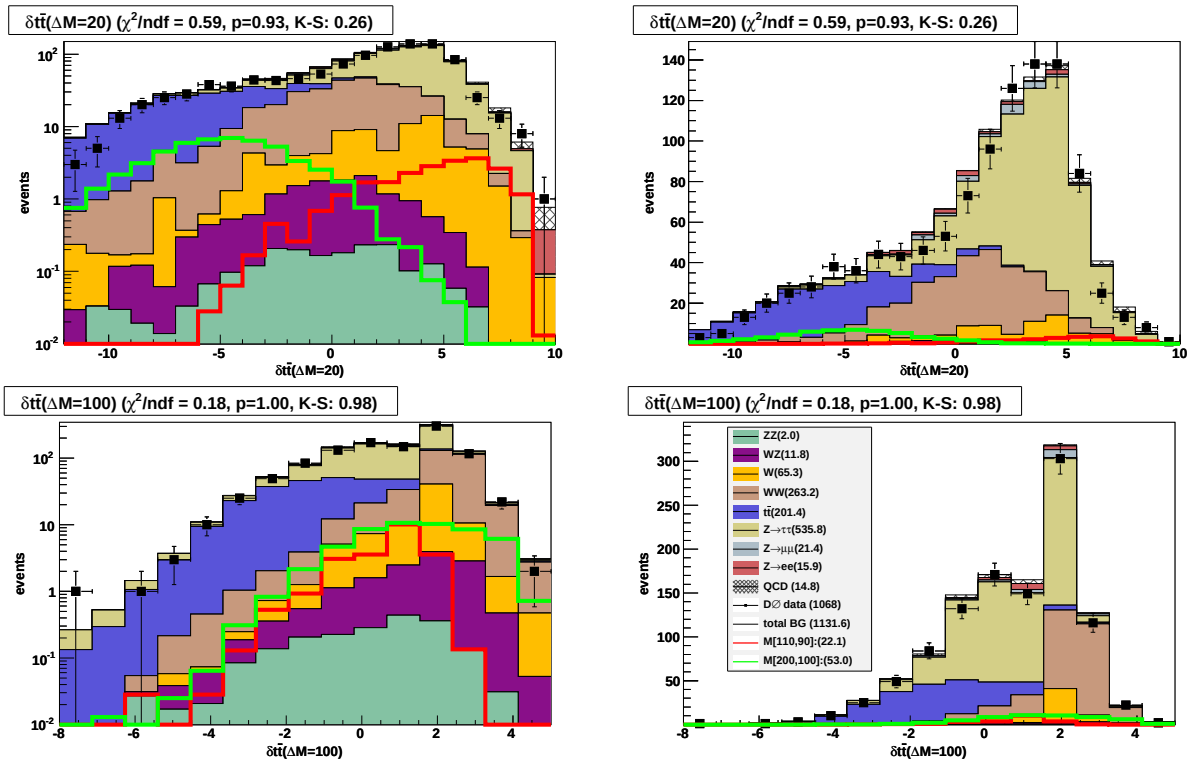

Figure 5.8: The discriminant variable $\delta t\bar{t}(\Delta M)$ in log (left) and linear (right) scale for the $\Delta M = 20$ GeV/c^2 (top) and $\Delta M = 100$ GeV/c^2 (bottom) benchmarks.

5.3 Applying the Discriminant Variables

In order to maximize signal sensitivity, we need to be able to discriminate against all the backgrounds simultaneously. We have three discriminant variables but binning events in three dimensions would give us bins which are too sparse or too coarse. Therefore, we begin by making "cut 2" on the most effective discriminator of the three. For ΔM values 20 through 60 GeV/c^2 we require

$$\delta t\bar{t} > 0. \tag{5.6}$$

For ΔM values greater than 60 GeV/c^2 we require

$$\delta Z > 0. \tag{5.7}$$

The expected numbers of background and signal events as well as the observed number of data events are listed in Tables 5.5 and 5.6 respectively. After cutting on one variable, we can bin in two dimensions with the other two variables. Figures 5.9 and 5.10 show the 2D distributions for soft and hard benchmarks and the most significant backgrounds. As these plots show, the signal events are concentrated in the upper right quadrant. For use in calculating the signal exclusion confidence limits, we bin only the upper right quadrant using bin edges {0,1,2,3,4,5,6,1000} for both the x and y axes.

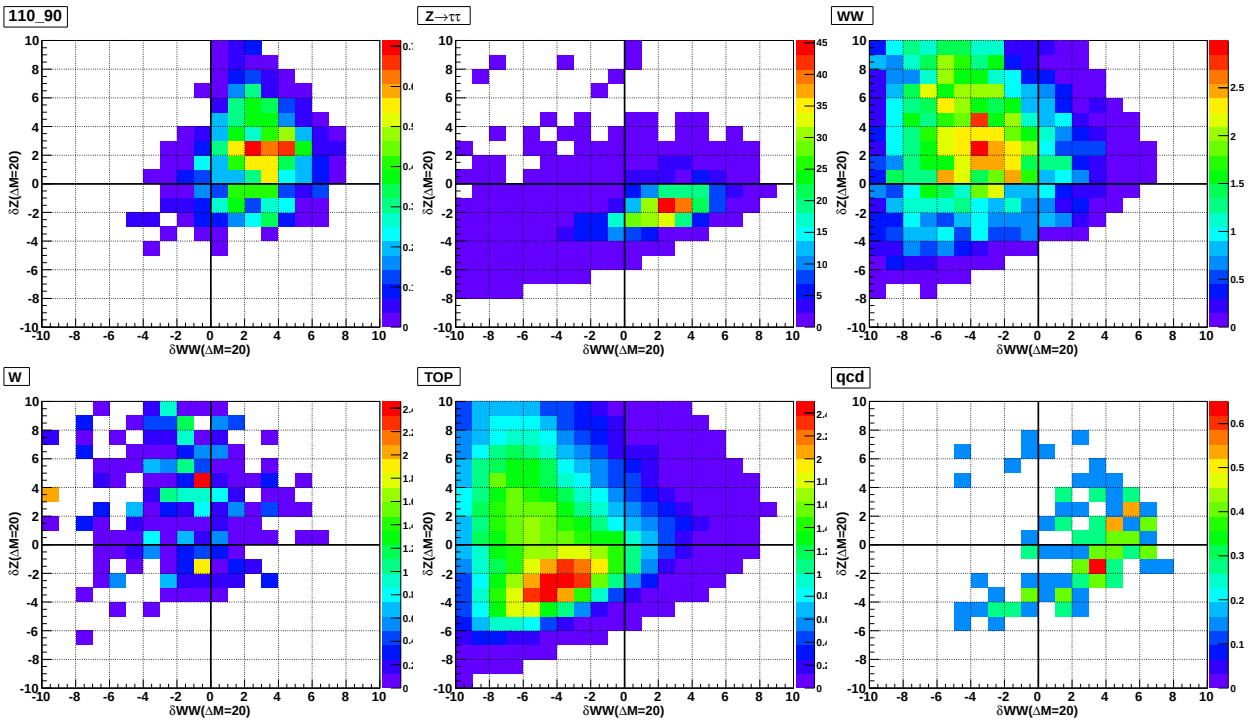

Figure 5.9: δZ vs. δWW for $\Delta M = 20$ GeV/c^2. The six plots show the soft signal benchmark (upper left), $\gamma^*/Z \to \tau\bar{\tau}$ (upper middle), WW (upper right), W (lower left), $t\bar{t}$ (lower middle), and QCD (lower right). The upper right-hand quadrant is used in the limit setting procedure.

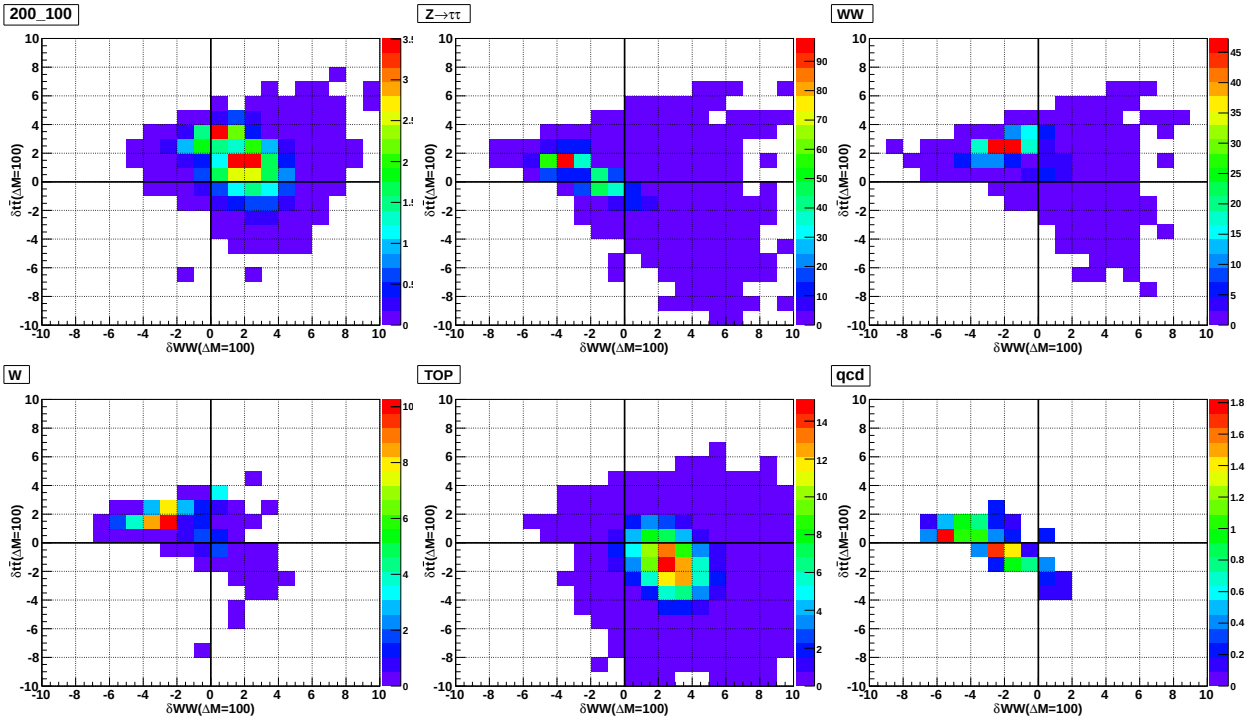

Figure 5.10: $\delta t\bar{t}$ vs. δWW for $\Delta M = 100$ GeV/c^2. The six plots show the hard signal benchmark (upper left), $\gamma^*/Z \to \tau\bar{\tau}$ (upper middle), WW (upper right), W (lower left), $t\bar{t}$ (lower middle), and QCD (lower right). The upper right-hand quadrant is used in the limit setting procedure.

	Cut 0: Preselection	**Cut 1: Back-to-back**		**Cut 2:** $\delta t\bar{t}(\Delta M = 20) > 0$		
sample	**events**	**events**	ϵ_1	**events**	ϵ_2	$\epsilon_{1,2}$
ZZ	2.09 $\pm$0.23	1.96 $\pm$0.22	0.94	0.97 $\pm$0.11	0.50	0.46
WZ	12.37 $\pm$1.45	11.81 $\pm$1.4	0.95	6.1 $\pm$0.72	0.52	0.49
W	$67.46\ ^{+6.92}_{-6.83}$	$65.35\ ^{+6.6}_{-6.5}$	0.97	$52.52\ ^{+5.4}_{-5.4}$	0.81	0.78
WW	283.75 $\pm$31.39	263.34 $\pm$29	0.93	153.05 $\pm$17	0.59	0.54
$t\bar{t}$	$203.31\ ^{+24.59}_{-28.44}$	$201.49\ ^{+24}_{-27}$	0.99	$6.33\ ^{+0.76}_{-0.9}$	0.03	0.03
$Z \to \tau\bar{\tau}$	$1225.57\ ^{+125.4}_{-123.78}$	$535.85\ ^{+55}_{-54}$	0.44	470.39 $\pm$48	0.94	0.38
$Z \to \mu\bar{\mu}$	$29.2\ ^{+2.91}_{-2.87}$	$21.39\ ^{+2.2}_{-2.1}$	0.73	$14.96\ ^{+1.5}_{-1.5}$	0.78	0.51
$Z \to e\bar{e}$	$21.37\ ^{+2.31}_{-2.28}$	15.92 $\pm$1.8	0.75	9.57 $\pm$1.2	0.68	0.45
QCD	24.44 $\pm$6.2	14.82 $\pm$3.9	0.61	13.78 $\pm$3.6	0.95	0.56
BG total	$1869.6\ ^{+131}_{-131}$	$1131.9\ ^{+67}_{-68}$	0.61	$727.66\ ^{+51}_{-51}$	0.78	0.39
data	1786	1068	0.60	702	0.79	0.39
(110,90)	$29.37\ ^{+4.9}_{-4.8}$	$22.14\ ^{+3.7}_{-3.7}$	0.75	20.48 $\pm$3.43.4	0.94	0.70
(200,100)	$54.35\ ^{+9.2}_{-9.2}$	$53.13\ ^{+8.9}_{-8.9}$	0.98	3.11 $\pm$0.510.51	0.06	0.06

Table 5.5: Summary of signal selection cuts and their efficiencies, ϵ_1 and ϵ_2. ϵ_1 and ϵ_2 are measured after the preselection cuts and correction have been applied. $\epsilon_{1,2}$ gives the combined efficiency of cuts 1 and cut 2. Cut 2 shown here uses the variable $\delta t\bar{t}(\Delta M = 20) > 0$ which provides discrimination between $t\bar{t}$ and signal events where the mass difference between the top squark and the sneutrino is 20 GeV/c^2.

	Cut 0: Preselection	**Cut 1: Back-to-back**		**Cut 2:** $\delta Z(\Delta M = 100) > 0$		
sample	**events**	**events**	ϵ_1	**events**	ϵ_2	$\epsilon_{1,2}$
ZZ	2.09 $\pm$0.23	1.96 $\pm$0.22	0.94	1.07 $\pm$0.12	0.52	0.51
WZ	12.37 $\pm$1.45	11.81 $\pm$1.4	0.95	9.21 $\pm$1.1	0.76	0.74
W	67.46 $^{+6.92}_{-6.83}$	65.35 $^{+6.6}_{-6.5}$	0.97	52.6 $^{+5.3}_{-5.2}$	0.78	0.78
WW	283.75 $\pm$31.39	263.34 $\pm$29	0.93	235 $\pm$26	0.86	0.83
$t\bar{t}$	203.31 $^{+24.59}_{-28.44}$	201.49 $^{+24}_{-27}$	0.99	178 $^{+21}_{-24}$	0.88	0.87
$Z \to \tau\bar{\tau}$	1225.57 $^{+125.4}_{-123.78}$	535.85 $^{+55}_{-54}$	0.44	16.8 $\pm$1.7	0.01	0.01
$Z \to \mu\bar{\mu}$	29.2 $^{+2.91}_{-2.87}$	21.39 $^{+2.2}_{-2.1}$	0.73	5.28 $^{+0.52}_{-0.51}$	0.18	0.18
$Z \to e\bar{e}$	21.37 $^{+2.31}_{-2.28}$	15.92 $\pm$1.8	0.75	10.0 $\pm$1.1	0.52	0.47
QCD	24.44 $\pm$6.2	14.82 $\pm$3.9	0.61	1.17 $\pm$0.48	0.05	0.05
BG total	1869.6 $^{+131}_{-131}$	1131.9 $^{+67}_{-68}$	0.61	512.0 $^{+34}_{-35.9}$	0.28	0.27
data	1786	1068	0.60	467	0.27	0.26
(110,90)	29.37 $^{+4.9}_{-4.8}$	22.14 $^{+3.7}_{-3.7}$	0.75	2.10 $\pm$0.35	0.07	0.07
(200,100)	54.35 $^{+9.2}_{-9.2}$	53.13 $^{+8.9}_{-8.9}$	0.98	51.6 $\pm$8.7	0.97	0.95

Table 5.6: Summary of the signal selection cuts and their efficiencies, ϵ_1 and ϵ_2. ϵ_1 and ϵ_2 are measured after the preselection cuts and correction have been applied. $\epsilon_{1,2}$ gives the combined efficiency of cuts 1 and cut 2. Cut 2 shown here uses the variable $\delta Z(\Delta M = 100) > 0$ which provides discrimination between γ^*/Z and signal events where the mass difference between the top squark and the sneutrino is 100 GeV/c^2.

5.3.1 Signal Efficiency

The efficiency before and after the analysis cut is shown for all signal points in Figure 5.11. Figure 5.12 compares the signal efficiency after cut 1 for run2a and run2b. Figure 5.13 shows the weighted Monte Carlo events remaining for each signal point before and after the analysis cuts have been applied.

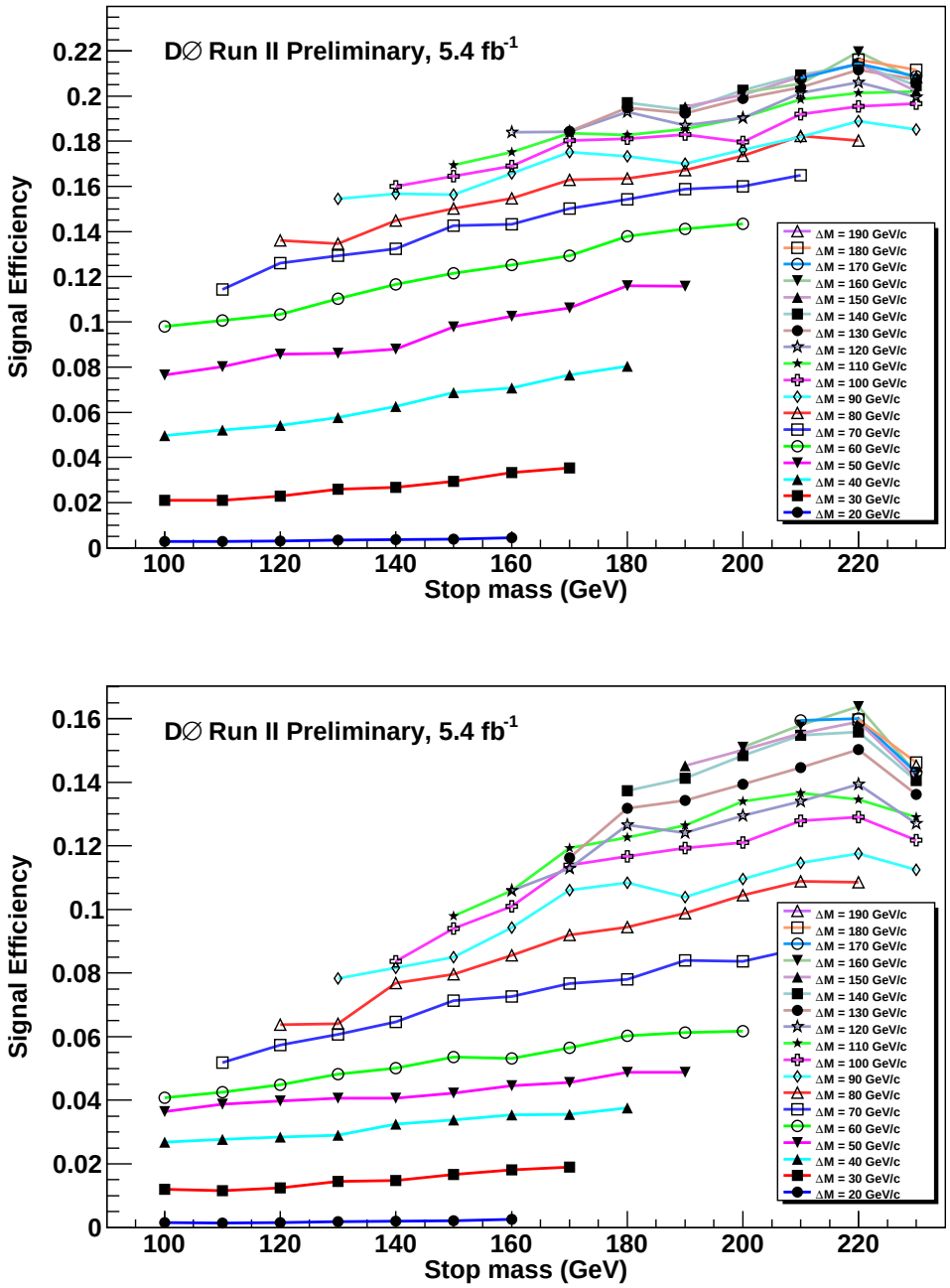

Figure 5.11: Signal efficiency after the preselection (top) and after cuts 1 and 2 have been applied (bottom).

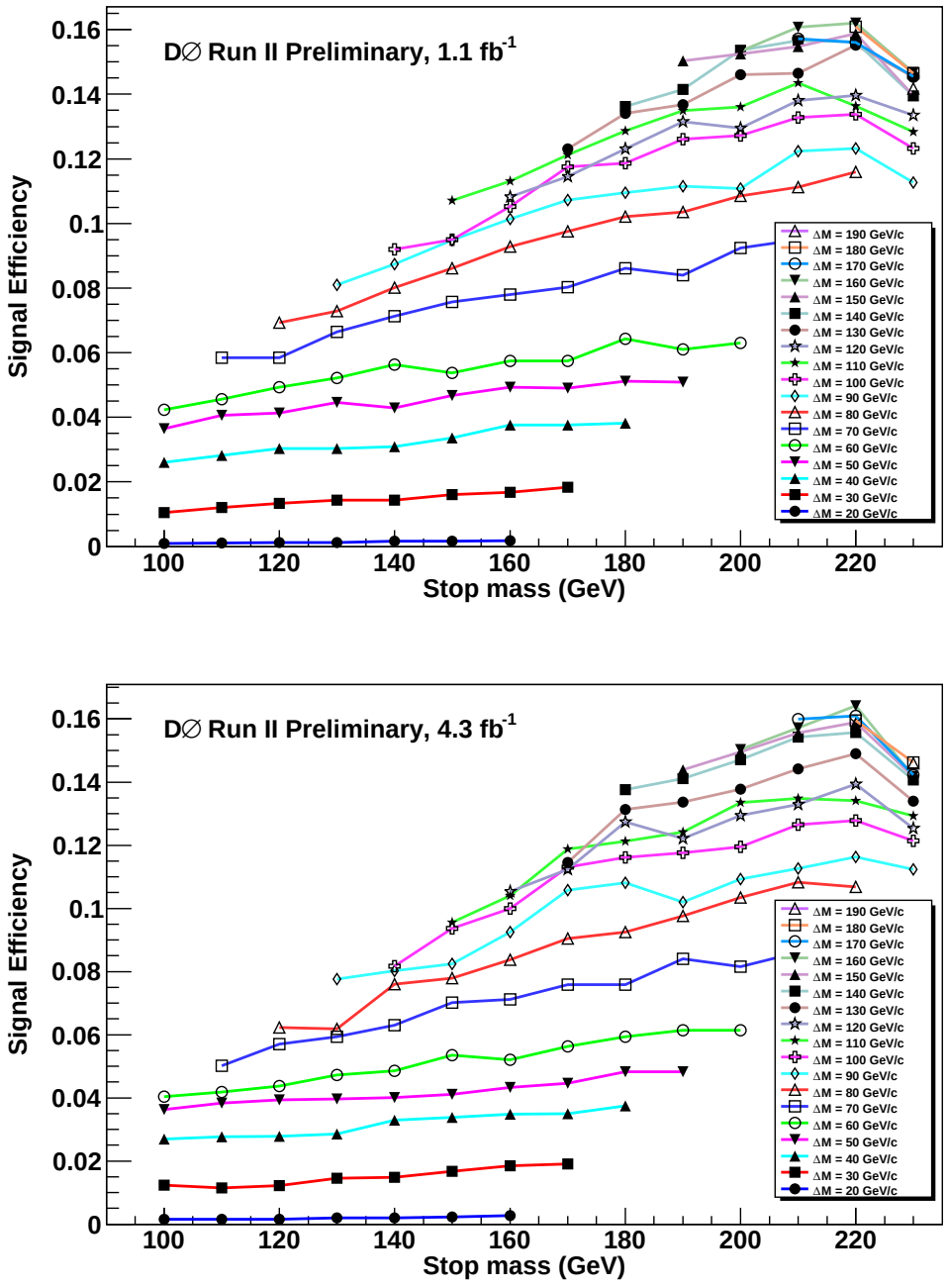

Figure 5.12: Signal efficiency after the selection for run2a and run2b.

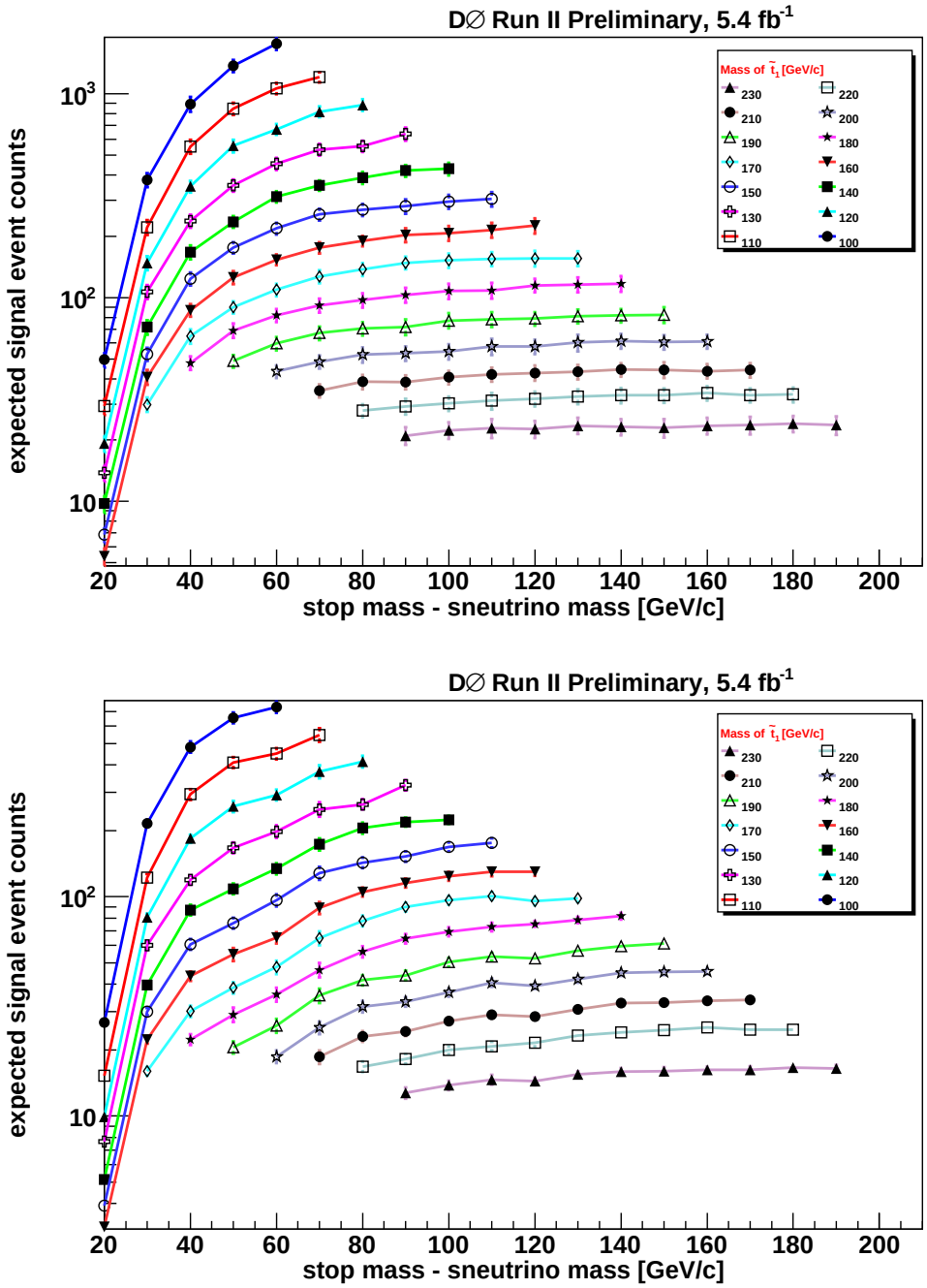

Figure 5.13: Signal Monte Carlo events after the preselection (top) and after cuts 1 and 2 have been applied (bottom).

5.4 Calculating the Limits

We used the Collie [75] software package to calculate the 95% confidence level exclusion region. In order to calculate the limits, Collie applies the CLs Method [76], see Appendix E, to histograms of the data, background, and signal events. In the calculations it includes both uniform and shape based systematic uncertainties. Uniform uncertainties are passed in as fractional scale factors. Shape dependent uncertainties are passed in as histograms with each bin set to a fractional value. The uncertainty histograms and the sample histograms must have the same bin structure. In Section 5.3 we described the bin structure. In this section we will describe the uniform and shape based uncertainties as applied in this analysis.

5.4.1 Uniformly Applied Systematic Uncertainties

These systematics are applied as uniform scale factors to entire samples. The uncertainties described here are applied to all Monte Carlo samples and are treated as correlated unless otherwise specified. The exception is the uncertainty on the QCD estimate, which is applied only to the QCD sample.

Luminosity - The uncertainty on the integrated luminosity for both run2a and run2b is ± 0.061 [77][78].

EM identification - The uncertainty for the EM ID correction in the central calorimeter is 0.04 [66].

Muon ID - The uncertainty on the muon ID efficiency for muons used in this analysis in run2a is ± 0.007 [60] and in run2b is ± 0.002 [61]. For the limit calculations, this analysis use the value of ± 0.007 for both run2a and run2b Monte Carlo events.

Muon tracking efficiency - The uncertainty on the muon tracking efficiency is 0.01 [61].

Production cross sections - Production cross section uncertainties are applied to the Monte Carlo samples as specified in Table 5.7. The signal production cross section uncertainty is shown as a band on the 95% Confidence Level exclusion plots.

QCD Estimation - The uncertainty on the QCD estimate is 29%. The details on how this value is derived are given in Section 4.7.

5.4.2 Shape Based Systematic Uncertainties

The shape based uncertainties are calculated for each bin for each Monte Carlo sample. The uncertainties are asymmetric, and, thus, there is a positive and a negative uncertainty histogram for each uncertainty listed. These uncertainties are correlated among the samples and Collie treats them as such.

Luminosity profiles re-weighting - The luminosity re-weighting is applied on an event-by-event basis, parameterized by the instantaneous luminosity. The uncertainty on the re-weighting is calculated simultaneously.

Trigger efficiency correction uncertainty - When the regression calculations are performed in order to determine the coefficients used in the trigger efficiency model, the coefficient covariance matrices are calculated as well. As indicated in Eq. 4.6, the uncertainty on the model is provided by the factor $e^{\pm\sqrt{\mathbf{X}^T\mathbf{V}\mathbf{X}}}$ which appears in both the numerator and the denominator. Due to this form, the uncertainty is inherently asymmetric and heteroskedastic. Since the trigger efficiency correction is actually calculated from a combination of two GLM's (see eqn. 4.18) the two uncertainties provided by

the GLM's are combined using standard propagation of errors and calculated on an event by event basis.

Jet Energy Scale Uncertainty To determine the effect of the jet energy scale on the Monte Carlo samples, the analysis variables were recalculated with the JES varied by plus and minus one sigma. The differences between the analysis variable distributions of the nominal and the samples with varied JES are included as shape dependent systematics.

Table 5.7 gives the fractional uncertainty of the correction as measured over all events.

	WW	WZ	ZZ	W	$t\bar{t}$	$Z \to ll$	QCD	(110,90)	(200,100)
Statistical	0.004	0.007	0.01	0.04	0.00	0.004	0.29	0.01	0.001
Cross Section	0.056	0.067	0.55	$^{+0.036}_{-0.032}$	$^{+0.075}_{-0.097}$	$^{+0.036}_{-0.032}$			
Trigger Efficiency	0.002	0.002	0.005	0.01	0.001	0.01		0.01	0.01
Lumi. reweighting	0.04	0.03	0.05	0.05	0.05	0.06		0.01	0.01
Jet Energy Scale	0.00	0.01	0.01	0.01	0.00	0.02		0.01	0.02
Luminosity	0.061	0.061	0.061	0.061	0.061	0.061		0.061	0.061
Electron ID	0.04	0.04	0.04	0.04	0.04	0.04		0.04	0.04
Muon ID	0.01	0.01	0.01	0.01	0.01	0.01		0.01	0.01
Muon Track ID	0.01	0.01	0.01	0.01	0.01	0.01		0.01	0.01

Table 5.7: Summary of the systematic uncertainties included in the limit calculations.

Chapter 6

Results and Conclusions

No significant excess above the standard model prediction was found. We have set 95% confidence level exclusion limits for light top squark pair production assuming a 100% branching fraction to $b\bar{b}l^{\pm}l^{\mp}\tilde{\nu}\bar{\tilde{\nu}}$ and used them to set limits in the sneutrino mass versus stop mass plane as shown in Figure 6.1. We have excluded stop pair production for $m_{\tilde{t}_1} < 220$ GeV when $m_{\tilde{\nu}} < 110$ GeV and the difference $m_{\tilde{t}_1} - m_{\tilde{\nu}} > 30$ GeV. Also shown are earlier results from DØ using the combined ee+$e\mu$ channels with a 1.1 fb^{-1} sample [1], and the results from LEP [79][80]. Figure 6.2 shows the 95% CL cross section as a fraction of theoretical cross section by top squark mass for both the expected and observed limits.

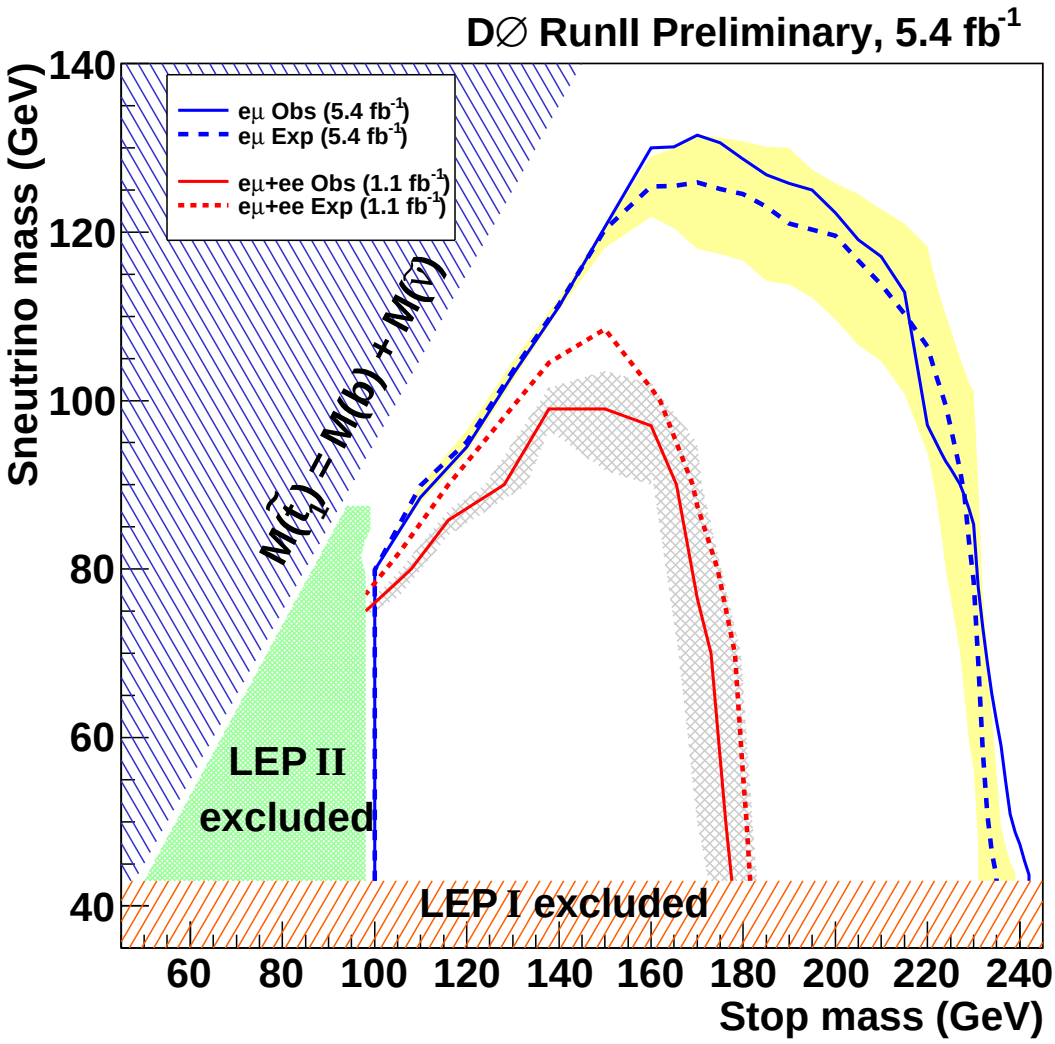

Figure 6.1: The DØ 5.4 fb^{-1}, preliminary observed (expected) 95% confidence exclusion region includes all mass points below the solid (dashed) blue line. The yellow area shows the effects of the stop quark cross section uncertainties. The shaded blue region is kinematically forbidden. The shaded orange and green areas were excluded by LEP I and LEP II respectively. Also shown is the DØ 1.1 fb^{-1} combined result from the $e\mu$ and ee channels [1].

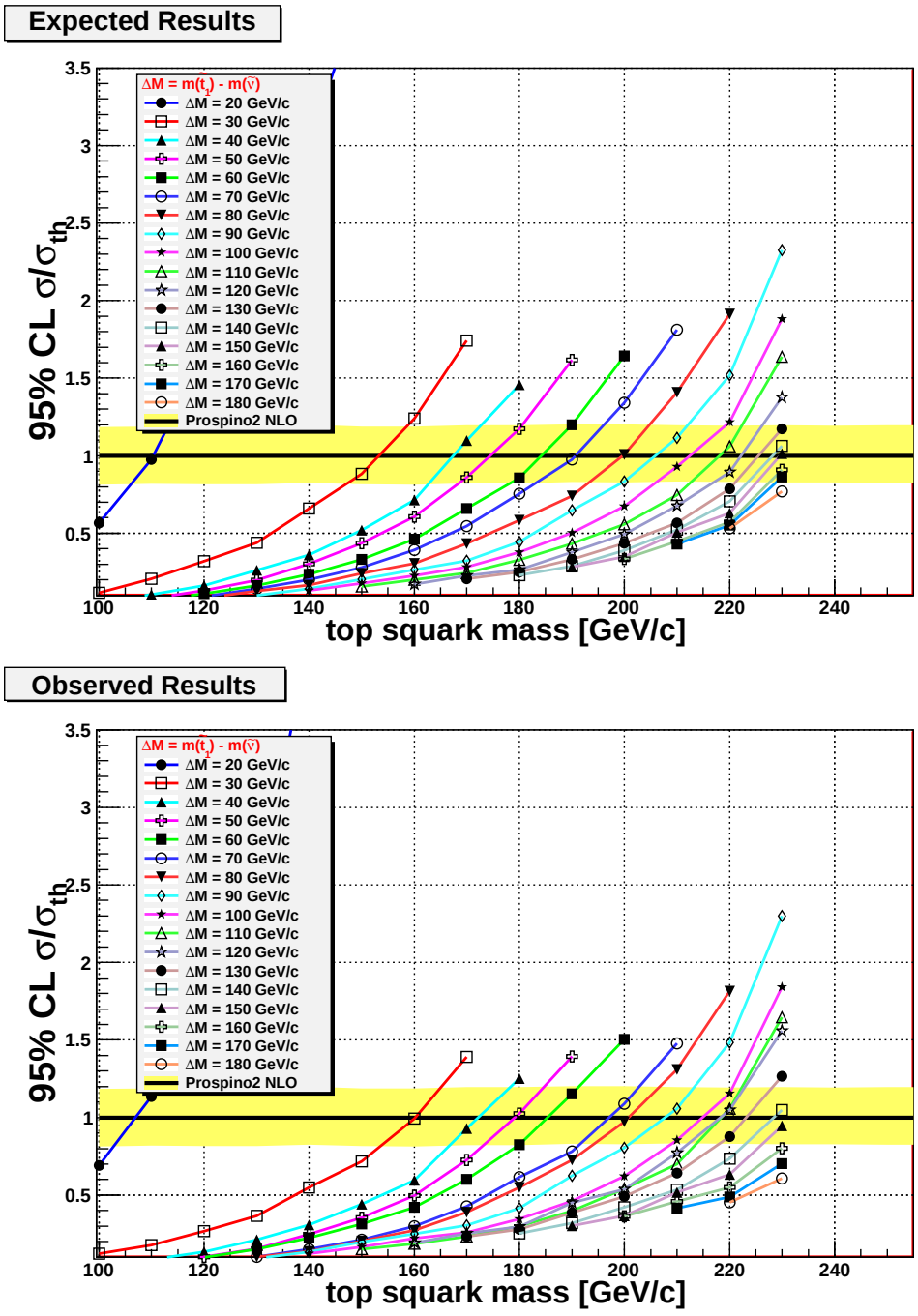

Figure 6.2: The 95% CL cross section as a fraction of the theoretical cross section by top squark mass for both the expected (top) and observed (bottom) limits.

Bibliography

[1] V. M. Abamov et al. Search for the lightest scalar top quark in events with two leptons in $p\bar{p}$ collisions at $\sqrt{s} = 1.96$ TeV. *Physics Letters B*, 675(3-4):289 – 296, 2009.

[2] David J. Gross and Frank Wilczek. Ultraviolet behavior of non-abelian gauge theories. *Phys. Rev. Lett.*, 30(26):1343–1346, Jun 1973.

[3] Donald H. Perkins. *Introduction to High Energy Physics*. Cambridge University Press, Cambridge, fourth edition, 2000.

[4] Francis Halzen and Alan D. Martin. *Quarks and Leptons: An Introductory Course in Modern Particle Physics*. John Wiley & Sons, Inc., Redwood City, California, first edition, 1984.

[5] David Griffiths. *Introduction to Elementary Particles*. John Wiley and Sons, Inc., 1987.

[6] K. Hagiwara et al. Review of Particle Physics. *Physical Review D*, 66:010001, 2002.

[7] Peter W. Higgs. Broken symmetries and the masses of gauge bosons. *Phys. Rev. Lett.*, 13(16):508–509, Oct 1964.

[8] F. Englert and R. Brout. Broken symmetry and the mass of gauge vector mesons. *Phys. Rev. Lett.*, 13(9):321–323, Aug 1964.

[9] G. S. Guralnik, C. R. Hagen, and T. W. B. Kibble. Global conservation laws and massless particles. *Phys. Rev. Lett.*, 13(20):585–587, Nov 1964.

[10] Laura Reina. TASI 2004 lecture notes on Higgs boson physics. 2005.

[11] Leonard Susskind. Dynamics of spontaneous symmetry breaking in the Weinberg-Salam theory. *Phys. Rev. D*, 20(10):2619–2625, Nov 1979.

[12] G. D'Agostini and G. Degrassi. Constraints on the Higgs boson mass from direct searches and precision measurements. *Eur. Phys. J.*, C10:663–675, 1999.

[13] Ian Aitchison. *Supersymmetry in Particle Physics: An Elementary Introduction*. Cambridge Univ. Press, Cambridge, 2007.

[14] Manuel Drees. An Introduction to Supersymmetry. *arXiv*, arXiv:hep-ph/9611409, 1996.

[15] Stephen P. Martin. A Supersymmetry Primer. arXiv:hep-ph/9709356v5, 2006.

[16] P. Fayet and S. Ferrara. Supersymmetry. *Physics Reports*, 32(5):249 – 334, 1977.

[17] Manuel Drees and Stephen P. Martin. Implications of susy model building. arXiv:hep-ph/9504324v1, 1995.

[18] H. E. Haber. Supersymmetry part I (theory). *Physics Letters B*, Review of Particle Physics:1003–1014, 2002.

[19] H. E. Haber and G. L. Kane. The search for supersymmetry: Probing physics beyond the Standard Model. *Phys. Rep.*, 117:75, 1985.

[20] C. Boehm, A. Djouandi, and Y. Mambrini. Decays of the lightest top squark. *Phys. Rev. D*, 61(095006):1–10, 1999.

[21] D0 Collaboration and V. M. Abazov. Search for scalar top quarks in the acoplanar charm jets and missing transverse energy final state in $p\bar{p}$ collisions at $\sqrt{s} = 1.96$ TeV. *Physics Letters B*, 665:1, 2008.

[22] Terry Asher. Main Injector Rookie Book. *Fermilab Operations Technical Note*, 2010.

[23] Brian Drendel, Jim Morgan, and Stan Johnson. Antiproton Source Rookie Book. *Fermilab Operations Technical Note*, 2009.

[24] S. Abachi et al. The DØ detector. *Nuclear Instruments & Methods in Physics Research*, A 338:185 – 253, 1994.

[25] V.M. Abazov et al. The upgraded DØ detector. *Nuclear Instruments & Methods in Physics Research*, 565(2):463 – 537, 2006.

[26] John Ellison. The DØ Upgrade and Physics Program. *DØ Internal Note*, (3830), 2001.

[27] Richard C. Fernow. *Introduction to experimental particle physics*. Cambridge University Press, Cambridge, first edition, 1986.

[28] Nikola Makovec and Jean-Francois Grivaz. Shifting, smearing, and removing simulated jets. *DØ Internal Note*, 4914(4914), 2005.

[29] Jan Stark. Undertanding and modeling the cal energy resolution. *W Mass Meeting, Jan. 13, 2006*.

[30] DØ JES Working Group. Jet Energy Scale Determination at DØ Run II (final p17 version). *DØ Internal Note*, 5382, 2007.

[31] DØ JES Working Group. Jet Energy Scale Determination at DØ Run II (final p20 version). *DØ Internal Note*, 5801, 2009.

[32] DØ Jet Energy Scale Working Group. See http://www-d0.fnal.gov/phys_id/jes/public/plots/.

[33] Yuri Fisyak and John Womersley. DØGSTAR DØ GEANT simulation of the total apparatus response. *DØ Internal Note*, 3191, 1997.

[34] Alexander Khanov. HTF: Histogramming method for finding tracks. the algorithm description. *DØ Internal Note*, 3778, 2000.

[35] R. Fruhwirth. Application of Kalman filtering to track and vertex fitting. *Nucl. Inst. and Methods*, A262(2-3):444 – 450, 1987.

[36] Guennadi Borissov. Technical Details of AA Tracking. See http://www-d0.fnal.gov/atwork/adm/d0_private/2003-02-28/adm_talk.ps. *All DØ Meeting, Feb. 28, 2003*, 2003.

[37] F. Flueret. The DØ Electron/Photon Analysis Package EMAnalyze. *DØ Internal Note*, 2001.

[38] E. Busato and B. Andrieu. Jet Algorithms in D0 RunII Software: Description and User's Guide. *DØ Internal Note*, 4457, 2004.

[39] Frederic Deliot. The fit algorithm in muo_trackreco. *DØ Internal Note*, 5879(5879), 2009.

[40] DØ Data Format Working Group. Recommendations Regarding Common Analysis Format Content. *DØ Internal Note*, 4647(4647), 2005.

[41] DØ Common Samples Group. See http://www-d0.fnal.gov/run2physics/cs/caf/.

[42] Abdelhak Djouadi, Jean-Loc Kneur, and Gilbert Moultaka. SuSpect: A Fortran code for the Supersymmetric and Higgs particle spectrum in the MSSM. *Computer Physics Communications*, 176(6):426 – 455, 2007.

[43] Peter Skands et al. Susy les houches accord: interfacing susy spectrum calculators, decay packages, and event generators. *Journal of High Energy Physics*, 2004(07):036, 2004.

[44] M. Muhlleitner. SDECAY - a Fortran code for SUSY particle decays in the MSSM. *ACTA PHYS.POLON.B*, 35:2753, 2004.

[45] Johan Alwall et al. MadGraph/MadEvent v4: The New Web Generation. *JHEP*, 09:028, 2007.

[46] Torbjorn Sjostrand, Stephen Mrenna, and Peter Skands. Pythia 6.4 physics and manual. *hep-ph*, (0603175), 2006.

[47] W. Beenakker, R. Höpker, and M. Spira. PROSPINO: a program for the production of supersymmetric particles in next-to-leading order QCD. arXiv:hep-ph/9611232v1, 1996.

[48] J. Pumplin, D. R. Stump, J. Huston, H. L. Lai, P. Nadolsky, and W. K. Tung. New generation of parton distributions with uncertainties from global QCD analysis. *JHEP0207*, 012, 2002.

[49] Michelangelo L. Mangano, Mauro Moretti, Fulvio Piccinini, Roberto Pittau, and Antonio D. Polosa. ALPGEN, a generator for hard multiparton processes in hadronic collisions. *JHEP*, 07:001, 2003.

[50] D. Gillberg. Heavy flavour removal and determination of weighting factors for ALPGEN W + jets Monte Carlo. *DØ Internal Note*, 5129, 2006.

[51] J. D. Hobbs, T. Nunnemann, and R. Van Kooten. Study of the $p\bar{p} \to z/\gamma^* \to e\bar{e}$ and $p\bar{p} \to z/\gamma^* \to \mu\bar{\mu}$ event yields as a luminosity cross check. *DØ Internal Note*, 5268(5268), 2006.

[52] J. F. Grivaz. DØ v+jets working group meeting - news 6/24/2008, http://www-d0.hef.kun.nl/fullagenda.php?ida=a081147. 2008.

[53] S. Moch and P. Uwer. Heavy-quark pair production at two loops in QCD. *Nuclear Physics B Proceeding Supplements*, 183:7580, 2008.

[54] DØ Electron ID Group. See http://www-d0.fnal.gov/phys_id/emid/d0_private/emid.html.

[55] Joseph Kozminski, Robert Kehoe, Harry Weerts, Su-Jung Park, Arnulf Quadt, John Gardner, and Shabnam Jabeen. Electron Likelihood in p14. *DØ Internal Note*, 4449, 2004.

[56] Ashish Kumar, Joseph Kozminski, Robert Kehoe, Jonathan Hays, and Jan Stark. Electron likelihood study. *DØ Internal Note*, 4769, 2005.

[57] Jonathan Hays, Jovan Mitrevski, Christian Schwanenberger, and Lei Wang. Electron Likelihood Effciency in p17. *DØ Internal Note*, 5114(5114), 2006.

[58] DØ Jet ID Group. See http://www-d0.fnal.gov/phys_id/jets/jetid.html.

[59] Amnon Harel and Robert Wagner. Improved L1 Confirmation. *DØ Internal Note*, 4432, 2005.

[60] Philippe Calfayan, Thomas Gadfort, Gavin Hesketh, Vincent Lesne, Mark Owen, Raimund Stroehmer, Viatcheslav Sharyy, and Boris Tuchming. Muon ID certification for p17 data. *DØ Internal Note*, 5157(5157), 2007.

[61] SungWoong Cho, Frederic Deliot, Mike Eads, Dave Hedin, HyeonSeung Lee, Boris Tuchming, and Yury Yatsunenko. Muon ID certification for p20 data. *DØ Internal Note*, 5824, 2008.

[62] Fabrice Couderc. See plone4.fnal.gov/p1/d0wiki/comp/caf/mcreweighting/lumiprofile-reweighting.

[63] Heidi Schellman. The longitudinal shape of the luminous region at DØ. *DØ Internal Note*, 5142, 2006.

[64] Gavin Hesketh. Generator level reweighting of the inclusive W boson p_t distribution. *DØ Internal Note*, 5786, 2008.

[65] Tim Bolton and Mansoora Shamim. Generator level reweighting of Z boson p_t. *DØ Internal Note*, 5565, 2008.

[66] Oleksiy Atramentov, Dmitry Bandurin, Xuebing Bu, Betty Calpas, Edgar Carrera, Daniel Duggan, Alexey Ferapontov, Maiko Takahashi, Tonya Uzbyakova, and Hang Yin. Electron and photon identifcation with p20 data. *DØ Internal Note*, 5761, 2008.

[67] Supriya Jain. Scale and over-smearing for MC electron. *DØ Internal Note*, 4402(4402), 2004.

[68] Marion Arthaud, Frederic Deliot, Boris Tuchming, Viatcheslav Sharyy, and Didier Vilanova. Muon momentum oversmearing for p17 data. *DØ Internal Note*, 5444(5444), 2007.

[69] Marion Arthaud, Frederic Deliot, Boris Tuchming, Viatcheslav Sharyy, and Didier Vilanova. Muon momentum oversmearing for p20 data. *DØ Internal Note*, 5449(5449), 2007.

[70] P. Mccullagh and J. Nelder. *Generalized Linear Models, Second Edition*. Chapman & Hall/CRC, August 1989.

[71] Julian J. Faraway. *Extending the Linear Model with R: Generalized Linear, Mixed Effects and Nonparametric Regression Models*. Texts in Statistical Science. Chapman & Hall/CRC, December 2005.

[72] W. N. Venables and B. D. Ripley. *Modern Applied Statistics with S*. Springer, New York, fourth edition, 2002.

[73] Raymond H. Myers, Douglas C. Montgomery, G. Geoffrey Vining, and Timothy J. Robinson. *Generalized Linear Models with Applications in Engineering and the Sciences*. John Wiley & Sons, Inc., Hoboken, New Jersey, second edition, 2010.

[74] R Development Core Team. *R: A Language and Environment for Statistical Computing*. R Foundation for Statistical Computing, Vienna, Austria, 2009.

[75] W. Fisher. Collie: A confidence level limit evaluator. *Fermilab-TM-2386-E*, 2007.

[76] Thomas Junk. Condfidence level computation for combining searches with small statistics. *Nuclear Instruments & Methods in Physics Research*, Section A(434):435–443, 1999.

[77] Brendan Casey, Yuji Enari, Thorsten Kuhl, Thomas Nunnemann, Rich Patridge, Pavel Polozov, Heidi Schellman, and Markus Wobisch. Determination of the effective inelastic

$p\bar{p}$ cross-section for the DØ luminosity measurement using upgraded readout electronics. *DØ Internal Note*, 4958(4958), 2005.

[78] Brendan Casey, Marj Corcoran, Yuji Enari, Michelle Prewitt, and Greg Snow. Determination of the RunIIb Luminosity Constants. *DØ Internal Note*, 5559(5559), 2008.

[79] C. Amsler et al. *Phys. Lett.*, B667:1, 2008.

[80] LEP SUSY Working Group. Report no. lepsusywg/01-02.1. LEPSUSYWG/01-02.1, 2001.

Appendix A

Optimizing the Coefficients of a Generalized Linear Model with a Logistic Link Function

The coefficient vectors $\boldsymbol{\beta}$ of linear models with the form

$$Y = \beta_0 + \sum_{i=1}^{p} \beta_i x_i + \varepsilon \tag{A.1}$$

are optimized using ordinary least squares (OLS)[1]. Here p is the number of explanatory variables and Y is the response. OLS determines the coefficients values which minimize $S(\boldsymbol{\beta})$ for the equation

$$S(\boldsymbol{\beta}) = \sum_{j=1}^{n} [y_j - \beta_0 + \sum_{i=1}^{p} \beta_i x_i] \tag{A.2}$$

[1]For a concise and clear introduction to OLS see [73].

where n is the number of data points and y_j the response for data point j. The logistic Generalized Linear Model has the form

$$\text{logit}(\mu) = \log\frac{\mu}{1-\mu} = \beta_0 + \sum_{\text{i=1}}^{\text{p}} \beta_{\text{i}} \text{x}_{\text{i}}. \tag{A.3}$$

In this case, OLS cannot be used because there are no measured values of the response, y_j, on which to base the model. Also, the response uncertainty is binomial rather than Gaussian and must be treated accordingly. Instead of OLS, iteratively reweighted least squares (IRWLS) is used[2]. In this section we outline the algorithm for IRWLS in order to answer the question "How are the GLM coefficients determined?".

We begin our discussion of IRWLS with a definition of terms. Let

$$Y = \log\frac{\mu}{1-\mu}. \tag{A.4}$$

Then

$$\frac{\partial Y}{\partial \mu} = \frac{1}{\mu(1-\mu)}. \tag{A.5}$$

Initially, the value for the estimated value of the probability, $\hat{\mu}_0$, can be set to the ratio of "successes" to total sample size. We use this value of $\hat{\mu}_0$ to get $Y_0 = \log\frac{\hat{\mu}_0}{1-\hat{\mu}_0}$. Next, for each data point, j, in the training sample we calculate the response z_j:

$$z_j = \hat{Y}_0 + (c_j - \hat{\mu_0})\frac{1}{\hat{\mu}_0(1-\hat{\mu}_0)} \tag{A.6}$$

[2]The explanation of IRWLS given here is based on that of Faraway, Chapter 6 [71].

where c_j is 1 if event j is a "success" and 0 otherwise. We can now use least squares regression with the z_j in place of the measured values y_j to determine the coefficients, $\boldsymbol{\beta}$, which minimize

$$S(\boldsymbol{\beta}) = \sum_{j=1}^{n} w_j[z_j - \beta_0 + \sum_{i=1}^{p} \beta_i x_{ij}]. \tag{A.7}$$

Instead of OLS, we use weighted least squares where the events are weighted by the inverse of the variance of z_j, $w_j = n\hat{\mu}(1-\hat{\mu})$. Weighting makes events with less uncertainty have a greater influence on the coefficient values. For each data point j we calculate $\hat{Y}_j$ and $\hat{\mu}_j$ using eq. A.3 and eq. A.4 with the newly calculated $\boldsymbol{\beta}$. Next, we recalculate z_j for each data point j:

$$z_j = \hat{Y}_j + (y_j - \hat{\mu}_j)\frac{1}{\hat{\mu}_j(1-\hat{\mu}_j)}. \tag{A.8}$$

and again use regression to calculate $\boldsymbol{\beta}$ for eq. A.7. We compare the new set of coefficients to the old ones. Until the coefficient values have converged to the desired degree of precision, we continue with the iterative process [71].

Appendix B

Interpreting the Coefficients of a Generalized Linear Model with a Logistic Link Function

In this analysis we use Generalized Linear Models (GLM) in Section 4.6 to estimate the trigger efficiency and in Section 5.2 to create variables which discriminate between the signal and one of the backgrounds. In our presentation of the models, the coefficients have the inverse dimensions of their associated variables. Thus, most of the coefficients have different dimensions and cannot be easily compared to one another. An alternative method for presenting the coefficients is to "normalize" the variable values before putting them into the GLM. By "normalize" we mean subtract the mean and divide by the standard deviation[1]. In this section, we show that using normalized variables makes interpretations of and comparisons between the coefficients much simpler. First, using an argument based on that given in Myers Chapter 4 [73], we show that a one standard deviation change in

[1]This "normalization trick" was suggested and explained by David Scott through private discussions.

the value of an explanatory variable, which we call x_j, scales the odds of success by a factor of e^{β_j} where β_j is the coefficient associated with variable x_j. Next, we give the coefficients from Section 5.2, but re-derived from normalized data. These coefficients clearly give more insight into the relative power of the variables.

In order to interpret the coefficients of the logistic GLM,

$$\log \frac{\mu}{1-\mu} = \beta_0 + \sum_{i=1}^{p} \beta_i x_i, \tag{B.1}$$

is usefully to note that the left hand side of the equation is the log of the odds of successes to failures. Since it is a function of the vector $\mathbf{x}$, we denote it as $Y(\mathbf{x})$. We let $\mathbf{x}$ be the values associated with a single binomial trial and let $\mathbf{x}'$ be an equivalent vector but with the value of one variable, which we label with subscript j, shifted by one standard deviation. Then

$$Y(\mathbf{x}') - Y(\mathbf{x}) = [\beta_0 + \beta_j(x_j + 1) + \sum_{i=1,\ i\neq j}^{p} \beta_i x_i] - [\beta_0 + \beta_j(x_j) + \sum_{i=1,\ i\neq j}^{p} \beta_i x_i]. \tag{B.2}$$

Which simplifies to

$$Y(\mathbf{x}') - Y(\mathbf{x}) = \beta_j. \tag{B.3}$$

Since Y is the log odds, we write

$$\log\left[\text{odds}(\mathbf{x}')\right] - \log\left[\text{odds}(\mathbf{x})\right] = \log \frac{\text{odds}(\mathbf{x}')}{\text{odds}(\mathbf{x})} = \beta_j. \tag{B.4}$$

Thus,

$$e^{\beta_j} = \frac{\text{odds}(\mathbf{x}')}{\text{odds}(\mathbf{x})}. \tag{B.5}$$

In addition to showing that changing a single variable value by a single standard deviation changes the odds of a success by a factor of e^{β_j}, eqn. B.5 shows that the magnitude of the coefficients is directly related to the magnitude of their contribution to the model. This feature of the coefficients makes it possible to directly compare the classification power of the coefficients for normalized variables. To enable this comparison for the discriminant variables described in Section 5.2, we recomputed the coefficients using normalized variables. It should be noted that normalizing the variables will not change the predictions or the uncertainty of the GLM. The coefficients associated with the normalized variables are given for the discriminant variables δZ, δWW, and $\delta t\bar{t}$ are given in Tables B.1, B.2, and B.3 respectively. Table B.1 shows that for δZ the transverse momentum variables become more predictive as ΔM gets larger. The opening angles between the $\not\!\!E_T$ and the charged leptons is predictive for all ΔM values. It is not surprising that the opening angle between the two charged leptons is the least predictive variable since Cut 1, requiring that $\not\!\!E_T > 20$ GeV or $\Delta\phi(e,\mu) < 2.8$ has already been applied. Table B.2 shows that for δWW all variables change as ΔM increases but no variables have a coefficient greater than one except for $\Delta M < 30$ GeV/c^2 and $\Delta M = 140$ GeV/c^2. Table B.3 shows that for $\delta t\bar{t}$ the lepton p_T coefficients change signs from negative to positive as the value of ΔM gets bigger. Their power relative to the other variables peaks at large, corresponding to "hard', and small, corresponding to "soft", ΔM values.

ΔM GeV/c^2	intercept	$\log p_T(e)$	$\log p_T(\mu)$	$\log \not\!\!E_T$	$\Delta\phi(e,\mu)$	$\Delta\phi(e,\not\!\!E_T)$	$\Delta\phi(\mu,\not\!\!E_T)$	$\Delta\phi(e,\not\!\!E_T)\times$ $\Delta\phi(\mu,\not\!\!E_T)$
20	0.59	-0.54	-0.46	0.62	-0.36	1.69	1.75	1.88
30	1.01	0.13	0.05	0.70	-0.68	1.50	1.60	2.28
40	1.31	0.44	0.47	0.82	-0.63	1.52	1.59	2.55
50	1.42	0.93	0.72	1.08	-0.29	1.10	1.31	3.02
60	1.51	1.27	1.17	1.35	-0.19	1.34	1.36	2.65
70	1.74	1.56	1.35	1.50	-0.28	1.26	1.38	2.70
80	2.03	1.78	1.60	1.84	-0.44	1.67	1.73	2.29
90	2.20	2.01	1.88	2.10	-0.17	1.40	1.34	2.70
100	2.10	2.18	2.29	1.82	-0.54	1.59	1.47	1.73
140	2.80	2.95	3.03	2.38	-0.07	1.13	1.09	2.33

Table B.1: The values of the coefficient vector $\boldsymbol{\beta}$ derived for discriminant variable δZ after normalizing the training sample.

ΔM GeV/c^2	intercept	numJets	$\log p_T(e)$	$\log p_T(\mu)$	$\log \not\!\!E_T$	$\Delta\phi(e,\mu)$	logWWtag
20	-0.81	0.36	-1.88	-2.12	-0.67	2.04	0.30
30	-0.13	0.33	-1.11	-1.23	-0.52	0.90	0.46
40	-0.01	0.26	-0.66	-0.79	-0.12	0.57	0.53
50	0.03	0.42	-0.33	-0.37	0.05	0.28	0.62
60	0.04	0.51	-0.01	-0.08	0.16	0.12	0.67
70	0.05	0.60	0.20	0.15	0.30	0.00	0.70
80	0.04	0.63	0.43	0.36	0.41	-0.12	0.75
90	0.04	0.78	0.60	0.52	0.54	-0.19	0.79
100	0.04	0.76	0.73	0.66	0.61	-0.24	0.90
140	0.00	0.96	1.24	1.13	0.82	-0.43	1.02

Table B.2: The values of the coefficient vector $\boldsymbol{\beta}$ derived for discriminant variable δWW after normalizing the training sample.

ΔM GeV/c^2	intercept	$\log(1+H_T)$	$\log p_T(e)$	$\log p_T(\mu)$	$\log \not\!\!E_T$	$(numJets>1)$ $*jet2Pt$	WWtag
20	0.75	-0.95	-2.07	-2.06	-1.07	-2.15	-0.64
30	0.89	-1.13	-1.15	-1.15	-0.88	-1.69	-1.01
40	0.70	-1.14	-0.91	-0.82	-0.54	-1.53	-1.50
50	0.73	-0.86	-0.54	-0.50	-0.33	-1.65	-1.59
60	0.64	-0.82	-0.27	-0.24	-0.17	-1.44	-1.62
70	0.68	-0.79	-0.10	-0.10	0.02	-1.42	-1.69
80	0.71	-0.71	0.03	0.07	0.19	-1.37	-1.32
90	0.70	-0.64	0.19	0.18	0.27	-1.30	-1.17
100	0.74	-0.41	0.38	0.28	0.35	-1.42	-1.93
140	0.70	-0.28	0.82	0.72	0.64	-1.16	-0.61

Table B.3: The values of the coefficient vector $\boldsymbol{\beta}$ derived for discriminant variable $\delta t\bar{t}$ after normalizing the training sample.

Appendix C

Signal Monte Carlo Sample Details

$m(st_1)$ GeV/c^2	$m(\tilde{\nu})$ GeV/c^2	$m(\chi_1^+)$ GeV/c^2	$\Gamma(\chi_1^+)$ GeV/c^2	$m(\chi_2^+)$ GeV/c^2	$\Gamma(\chi_2^+)$ GeV/c^2	$m(L_1)$ GeV/c^2	A_t GeV/c^2	μ	$\sigma \times br$	run2b events	run2a events
100	40	146.3	1.1	412.4	21.4	75.7	438.5	153.9	3.36	26162	19483
110	40	149.1	0.9	412.5	21.3	75.7	430	157	1.97	26014	19207
120	40	152.4	0.7	412.6	21.1	75.7	420.4	160.6	1.21	26407	19426
130	40	156.2	0.6	412.7	21	75.7	409.8	164.7	0.77	25992	19340
140	40	160.7	0.5	412.9	20.9	75.7	398.1	169.6	0.5	25811	19290
150	40	165.9	0.4	413.1	20.8	75.7	385.2	175.2	0.34	26259	19730
160	40	172	0.4	413.4	20.6	75.7	371.1	181.9	0.23	26152	19411
170	40	179.1	0.4	413.8	20.5	75.7	355.9	189.7	0.16	26556	19185
180	40	187.5	0.4	414.3	20.3	75.7	339.5	198.8	0.11	25312	19110
190	40	197.3	0.5	415	20.1	75.7	321.8	209.7	0.08	26595	19534
200	40	208.9	0.6	415.9	19.8	75.7	303	222.8	0.06	26577	19281
210	40	222.8	0.7	417.2	19.5	75.7	282.9	238.6	0.04	25805	19221
220	40	239.3	1	419	19	75.7	261.8	257.9	0.03	25965	19453
230	40	259.1	1.4	422	18.3	75.7	239.4	281.9	0.02	17564	19477
240	40	283.1	2.2	427.3	17.3	75.7	216	312.5	0.02	17924	19201
250	40	371.1	7.8	492.6	19.5	75.7	193.2	349.4	0.01	17577	18663
100	50	146.3	1	412.3	21.3	81.5	438.5	153.9	3.36	26991	18977
110	50	149.1	0.8	412.4	21.1	81.5	430	157	1.97	25598	18662
120	50	152.4	0.7	412.5	21	81.5	420.4	160.6	1.21	26438	19280
130	50	156.2	0.5	412.7	20.9	81.5	409.8	164.7	0.77	25766	19410
140	50	160.7	0.5	412.8	20.8	81.5	398.1	169.6	0.5	26629	19625
150	50	165.9	0.4	413.1	20.7	81.5	385.2	175.2	0.34	25565	19273
160	50	172	0.4	413.4	20.5	81.5	371.2	181.9	0.23	27283	19318
170	50	179.1	0.4	413.8	20.4	81.5	355.9	189.7	0.16	26080	18967
180	50	187.5	0.4	414.3	20.2	81.5	339.5	198.8	0.11	26474	19599
190	50	197.3	0.5	414.9	20	81.5	321.8	209.7	0.08	26027	19793
200	50	208.9	0.5	415.8	19.7	81.5	303	222.8	0.06	26550	19643
210	50	222.8	0.7	417.1	19.4	81.5	282.9	238.6	0.04	26014	19315
220	50	239.3	0.9	419	18.9	81.5	261.7	257.9	0.03	26007	19718
230	50	259.1	1.3	421.9	18.2	81.5	239.4	281.9	0.02	18777	19352
240	50	338.4	4.6	477.9	21.7	81.5	218.1	309.4	0.02	18618	9859
250	50	371.2	7.8	492.6	19.4	81.5	193.2	349.5	0.01	18491	19324
100	60	146.3	1	412.3	21.1	88	438.5	153.9	3.36	17073	19383
110	60	149.1	0.8	412.4	21	88	430	157	1.97	26125	19277
120	60	152.4	0.6	412.5	20.9	88	420.4	160.6	1.21	25977	19074
130	60	156.2	0.5	412.6	20.8	88	409.8	164.7	0.77	25167	19358
140	60	160.7	0.4	412.8	20.7	88	398.1	169.6	0.5	26724	19412
150	60	165.9	0.4	413	20.5	88	385.2	175.2	0.34	26704	19378
160	60	172	0.4	413.3	20.4	88	371.2	181.9	0.23	26126	19192
170	60	179.1	0.4	413.7	20.2	88	355.9	189.6	0.16	25883	19112
180	60	187.5	0.4	414.2	20.1	88	339.5	198.8	0.11	27133	19686
190	60	197.3	0.4	414.9	19.9	88	321.8	209.7	0.08	25616	19610
200	60	208.9	0.5	415.8	19.6	88	303	222.8	0.06	25974	19172
210	60	222.8	0.6	417.1	19.3	88	282.9	238.6	0.04	26157	19054
220	60	239.3	0.9	418.9	18.8	88	261.7	257.9	0.03	26384	19411
230	60	259.1	1.3	421.9	18.1	88	239.4	281.9	0.02	17179	19118
240	60	338.4	4.5	477.9	21.6	88	218.1	309.5	0.02	18980	18971
250	60	371.2	7.8	492.6	19.4	88	193.1	349.5	0.01	17746	19320

Table C.1: Listing part 1 of the top squark mass, sneutrino mass points with corresponding first and second chargino masses and widths. The top quark sector trilinear coupling constant A_t and the Higgs mass parameter μ values shown are the values used as inputs into SuSpect2. The final number of events for both the run2b and run2a Monte Carlo are listed as well.

$m(st_1)$ GeV/c^2	$m(\tilde{\nu})$ GeV/c^2	$m(\chi_1^+)$ GeV/c^2	$\Gamma(\chi_1^+)$ GeV/c^2	$m(\chi_2^+)$ GeV/c^2	$\Gamma(\chi_2^+)$ GeV/c^2	$m(L_1)$ GeV/c^2	A_t GeV/c^2	μ	$\sigma \times br$	run2b events	run2a events
100	70	146.3	1	412.2	21	95.1	438.5	153.9	3.36	25670	19433
110	70	149.1	0.8	412.3	20.9	95.1	430	157	1.97	24878	19333
120	70	152.4	0.6	412.4	20.8	95.1	420.4	160.6	1.21	25955	19235
130	70	156.2	0.5	412.6	20.6	95.1	409.8	164.7	0.77	25657	19277
140	70	160.7	0.4	412.8	20.5	95.1	398.1	169.6	0.5	26547	19222
150	70	165.9	0.3	413	20.4	95.1	385.2	175.2	0.34	25238	19156
160	70	172	0.3	413.3	20.2	95.1	371.2	181.9	0.23	26748	19452
170	70	179.1	0.3	413.7	20.1	95.1	355.9	189.6	0.16	25668	18879
180	70	187.5	0.4	414.2	19.9	95.1	339.5	198.8	0.11	26554	18984
190	70	197.3	0.4	414.8	19.7	95.1	321.8	209.7	0.08	26142	18955
200	70	208.9	0.5	415.7	19.4	95.1	303	222.8	0.06	26009	19473
210	70	222.8	0.6	417	19.1	95.1	282.9	238.6	0.04	26290	18975
220	70	239.3	0.8	418.9	18.6	95.1	261.7	257.9	0.03	26727	19396
230	70	259.1	1.2	421.8	18	95.1	239.4	281.9	0.02	17967	18942
240	70	338.5	4.5	477.8	21.5	95.1	218.1	309.5	0.02	19313	19312
250	70	371.2	7.7	492.5	19.3	95.1	193.1	349.5	0.01	17992	18770
100	80	146.3	1	412.2	20.8	102.6	438.5	153.9	3.36	27797	19089
110	80	149.1	0.8	412.3	20.7	102.6	430	157	1.97	25518	18978
120	80	152.4	0.6	412.4	20.6	102.6	420.4	160.6	1.21	26539	19564
130	80	156.2	0.5	412.5	20.5	102.6	409.8	164.7	0.77	26782	19115
140	80	160.7	0.4	412.7	20.3	102.6	398.1	169.6	0.5	25312	19503
150	80	165.9	0.3	412.9	20.2	102.6	385.2	175.2	0.34	25927	19235
160	80	172	0.3	413.2	20.1	102.6	371.1	181.9	0.23	25972	18831
170	80	179.1	0.3	413.6	19.9	102.6	355.9	189.7	0.16	26518	19517
180	80	187.5	0.3	414.1	19.7	102.6	339.5	198.8	0.11	25947	19007
190	80	197.3	0.4	414.8	19.5	102.6	321.8	209.8	0.08	26034	19394
200	80	208.9	0.4	415.7	19.3	102.6	303	222.8	0.06	26773	19250
210	80	222.8	0.6	417	18.9	102.6	282.9	238.6	0.04	25867	19601
220	80	239.3	0.8	418.8	18.5	102.6	261.7	257.9	0.03	25861	19711
230	80	259.1	1.2	421.8	17.8	102.6	239.4	282	0.02	17538	18921
240	80	338.5	4.4	477.8	21.3	102.6	218.1	309.5	0.02	17608	18846
250	80	371.2	7.6	492.5	19.1	102.6	193.1	349.5	0.01	17705	18744
110	90	149.1	0.7	412.2	20.5	110.6	430	157	1.97	25952	19094
120	90	152.4	0.6	412.3	20.4	110.6	420.4	160.6	1.21	26461	19566
130	90	156.2	0.4	412.5	20.3	110.6	409.8	164.7	0.77	26615	19165
140	90	160.7	0.3	412.7	20.1	110.6	398.1	169.6	0.5	26513	19350
150	90	165.9	0.3	412.9	20	110.6	385.2	175.2	0.34	26779	19438
160	90	172	0.3	413.2	19.9	110.6	371.1	181.9	0.23	26781	19057
170	90	179.1	0.3	413.6	19.7	110.6	355.9	189.7	0.16	26272	19352
180	90	187.5	0.3	414.1	19.6	110.6	339.4	198.9	0.11	26842	19357
190	90	197.3	0.3	414.7	19.3	110.6	321.8	209.8	0.08	26290	18948
200	90	209	0.4	415.6	19.1	110.6	302.9	222.8	0.06	26007	19365
210	90	222.8	0.5	416.9	18.8	110.6	282.9	238.6	0.04	25748	19573
220	90	239.3	0.7	418.8	18.3	110.6	261.7	257.9	0.03	26079	19139
230	90	259.1	1.1	421.7	17.6	110.6	239.4	282	0.02	17469	19583
240	90	338.5	4.3	477.7	21.2	110.6	218.1	309.5	0.02	17380	19297
250	90	371.2	7.5	492.5	19	110.6	193.1	349.5	0.01	18229	19508

Table C.2: Listing part 2 of the top squark mass, sneutrino mass points with corresponding first and second chargino masses and widths. The top quark sector trilinear coupling constant A_t and the Higgs mass parameter μ values shown are the values used as inputs into SuSpect2. The final number of events for both the run2b and run2a Monte Carlo are listed as well.

$m(st_1)$ GeV/c^2	$m(\tilde{\nu})$ GeV/c^2	$m(\chi_1^+)$ GeV/c^2	$\Gamma(\chi_1^+)$ GeV/c^2	$m(\chi_2^+)$ GeV/c^2	$\Gamma(\chi_2^+)$ GeV/c^2	$m(L_1)$ GeV/c^2	A_t GeV/c^2	μ	$\sigma \times br$	run2b events	run2a events
120	100	152.4	0.5	412.3	20.2	118.9	420.4	160.6	1.21	26431	19664
130	100	156.2	0.4	412.4	20.1	118.9	409.8	164.7	0.77	25711	19426
140	100	160.7	0.3	412.6	19.9	118.9	398	169.6	0.5	25682	19428
150	100	165.9	0.3	412.8	19.8	118.9	385.2	175.2	0.34	26640	19074
160	100	172	0.2	413.1	19.7	118.9	371.1	181.9	0.23	25758	19331
170	100	179.1	0.2	413.5	19.5	118.9	355.9	189.7	0.16	26190	19215
180	100	187.5	0.2	414	19.3	118.9	339.4	198.9	0.11	26150	19297
190	100	197.3	0.3	414.7	19.1	118.9	321.8	209.8	0.08	26307	19282
200	100	209	0.4	415.6	18.9	118.9	302.9	222.8	0.06	27162	19254
210	100	222.8	0.5	416.9	18.6	118.9	282.9	238.6	0.04	25743	19181
220	100	239.3	0.7	418.7	18.1	118.9	261.7	257.9	0.03	25644	18931
230	100	259.2	1.1	421.7	17.4	118.9	239.4	282	0.02	17715	19605
240	100	338.5	4.2	477.7	21	118.9	218.1	309.5	0.02	18214	19310
250	100	371.2	7.4	492.5	18.9	118.9	193.1	349.6	0.01	18168	19679
130	110	156.3	0.4	412.4	19.8	127.4	409.7	164.7	0.77	25812	19377
140	110	160.7	0.3	412.6	19.7	127.4	398	169.6	0.5	26535	19356
150	110	166	0.2	412.8	19.6	127.4	385.1	175.3	0.34	26237	19084
160	110	172	0.2	413.1	19.4	127.4	371.1	181.9	0.23	25988	19637
170	110	179.2	0.2	413.5	19.3	127.4	355.8	189.7	0.16	26798	19477
180	110	187.5	0.2	414	19.1	127.4	339.4	198.9	0.11	24685	19221
190	110	197.3	0.3	414.6	18.9	127.4	321.8	209.8	0.08	25910	19988
200	110	209	0.3	415.5	18.7	127.4	302.9	222.8	0.06	26041	19439
210	110	222.8	0.4	416.8	18.3	127.4	282.9	238.6	0.04	26834	19517
220	110	239.3	0.6	418.7	17.9	127.4	261.7	257.9	0.03	26903	19217
230	110	259.2	1	421.7	17.2	127.4	239.4	282	0.02	18021	19450
240	110	338.5	4.1	477.7	20.8	127.4	218.1	309.5	0.02	17939	19254
250	110	371.2	7.3	492.4	18.7	127.4	193.1	349.6	0.01	17481	18741
140	120	160.7	0.3	412.5	19.4	136.2	398	169.6	0.5	25758	19160
150	120	166	0.2	412.8	19.3	136.2	385.1	175.3	0.34	25955	19480
160	120	172.1	0.2	413.1	19.2	136.2	371.1	181.9	0.23	25731	19246
170	120	179.2	0.2	413.4	19	136.2	355.8	189.7	0.16	25731	19616
180	120	187.5	0.2	413.9	18.9	136.2	339.4	198.9	0.11	26984	18771
190	120	197.4	0.2	414.6	18.7	136.2	321.7	209.8	0.08	26752	19203
200	120	209	0.3	415.5	18.4	136.2	302.9	222.9	0.06	26287	18918
210	120	222.8	0.4	416.8	18.1	136.2	282.9	238.6	0.04	26821	19273
220	120	239.4	0.6	418.7	17.6	136.2	261.7	258	0.03	26095	18961
230	120	259.2	0.9	421.6	17	136.2	239.3	282	0.02	18725	19241
240	120	338.5	4	477.6	20.6	136.2	218	309.6	0.02	17771	18906
250	120	371.3	7.1	492.4	18.6	136.2	193.1	349.6	0.01	17110	19525
150	130	166	0.2	412.7	19	145	385.1	175.3	0.34	24977	19097
160	130	172.1	0.1	413	18.9	145	371	181.9	0.23	27526	19141
170	130	179.2	0.1	413.4	18.8	145	355.8	189.7	0.16	24970	19681
180	130	187.5	0.1	413.9	18.6	145	339.3	198.9	0.11	25648	19311
190	130	197.4	0.2	414.6	18.4	145	321.7	209.8	0.08	26153	19326
200	130	209	0.2	415.5	18.1	145	302.9	222.9	0.06	26311	18851
210	130	222.9	0.4	416.8	17.8	145	282.8	238.7	0.04	25966	19209
220	130	239.4	0.5	418.6	17.4	145	261.6	258	0.03	25711	19475
230	130	259.2	0.9	421.6	16.7	145	239.3	282	0.02	18081	19703
240	130	338.6	4	477.6	20.4	145	218	309.6	0.02	18033	19142
250	130	371.3	7	492.4	18.4	145	193	349.7	0.01	17822	19537
160	140	172.1	0.1	413	18.6	154.1	371	182	0.23	25684	17497
170	140	179.2	0.1	413.4	18.5	154.1	355.7	189.7	0.16	26259	19191
180	140	187.6	0.1	413.9	18.3	154.1	339.3	198.9	0.11	25348	19647
190	140	197.4	0.1	414.5	18.1	154.1	321.7	209.8	0.08	26887	19104
200	140	209	0.2	415.5	17.9	154.1	302.8	222.9	0.06	27179	18625
210	140	222.9	0.3	416.7	17.5	154.1	282.8	238.7	0.04	26654	19421
220	140	239.4	0.5	418.6	17.1	154.1	261.6	258	0.03	25614	19281
230	140	259.2	0.8	421.6	16.5	154.1	239.3	282.1	0.02	18121	19625
240	140	338.6	3.9	477.6	20.2	154.1	218	309.7	0.02	18353	19022
250	140	371.3	6.9	492.4	18.2	154.1	193	349.8	0.01	17999	18956

Table C.3: Listing part 3of the top squark mass, sneutrino mass points with corresponding first and second chargino masses and widths. The top quark sector trilinear coupling constant A_t and the Higgs mass parameter μ values shown are the values used as inputs into SuSpect2. The final number of events for both the run2b and run2a Monte Carlo are listed as well.

$m(st_1)$	$m(\tilde{\nu})$	run2b		run2a	
GeV/c^2	GeV/c^2	gg	$q\bar{q}$	gg	$q\bar{q}$
100	40	6.19E-5	3.10E-5	4.61E-5	2.31E-5
100	50	6.20E-5	2.98E-5	4.36E-5	2.09E-5
100	60	5.41E-5	2.77E-5	6.14E-5	3.14E-5
100	70	4.39E-5	2.32E-5	3.32E-5	1.75E-5
100	80	2.25E-5	1.58E-5	1.54E-5	1.08E-5
110	40	6.94E-5	3.28E-5	5.13E-5	2.43E-5
110	50	7.04E-5	3.28E-5	5.13E-5	2.39E-5
110	60	6.49E-5	3.06E-5	4.79E-5	2.25E-5
110	70	5.87E-5	2.82E-5	4.56E-5	2.19E-5
110	80	4.83E-5	2.44E-5	3.59E-5	1.81E-5
110	90	2.43E-5	1.59E-5	1.79E-5	1.17E-5
120	40	7.53E-5	3.36E-5	5.54E-5	2.47E-5
120	50	7.49E-5	3.38E-5	5.46E-5	2.47E-5
120	60	7.25E-5	3.33E-5	5.32E-5	2.44E-5
120	70	6.92E-5	3.15E-5	5.13E-5	2.34E-5
120	80	6.34E-5	2.86E-5	4.67E-5	2.11E-5
120	90	5.03E-5	2.44E-5	3.72E-5	1.80E-5
120	100	2.53E-5	1.58E-5	1.88E-5	1.18E-5
130	40	8.17E-5	3.55E-5	6.08E-5	2.64E-5
130	50	8.00E-5	3.51E-5	6.02E-5	2.64E-5
130	60	7.67E-5	3.48E-5	5.90E-5	2.68E-5
130	70	7.61E-5	3.39E-5	5.71E-5	2.55E-5
130	80	7.42E-5	3.27E-5	5.29E-5	2.33E-5
130	90	6.73E-5	3.04E-5	4.84E-5	2.19E-5
130	100	5.46E-5	2.55E-5	4.12E-5	1.92E-5
130	110	2.82E-5	1.63E-5	2.12E-5	1.23E-5
140	40	8.57E-5	3.70E-5	6.41E-5	2.76E-5
140	50	8.39E-5	3.60E-5	6.18E-5	2.65E-5
140	60	8.32E-5	3.63E-5	6.04E-5	2.64E-5
140	70	8.30E-5	3.60E-5	6.01E-5	2.61E-5
140	80	8.05E-5	3.48E-5	6.20E-5	2.68E-5
140	90	7.81E-5	3.35E-5	5.70E-5	2.45E-5
140	100	7.13E-5	3.09E-5	5.39E-5	2.34E-5
140	110	5.88E-5	2.63E-5	4.29E-5	1.92E-5
140	120	3.04E-5	1.72E-5	2.26E-5	1.28E-5
150	40	8.87E-5	3.69E-5	6.66E-5	2.77E-5
150	50	9.01E-5	3.77E-5	6.79E-5	2.84E-5
150	60	9.09E-5	3.71E-5	6.59E-5	2.69E-5
150	70	9.07E-5	3.76E-5	6.88E-5	2.85E-5
150	80	9.25E-5	3.67E-5	6.87E-5	2.72E-5
150	90	8.78E-5	3.55E-5	6.37E-5	2.58E-5
150	100	8.43E-5	3.49E-5	6.04E-5	2.50E-5
150	110	7.84E-5	3.23E-5	5.71E-5	2.35E-5
150	120	6.47E-5	2.69E-5	4.86E-5	2.02E-5
150	130	3.29E-5	1.77E-5	2.51E-5	1.35E-5
160	40	9.66E-5	3.89E-5	7.17E-5	2.88E-5
160	50	9.70E-5	3.87E-5	6.87E-5	2.74E-5
160	60	9.59E-5	3.88E-5	7.04E-5	2.85E-5
160	70	9.70E-5	3.78E-5	7.05E-5	2.75E-5
160	80	9.69E-5	3.91E-5	7.03E-5	2.83E-5
160	90	9.68E-5	3.79E-5	6.89E-5	2.70E-5
160	100	9.13E-5	3.66E-5	6.85E-5	2.75E-5
160	110	8.77E-5	3.48E-5	6.63E-5	2.63E-5
160	120	8.27E-5	3.31E-5	6.18E-5	2.48E-5
160	130	6.89E-5	2.86E-5	4.79E-5	1.99E-5
160	140	3.94E-5	1.98E-5	2.68E-5	1.35E-5
170	40	1.03E-4	4.01E-5	7.46E-5	2.90E-5
170	50	1.01E-4	4.06E-5	7.35E-5	2.95E-5
170	60	1.02E-4	4.03E-5	7.50E-5	2.97E-5
170	70	1.03E-4	4.04E-5	7.56E-5	2.97E-5
170	80	1.06E-4	3.89E-5	7.83E-5	2.86E-5
170	90	9.96E-5	3.89E-5	7.33E-5	2.87E-5
170	100	9.58E-5	3.90E-5	7.03E-5	2.86E-5
170	110	9.47E-5	3.77E-5	6.88E-5	2.74E-5
170	120	8.86E-5	3.63E-5	6.75E-5	2.77E-5
170	130	8.42E-5	3.36E-5	6.63E-5	2.65E-5
170	140	7.34E-5	2.98E-5	5.36E-5	2.18E-5
180	40	1.09E-4	4.13E-5	8.21E-5	3.12E-5
180	50	1.06E-4	4.02E-5	7.82E-5	2.98E-5
180	60	1.03E-4	3.99E-5	7.49E-5	2.90E-5
180	70	1.06E-4	4.17E-5	7.57E-5	2.98E-5
180	80	1.08E-4	4.12E-5	7.91E-5	3.02E-5
180	90	1.03E-4	4.05E-5	7.40E-5	2.92E-5
180	100	1.05E-4	4.01E-5	7.74E-5	2.96E-5
180	110	1.01E-4	3.97E-5	7.88E-5	3.09E-5
180	120	1.05E-4	3.99E-5	7.27E-5	2.77E-5
180	130	9.57E-5	3.77E-5	7.21E-5	2.84E-5
180	140	8.88E-5	3.47E-5	6.88E-5	2.69E-5
190	40	1.19E-4	4.01E-5	8.73E-5	2.94E-5
190	50	1.14E-4	3.93E-5	8.66E-5	2.99E-5
190	60	1.18E-4	3.99E-5	9.05E-5	3.06E-5
190	70	1.21E-4	4.10E-5	8.76E-5	2.97E-5
190	80	1.16E-4	3.99E-5	8.63E-5	2.97E-5
190	90	1.20E-4	4.08E-5	8.64E-5	2.94E-5
190	100	1.16E-4	3.99E-5	8.51E-5	2.93E-5
190	110	1.15E-4	4.04E-5	8.43E-5	2.96E-5
190	120	1.14E-4	3.94E-5	8.20E-5	2.83E-5
190	130	1.13E-4	3.83E-5	8.37E-5	2.83E-5
190	140	1.08E-4	3.79E-5	7.68E-5	2.70E-5
200	40	1.21E-4	4.10E-5	8.75E-5	2.97E-5
200	50	1.13E-4	4.08E-5	8.36E-5	3.02E-5
200	60	1.21E-4	4.13E-5	8.91E-5	3.05E-5
200	70	1.15E-4	4.07E-5	8.63E-5	3.05E-5
200	80	1.15E-4	4.12E-5	8.29E-5	2.96E-5
200	90	1.17E-4	4.10E-5	8.72E-5	3.05E-5
200	100	1.16E-4	4.09E-5	8.25E-5	2.90E-5
200	110	1.12E-4	4.02E-5	8.35E-5	3.00E-5
200	120	1.21E-4	4.10E-5	8.68E-5	2.95E-5
200	130	1.15E-4	4.09E-5	8.21E-5	2.93E-5
200	140	1.15E-4	4.05E-5	7.89E-5	2.78E-5
210	40	1.38E-4	4.18E-5	1.03E-4	3.11E-5
210	50	1.43E-4	4.15E-5	1.06E-4	3.08E-5
210	60	1.44E-4	4.23E-5	1.05E-4	3.08E-5
210	70	1.37E-4	4.26E-5	9.87E-5	3.07E-5
210	80	1.35E-4	4.10E-5	1.03E-4	3.10E-5
210	90	1.35E-4	4.10E-5	1.03E-4	3.12E-5
210	100	1.37E-4	4.18E-5	1.02E-4	3.12E-5
210	110	1.36E-4	4.08E-5	9.90E-5	2.97E-5
210	120	1.35E-4	4.13E-5	9.68E-5	2.97E-5
210	130	1.36E-4	4.10E-5	1.01E-4	3.03E-5
210	140	1.34E-4	3.99E-5	9.77E-5	2.90E-5
220	40	1.25E-4	4.32E-5	9.40E-5	3.24E-5
220	50	1.24E-4	4.26E-5	9.39E-5	3.23E-5
220	60	1.27E-4	4.29E-5	9.35E-5	3.16E-5
220	70	1.29E-4	4.31E-5	9.40E-5	3.13E-5
220	80	1.26E-4	4.26E-5	9.57E-5	3.24E-5
220	90	1.31E-4	4.36E-5	9.58E-5	3.20E-5
220	100	1.29E-4	4.40E-5	9.54E-5	3.25E-5
220	110	1.27E-4	4.34E-5	9.04E-5	3.10E-5
220	120	1.30E-4	4.37E-5	9.44E-5	3.17E-5
220	130	1.32E-4	4.22E-5	9.97E-5	3.20E-5
220	140	1.25E-4	4.24E-5	9.40E-5	3.19E-5
230	40	1.34E-4	4.09E-5	1.48E-4	4.53E-5
230	50	1.37E-4	4.06E-5	1.42E-4	4.18E-5
230	60	1.39E-4	4.12E-5	1.55E-4	4.58E-5
230	70	1.32E-4	4.19E-5	1.39E-4	4.42E-5
230	80	1.28E-4	4.19E-5	1.38E-4	4.52E-5
230	90	1.30E-4	3.99E-5	1.45E-4	4.47E-5
230	100	1.30E-4	4.03E-5	1.44E-4	4.46E-5
230	110	1.29E-4	4.04E-5	1.40E-4	4.36E-5
230	120	1.33E-4	4.05E-5	1.36E-4	4.16E-5
230	130	1.22E-4	3.97E-5	1.33E-4	4.32E-5
230	140	1.25E-4	3.94E-5	1.35E-4	4.27E-5
240	40	1.05E-4	4.72E-5	1.12E-4	5.05E-5
240	50	1.98E-4	9.17E-5	1.05E-4	4.85E-5

Table C.4: The run2b and run2a scale factors used for gluon/gluon (gg) fusion and quark/anti-quark ($q\bar{q}$) Monte Carlo events.

Appendix D

Comparison of data and background estimate for run2a and run2b

D.1 Run2b Analysis Variable Plots

D.1.1 Lepton and $\not\!\!E_T$ kinematic variables

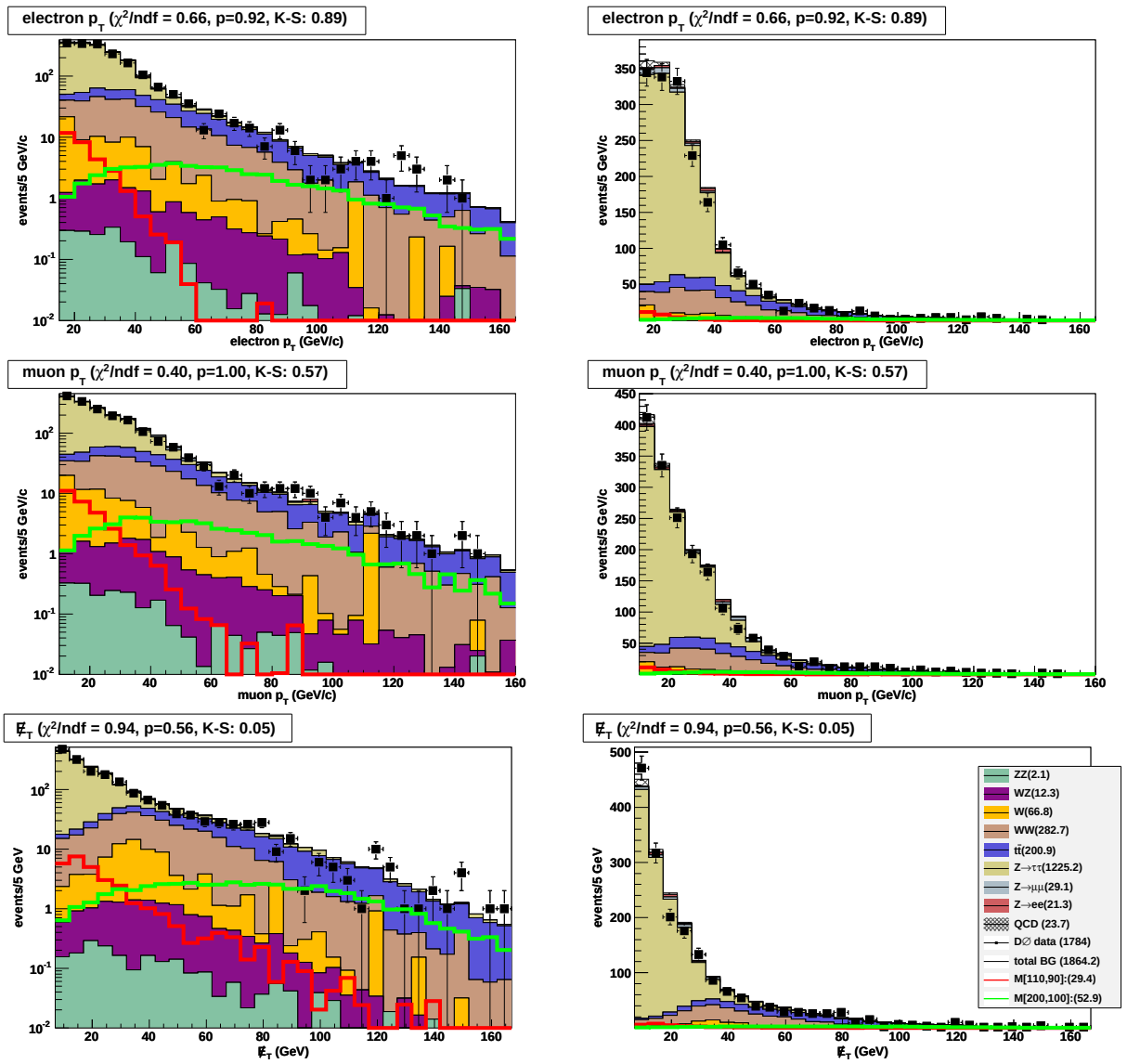

Figure D.1: The transverse momentum of the electron (top) and muon (middle) and the missing transverse energy (bottom) for the run2b samples. M[200,100] (green) and M[110,90] (red) are the hard and soft benchmark signal samples. The DØ data event counts and the estimated events for the backgrounds and signal benchmarks are given in the legend. The legend also included event counts for each of the samples. The events shown represent run2b data and Monte Carlo.

D.1.2 Lepton and $\not\!\!E_T$ topological variables

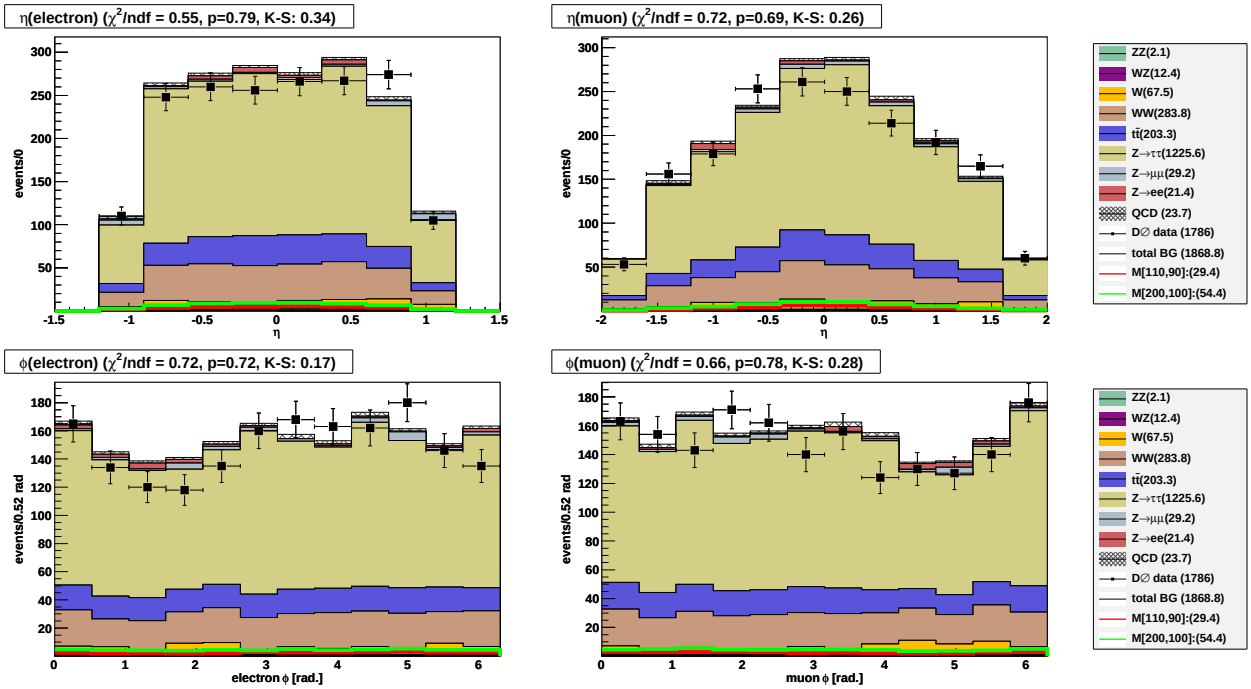

Figure D.2: Electron (left) and muon (right) η (top) and ϕ (bottom). M[200,100] (green) and M[110,90] (red) are the hard and soft benchmark signal samples. The DØ data event counts and the estimated events for the backgrounds and signal benchmarks are given in the legend. The legend also included event counts for each of the samples. The events shown represent run2b data and Monte Carlo.

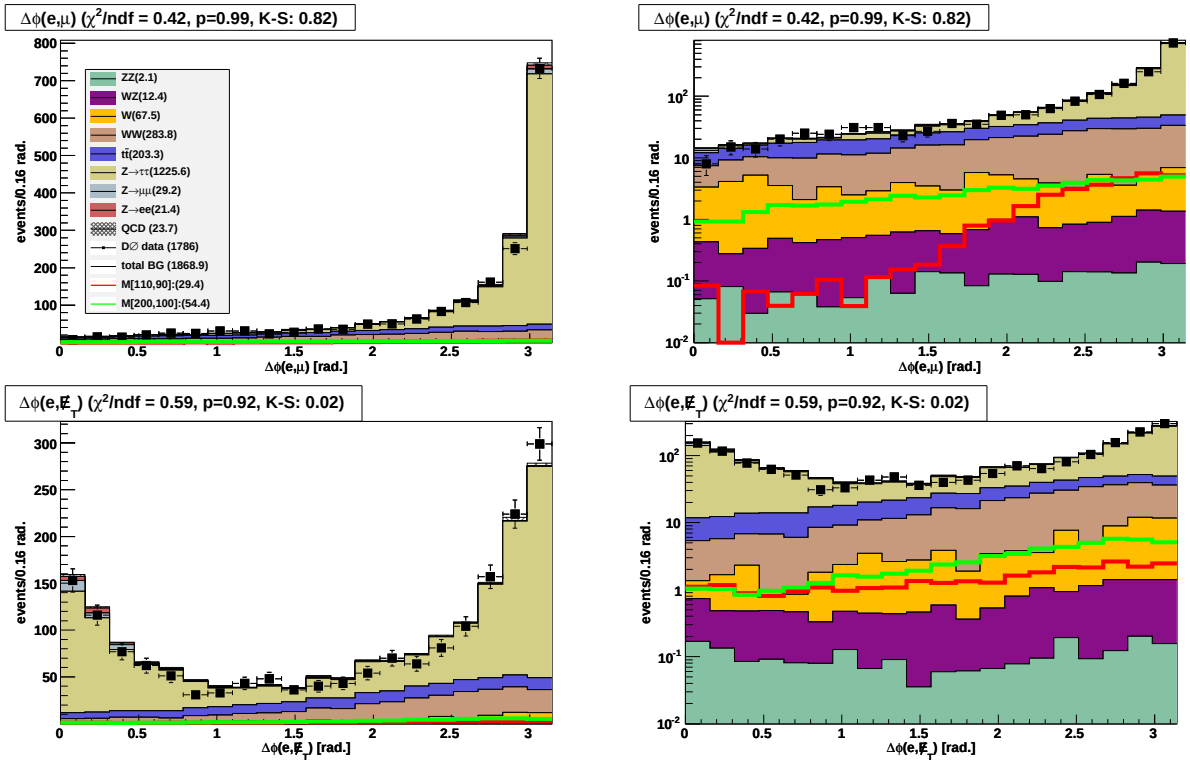

Figure D.3: The transverse plane opening angles between the electron and the muon (top) and the electron and the missing transverse energy (bottom). M[200,100] (green) and M[110,90] (red) are the hard and soft benchmark signal samples. The DØ data event counts and the estimated events for the backgrounds and signal benchmarks are given in the legend. The legend also included event counts for each of the samples. The events shown represent run2b data and Monte Carlo.

D.1.3 Jets

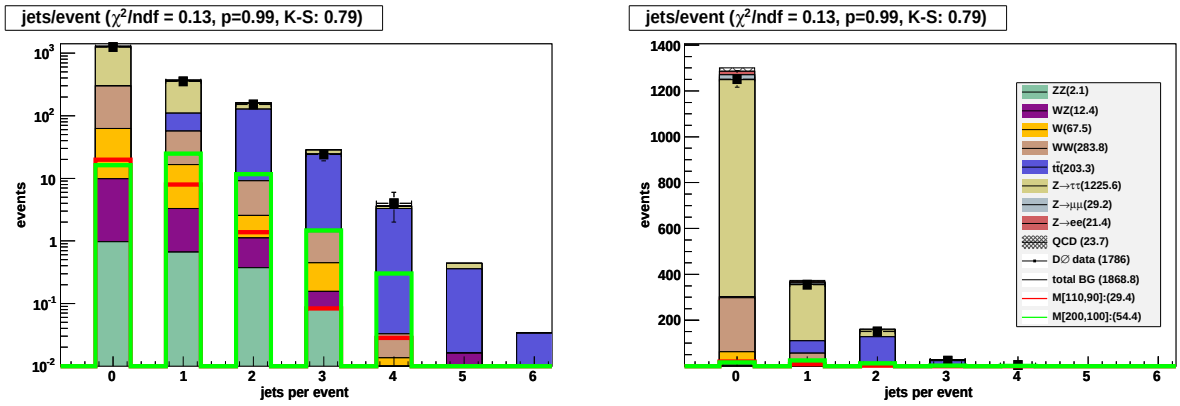

Figure D.4: The number of jets in log (left) and linear (right) scale. M[200,100] (green) and M[110,90] (red) are the hard and soft benchmark signal samples. The DØ data event counts and the estimated events for the backgrounds and signal benchmarks are given in the legend. The events shown represent run2b data and Monte Carlo.

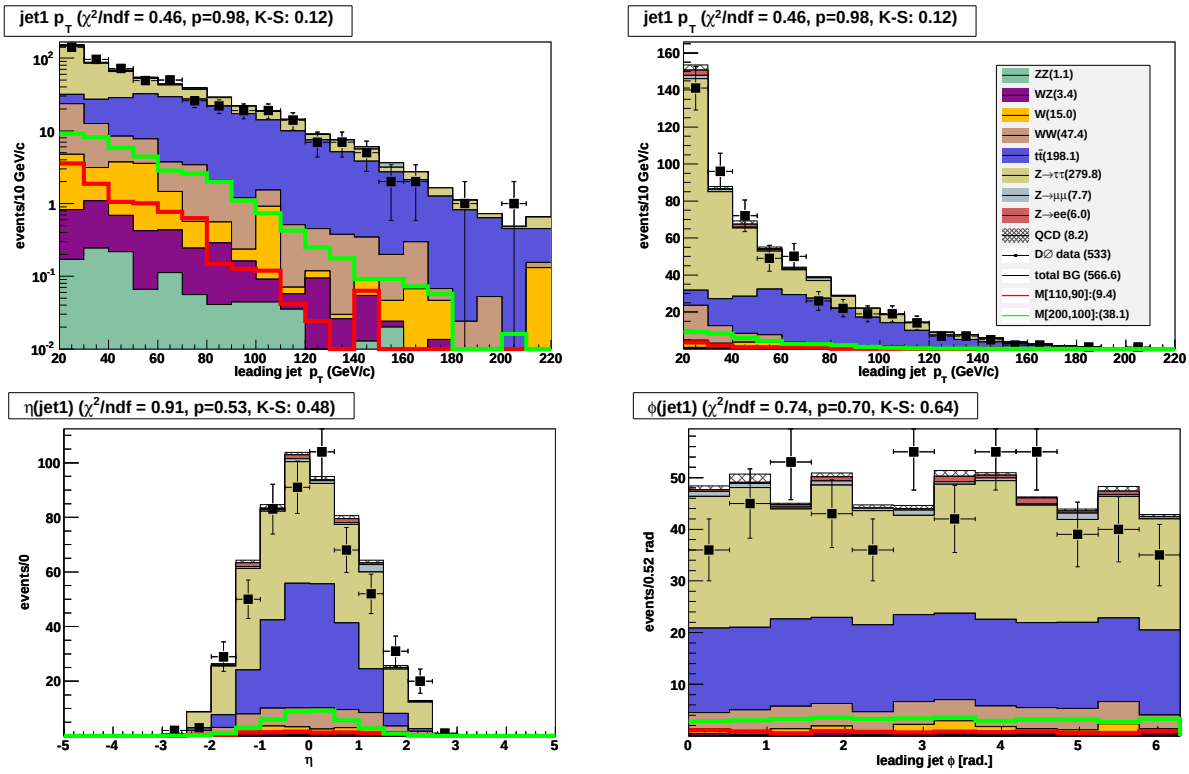

Figure D.5: The transverse momentum of the leading jet (top) in log (left) and linear (right) scale. Also shown are the leading jet η (bottom left) and ϕ (bottom right) distributions. M[200,100] (green) and M[110,90] (red) are the hard and soft benchmark signal samples. The DØ data event counts and the estimated events for the backgrounds and signal benchmarks are given in the legend. The events shown represent run2b data and Monte Carlo.

D.1.4 S_T and H_T

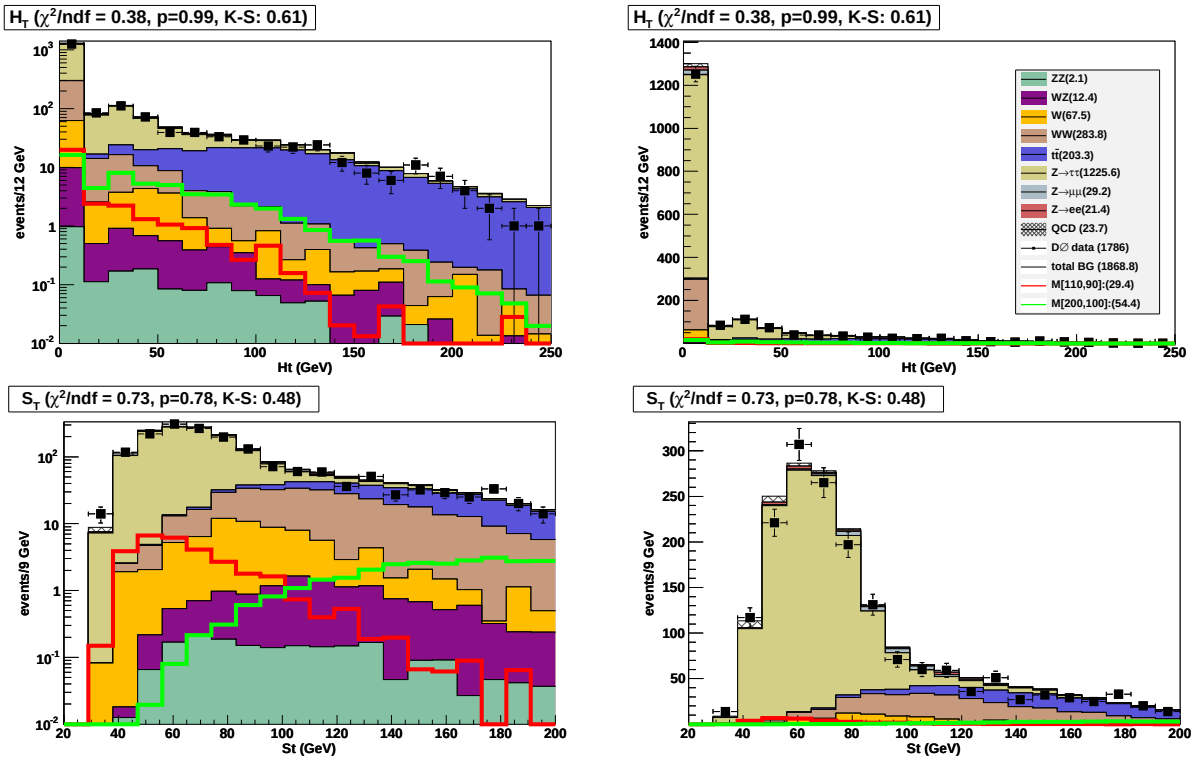

Figure D.6: H_T(top) and S_T (bottom) in log (left) and linear(right) scale. M[200,100] (green) and M[110,90] (red) are the hard and soft benchmark signal samples. The DØ data event counts and the estimated events for the backgrounds and signal benchmarks are given in the legend. The legend also included event counts for each of the samples. The events shown represent run2b data and Monte Carlo.

D.1.5 Luminosity

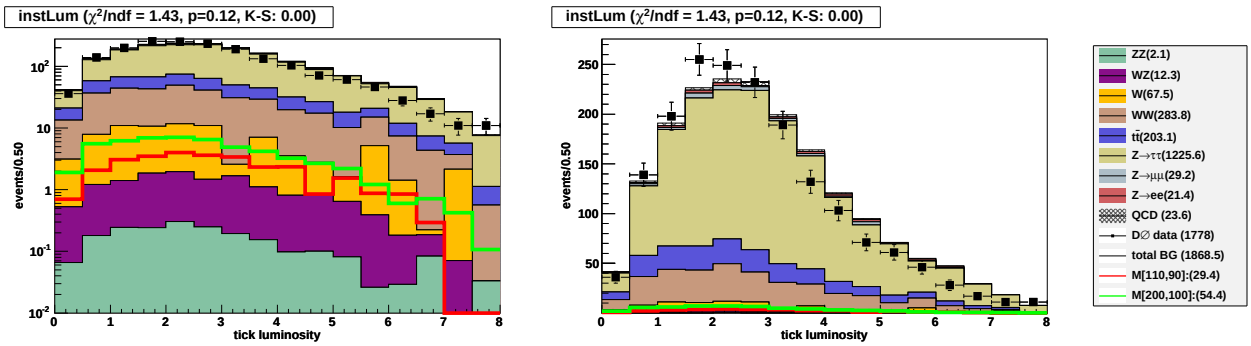

Figure D.7: Tick luminosity with log and linear scales for the combination data set. M[200,100] (green) and M[110,90] (red) are the hard and soft benchmark signal samples. The DØ data event counts and the estimated events for the backgrounds and signal benchmarks are given in the legend. The legend also included event counts for each of the samples. The events shown represent run2b data and Monte Carlo.

D.2 Run2b Analysis Variable Plots

D.2.1 Lepton and $\not\!\!E_T$ kinematic variables

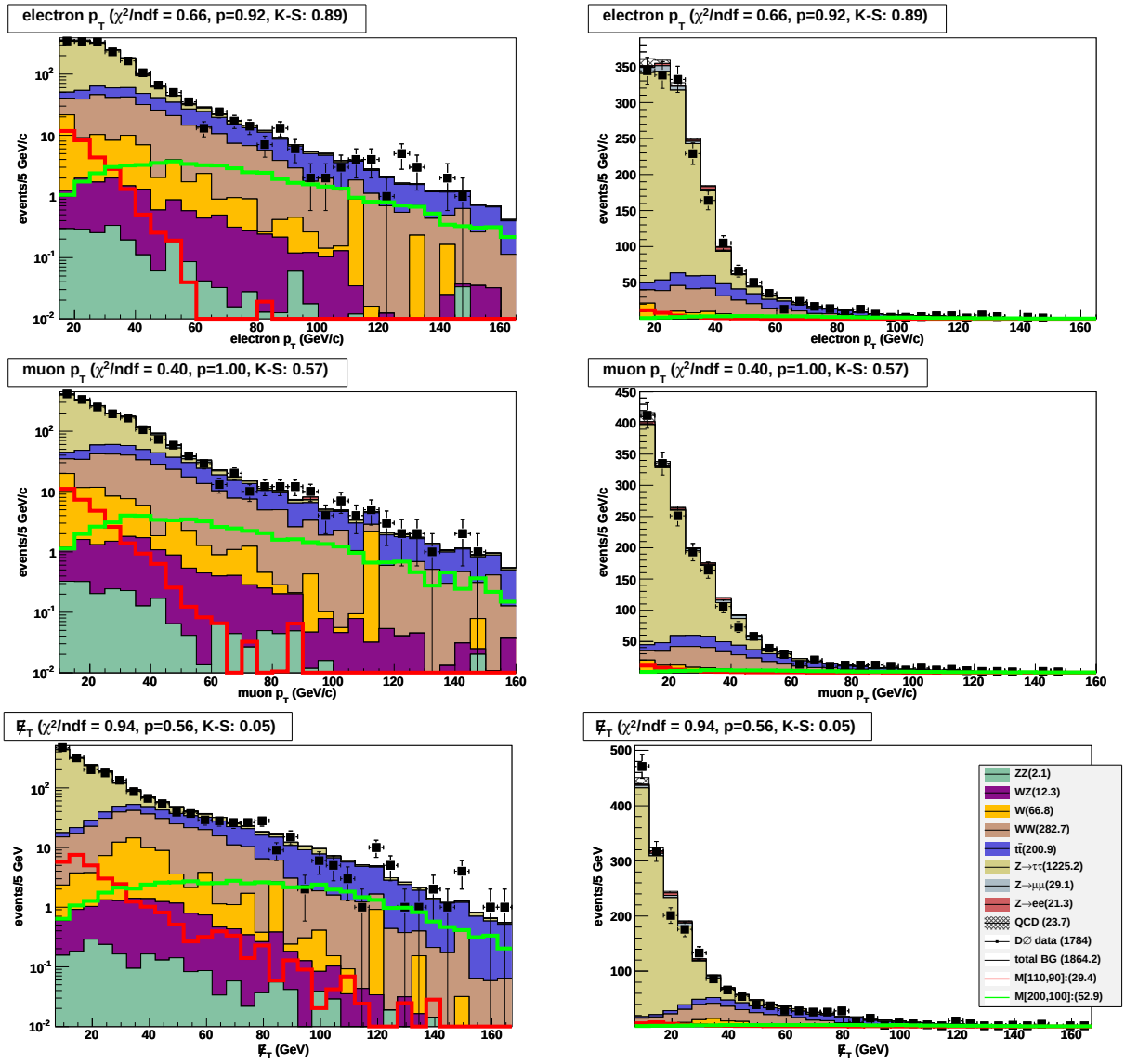

Figure D.8: The transverse momentum of the electron (top) and muon (middle) and the missing transverse energy (bottom) for the RunIIa samples. M[200,100] (green) and M[110,90] (red) are the hard and soft benchmark signal samples. The DØ data event counts and the estimated events for the backgrounds and signal benchmarks are given in the legend. The legend also included event counts for each of the samples. The events shown represent run2a data and Monte Carlo.

D.2.2 Lepton and $\not\!\!E_T$ topological variables

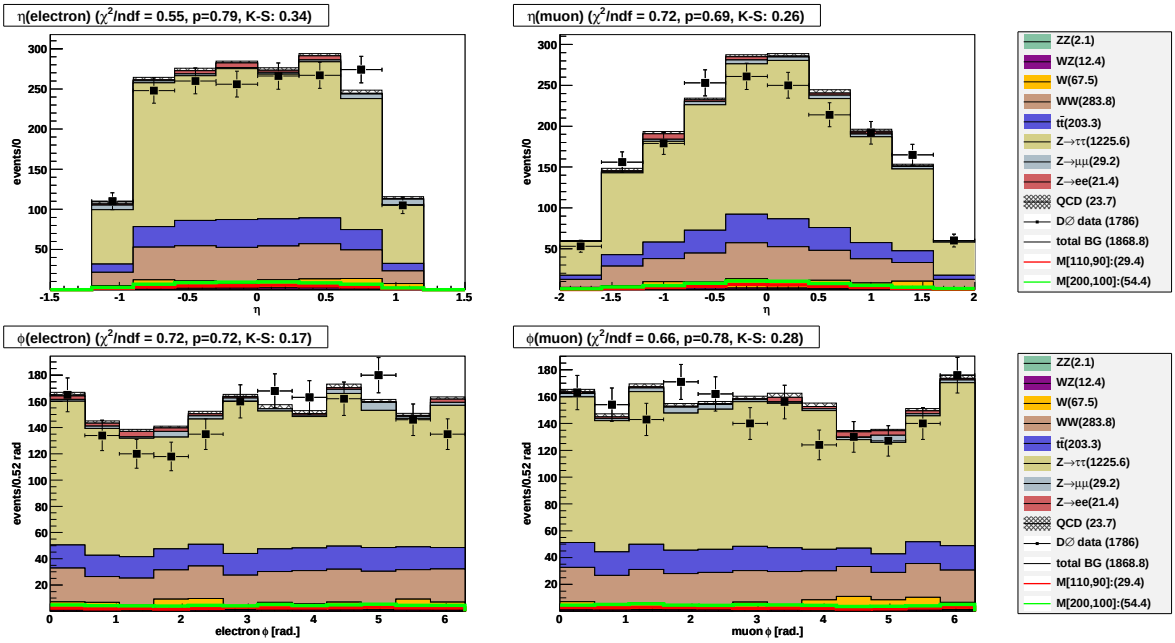

Figure D.9: Electron (left) and muon (right) η (top) and ϕ (bottom). M[200,100] (green) and M[110,90] (red) are the hard and soft benchmark signal samples. The DØ data event counts and the estimated events for the backgrounds and signal benchmarks are given in the legend. The legend also included event counts for each of the samples. The events shown represent run2a data and Monte Carlo.

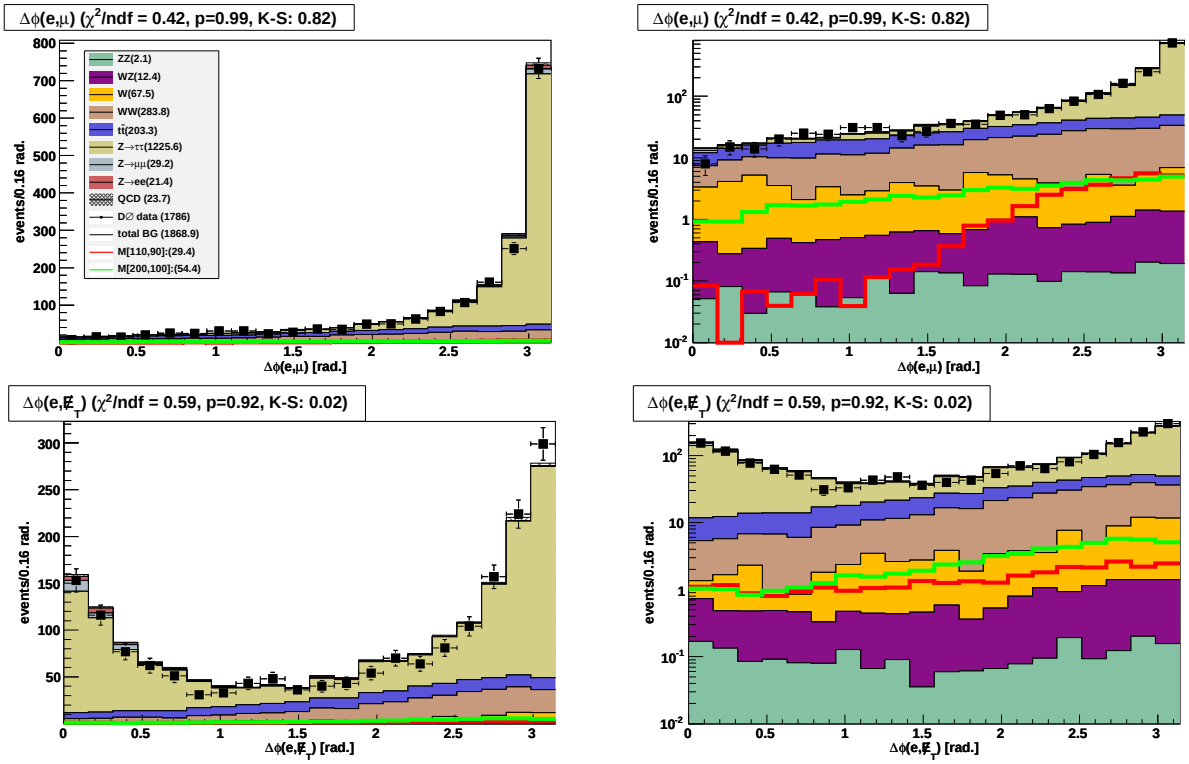

Figure D.10: The transverse plane opening angles between the electron and the muon (top) and the electron and the missing transverse energy (bottom). M[200,100] (green) and M[110,90] (red) are the hard and soft benchmark signal samples. The DØ data event counts and the estimated events for the backgrounds and signal benchmarks are given in the legend. The legend also included event counts for each of the samples. The events shown represent run2a data and Monte Carlo.

D.2.3 Jets

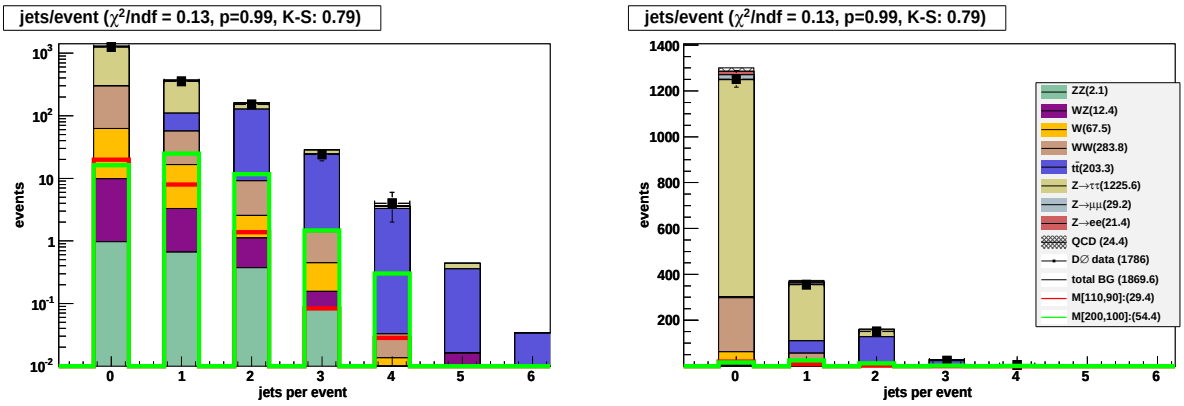

Figure D.11: The number of jets in log (left) and linear (right) scale. M[200,100] (green) and M[110,90] (red) are the hard and soft benchmark signal samples. The DØ data event counts and the estimated events for the backgrounds and signal benchmarks are given in the legend. The events shown represent run2a data and Monte Carlo.

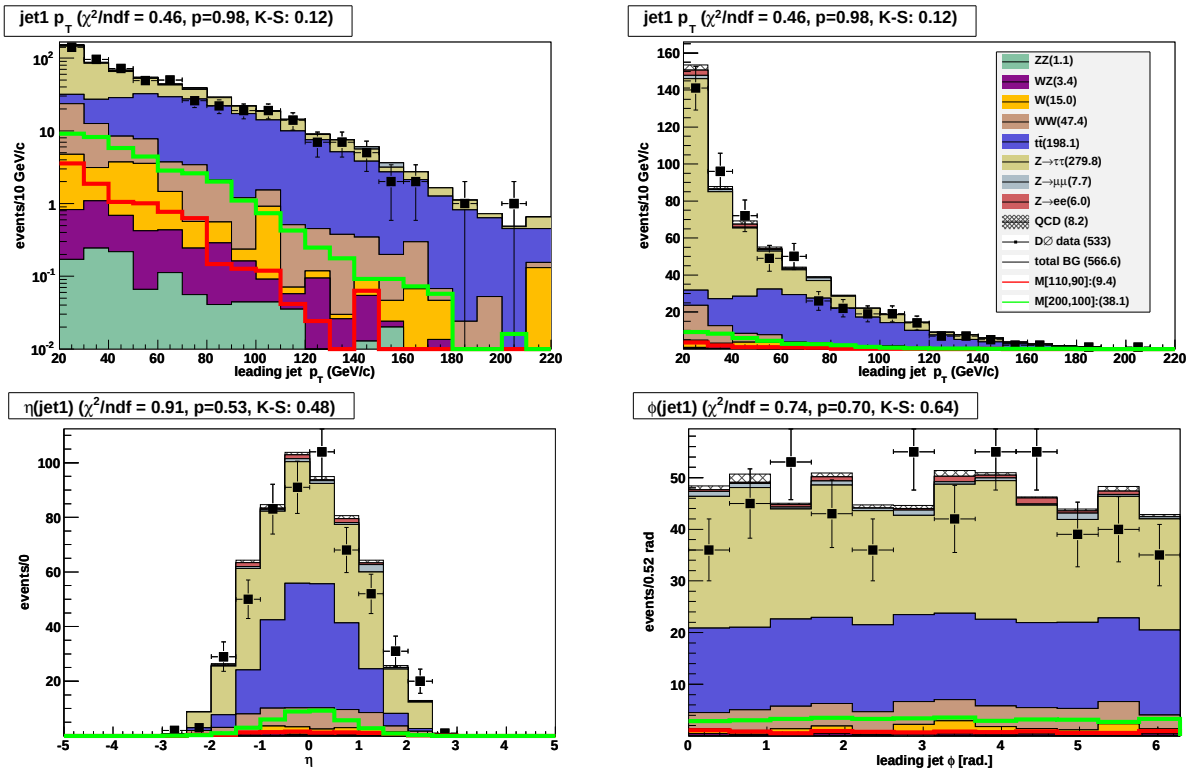

Figure D.12: The transverse momentum of the leading jet (top) in log (left) and linear (right) scale. Also shown are the leading jet η (bottom left) and ϕ (bottom right) distributions. M[200,100] (green) and M[110,90] (red) are the hard and soft benchmark signal samples. The DØ data event counts and the estimated events for the backgrounds and signal benchmarks are given in the legend. The events shown represent run2a data and Monte Carlo.

D.2.4 S_T and H_T

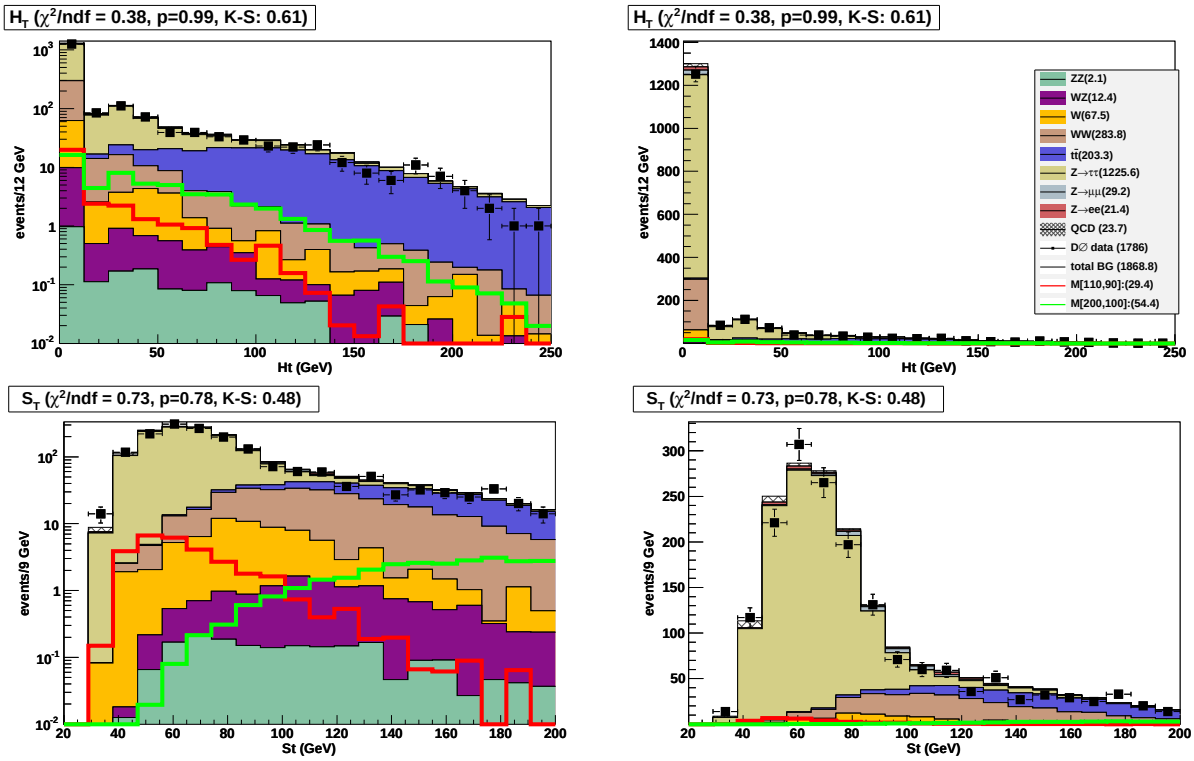

Figure D.13: H_T(top) and S_T (bottom) in log (left) and linear(right) scale. M[200,100] (green) and M[110,90] (red) are the hard and soft benchmark signal samples. The DØ data event counts and the estimated events for the backgrounds and signal benchmarks are given in the legend. The legend also included event counts for each of the samples. The events shown represent run2a data and Monte Carlo.

D.2.5 Luminosity

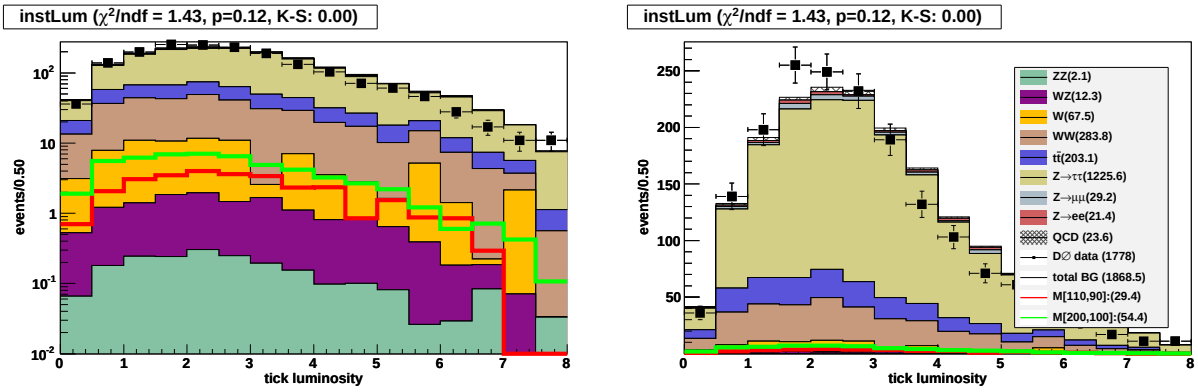

Figure D.14: Tick luminosity with log and linear scales for the combination data set. M[200,100] (green) and M[110,90] (red) are the hard and soft benchmark signal samples. The DØ data event counts and the estimated events for the backgrounds and signal benchmarks are given in the legend. The legend also included event counts for each of the samples. The events shown represent run2a data and Monte Carlo.

Appendix E

The CL_S Method

Though CL_s can be thought of as an acronym for Confidence Level for a signal, it originally appeared as the notation Junk used for the figure of merit when he introduced this method for calculating confidence levels [76]. Several features make the CL_s method useful for new physics searches. It is designed to work with low statistics. Results from multiple experiments can be combined easily. Also, it can incorporate correlated and uncorrelated systematic uncertainties for both the signal and background estimates.

E.1 95% Upper-limit Cross Section

When looking for a new physics signal, we want to check how well our expected signal plus expected background hypothesis, which we will denote $S + B$, describes the observed data, which we will denote D_{obs}. Because we usually have many more Monte Carlo events to describe S + B than we have data events to describe D_{obs}, we flip the question around and ask "What is the probability of observing D_{obs} events if we assume our hypothesis, $S + B$, is true. Mathematically we state this as $P(D_{obs}|S + B)$ and we answer it using Poisson

statistics

$$P(D_{obs}|S+B) \;=\; \frac{(S+B)^{D_{obs}}\; e^{-(S+B)}}{D_{obs}!}. \tag{E.1}$$

To convert our question and answer into a probability interval, we ask "What is the probability of observing D_{obs} or fewer events if we assume that our hypothesis S+B is true?". This question and the answer in mathematics are

$$P(D \leq D_{obs}|S+B) \;=\; \sum_{D=0}^{D_{obs}} P(D|S+B) \tag{E.2}$$

where D is an integer and $0 \leq D \leq D_{obs}$.

Since $P(D \leq D_{obs}|S+B)$ is the probability of observing D_{obs} or fewer events assuming $S+B$ is true, then $1 - P(D \leq D_{obs}|S+B)$ is the probability of observing more than D_{obs} events assuming $S+B$. We call the probability

$$P(D > D_{obs}|S+B) = 1 - P(D \leq D_{obs}|S+B) \tag{E.3}$$

an upper-limit confidence level. In new physics searches it is customary to state the 95% upper-limit confidence level so our task is to find S such that $P(D > D_{obs}|S+B) \gtrsim 0.95$.

E.2 The CL_s Confidence Interval

The upperlimit confidence level we defined previously, $P(D > D_{obs}|S+B) \gtrsim 0.95$, is a true "frequentist" confidence level[1], but for $S+B$ not S. For $S+B$, this confidence

[1]Frequentists view confidence intervals as a way of stating the confidence that the true value of the estimated parameter is contained within the stated range of values. This is philosophically different from Bayesians who prefer to view statistics as a statement of their degree of belief and state credible intervals

interval has the feature that in cases where D_{obs} fluctuates below the expected background, the existence of the background actually improves the exclusion confidence of the signal. If D_{obs} fluctuates low enough, even a very small signal can be excluded with high degree of confidence. The CL_s method was introduced to deal with precisely this effect.

The CL_s method defines $CL_{s+b} = P(D \leq D_{obs}|S+B)$. It also introduces

$$CL_b = P(D \leq D_{obs}|B) \tag{E.4}$$

where $P(D \leq D_{obs}|B)$ is the probability of observing D_{obs} or fewer events assuming that the background hypothesis, B, is true. The figure of merit CL_s is given by

$$CL_s = \frac{CL_{s+b}}{CL_b} = \frac{P(D \leq D_{obs}|S+B)}{P(D \leq D_{obs}|B)}. \tag{E.5}$$

Dividing by CL_b protects against fluctuations in D_{obs}. CL_s is considered a semi-frequentist method because it does not represent a true frequentist confidence level but instead a more conservative one.

rather than confidence intervals.

E.3 CL_s and Multiple Channels

The CL_s method described above is for single channel experiments. CL_s can also state the confidence interval for the results from multiple channels, which can be the results of several experiments, the bins of the histogram of the discriminating variable for a single experiment, or a combination of the two. To calculate CL_s directly for multiple channels, one must sum the product of the probabilities for each channel over all possible outcomes in all channels:

$$CL_{s+b} = \sum_{D_1=0}^{D_{obs,1}} \cdots \sum_{D_N=0}^{D_{obs,N}} \prod_{n=1}^{N} \frac{(S_n + B_n)^{D_n}\ e^{-(S_n+B_n)}}{D_n!} \tag{E.6}$$

$$CL_b = \sum_{D_1=0}^{D_{obs,1}} \cdots \sum_{D_N=0}^{D_{obs,N}} \prod_{n=1}^{N} \frac{(B_n)^{D_n}\ e^{-B_n}}{D_n!} \tag{E.7}$$

$$CL_s = \frac{CL_{s+b}}{CL_b} \tag{E.8}$$

where N is the number of channels, $D_{obs,n}$ is the number of observed events in channel n, and D_n is a possible outcome for the n_{th} channel. This calculation is not always possible since the number of terms is of the order $\mathcal{O}(m^n)$ for n channels with m outcomes[2]. An alternative is to repeat the calculation of $P(D|S+B)$, eqn. E.1, for each $\tilde{D}$ in an ensemble of m samples, $\tilde{D}_0 \ldots \tilde{D}_m$ created as fluctuations from $S+B$ and also to repeat the calculation of $P(D|B)$, eqn. E.4, for each $\tilde{D}'$ in an ensemble of m samples, $\tilde{D}'_0 \ldots \tilde{D}'_m$, created as fluctuations from B. Then CL_{s+b} and CL_B are given by the percentages of the fluctuations for which $P(\tilde{D}|S+B) < P(D_{obs}|S+B)$ and $P(\tilde{D}'|B) < P(D_{obs}|B)$ respectively.

[2]Junk agreed via email that the number of terms is actually $\mathcal{O}(m^n)$ for n channels and m outcomes not $\mathcal{O}(n^m)$ as he wrote in his paper[76].

E.4 The Expected Confidence Level, $\langle CL_s \rangle$

The expected confidence level, $\langle CL_s \rangle$, states the expected value of CL_s if the background only hypothesis, B, is true. $\langle CL_s \rangle$, which is independent of the observed data, is used as a figure of merit for the signal sensitivity of an experiment and it is used for this purpose in this analysis. To calculate $\langle CL_s \rangle$, the $P(D \leq D^n_{obs}|S+B)$ and $P(D \leq D^n_{obs}|B)$ are calculated for each D^n_{obs} in an ensemble of N samples, $D^1_{obs} \ldots D^n_{obs} \ldots D^N_{obs}$, created as fluctuations from B. The average values of these calculations give $\langle CL_{s+b} \rangle$ and $\langle CL_b \rangle$. The expected confidence level is

$$\langle CL_s \rangle = \frac{\langle CL_{s+b} \rangle}{\langle CL_b \rangle}. \tag{E.9}$$

Appendix F

Additional Trigger Information

F.1 Trigger Periods

luminosity epoch	trigger version	luminosity (pb^{-1})
run2a	pre-v12	129.21
	v12	231.83
	v13	379.14
	v14	339.18
run2b		
pre-shutdown	v15	1222.46
post-shutdown	v15	401.07
	v16	2658.13

Table F.1: The integrated luminosity by trigger list. The reported luminosity is the amount after the run level but before the event level data quality corrections have been applied.

F.1.1 Single EM trigger lists

run2a Single EM Triggers			
E1_ISH30	E3_T15SH20	E8_SHT10_ITK10	E19_ISHT15_TK13
E1_ISHT15_TK13	E3_T25VL30	E8_SHT15_TK13	E19_ISHT22
E1_ISHT22	E4_ISH30	E8_SHT20	E19_SH35
E1_L50	E4_ISHT15_TK13	E8_T13L15	E19_SHT25
E1_L70	E4_ISHT22	E8_T13SH15	E19_T13SHT15
E1_NC90	E4_SH30	E8_T15L20	E19_T15SH20
E1_SH30	E4_SH35	E9_IT10SHT10	E20_ISH30
E1_SH35	E4_SHT15_TK13	E9_IT7SHT8	E20_ISHT15_TK13
E1_SHT15_TK13	E4_SHT20	E9_SH30	E20_ISHT22
E1_SHT20	E4_SHT22	E9_SHT10_ITK10	E20_IT10SHT10
E1_SHT22	E4_SHT25	E9_SHT15_TK13	E20_SH35
E1_SHT25	E4_T13L15	E9_SHT20	E20_SHT12_ITK10
E1_T13L15	E4_T13SH15	E9_SHT8_ITK10	E20_SHT25
E1_T13SH15	E4_T13SHT15	E9_T13L15	E20_T13SHT15
E1_T13SHT15	E4_T15L20	E9_T13SH15	E20_T15SH20
E1_T15L20	E4_T15SH20	E9_T15L20	E21_ISH30
E1_T15SH20	E4_T25VL30	E13_ISH30	E21_ISHT15_TK13
E1_T25VL30	E5_SH30	E13_ISHT15_TK13	E21_ISHT22
E1_VL70	E5_SHT15_TK13	E13_ISHT22	E21_IT10SHT10
E13_ISH30	E5_SHT20	E13_SH35	E21_SHT12_ITK10
E13_ISHT15_TK13	E5_SHT22	E13_SHT25	E21_SHT25
E13_ISHT22	E5_T13L15	E13_T13SHT15	E21_T13SHT15
E13_SH35	E5_T13SH15	E13_T15SH20	E21_T15SH20
E13_SHT25	E5_T15L20	E17_ISH30	EM_HI_2EM5
E13_T13SHT15	E6_SH30	E17_ISHT15_TK13	EM_HI_2EM5_EMFR8
E13_T15SH20	E6_SHT15_TK13	E17_ISHT22	EM_HI_2EM5_F0
E17_ISH30	E6_SHT20	E17_IT10SHT10	EM_HI_2EM5_SH
E17_ISHT15_TK13	E6_SHT22	E17_SH35	EM_HI_2EM5_SH_TR
E17_ISHT22	E6_T13L15	E17_SHT12_ITK10	EM_HI_2EM5_TR
E17_IT10SHT10	E6_T13SH15	E17_SHT25	EM_HI_EMFR8
E17_SH35	E6_T15L20	E17_T13SHT15	EM_HI_F0
E17_SHT12_ITK10	E7_SH30	E17_T15SH20	EM_HI_SH_TR
E17_SHT25	E7_SHT15_TK13	E18_ISH30	EM_HI_TR
E17_T13SHT15	E7_SHT20	E18_ISHT15_TK13	EM_MX_EMFR8
E17_T15SH20	E7_SHT22	E18_ISHT22	EM_MX_F0
E18_ISH30	E7_T13L15	E18_SH35	EM_MX_SH
E18_ISHT15_TK13	E7_T13SH15	E18_SHT25	EM_MX_SH_TR
E18_ISHT22	E7_T15L20	E18_T13SHT15	EM_MX_TR
E18_SH35	E8_IT10SHT10	E18_T15SH20	
E18_SHT25	E8_SH30	E19_ISH30	

Table F.2: The list of triggers included in the run2a "single EM triggers OR".

run2b Single EM Triggers		
E1_ISH30	TE1_LH2ISHT17T14_NOLUM	TE3_SHT25
E1_ISHT15_TK13	TE1_LH2L70	TE3_SHT25_NOLUM
E1_ISHT22	TE1_LH2L70_NOLUM	TE3_SHT50
E1_L70	TE1_LH2SH27	TE3_SHT50_NOLUM
E1_L80	TE1_LH2SH27_NOLUM	TE3_T13SHT15
E1_LH2ISH24	TE1_SH35	TE3_T14LH2SH17
E1_LH2ISHT17T14	TE1_SH60	TE3_T14LH2SH17_NOLUM
E1_LH2L70	TE1_SH60_NOLUM	TE3_T15SH20
E1_LH2SH27	TE1_SHT25	TE4_ISH30
E1_LH3ISH25	TE1_SHT25_NOLUM	TE4_ISHT15_TK13
E1_LH3SH27	TE1_SHT50	TE4_ISHT22
E1_SH35	TE1_SHT50_NOLUM	TE4_L70
E1_SH60	TE1_T13SHT15	TE4_L80
E1_SHT25	TE1_T14LH2SH17	TE4_L80_NOLUM
E1_SHT27	TE1_T14LH2SH17_NOLUM	TE4_LH2ISH24
E1_SHT27_NOLUM	TE1_T15SH20	TE4_LH2ISH24_NOLUM
E1_SHT50	TE2_ISH30	TE4_LH2ISHT17T14
E1_T13SHT15	TE2_ISHT15_TK13	TE4_LH2ISHT17T14_NOLUM
E1_T14LH2SH17	TE2_ISHT22	TE4_LH2L70
E1_T15SH20	TE2_L70	TE4_LH2L70_NOLUM
E2_ISH30	TE2_L80	TE4_LH2SH27
E2_ISHT15_TK13	TE2_LH2ISH24	TE4_LH2SH27_NOLUM
E2_ISHT22	TE2_LH2ISHT17T14	TE4_SH35
E2_L70	TE2_LH2L70	TE4_SH60
E2_L80	TE2_LH2SH27	TE4_SHT25
E2_LH2ISH24	TE2_SH35	TE4_SHT25_NOLUM
E2_LH2ISHT17T14	TE2_SH60	TE4_SHT50
E2_LH2L70	TE2_SHT25	TE4_SHT50_NOLUM
E2_LH2SH27	TE2_SHT50	TE4_T13SHT15
E2_LH3ISH25	TE2_T13SHT15	TE4_T14LH2SH17
E2_LH3SH27	TE2_T14LH2SH17	TE4_T14LH2SH17_NOLUM
E2_SH35	TE2_T15SH20	TE4_T15SH20
E2_SH60	TE3_ISH30	TE5_ISH30
E2_SHT25	TE3_ISHT15_TK13	TE5_ISHT15_TK13
E2_SHT27	TE3_ISHT22	TE5_ISHT22
E2_SHT50	TE3_L70	TE5_L70
E2_T13SHT15	TE3_L80	TE5_L80
E2_T14LH2SH17	TE3_L80_NOLUM	TE5_LH2ISH24
E2_T15SH20	TE3_LH2ISH24	TE5_LH2ISHT17T14
TE1_ISH30	TE3_LH2ISH24_NOLUM	TE5_LH2L70
TE1_ISHT15_TK13	TE3_LH2ISHT17T14	TE5_LH2SH27
TE1_ISHT22	TE3_LH2ISHT17T14_NOLUM	TE5_SH35
TE1_L70	TE3_LH2L70	TE5_SH60
TE1_L80	TE3_LH2L70_NOLUM	TE5_SHT25
TE1_L80_NOLUM	TE3_LH2SH27	TE5_SHT50
TE1_LH2ISH24	TE3_LH2SH27_NOLUM	TE5_T13SHT15
TE1_LH2ISH24_NOLUM	TE3_SH35	TE5_T14LH2SH17
TE1_LH2ISHT17T14	TE3_SH60	TE5_T15SH20

Table F.3: The list of triggers included in the run2b "single EM triggers OR".

F.2 Single muon trigger lists

run2a Single Muon Triggers	
MU_W_L2M0_TRK3	MUH3_LM3_TK10
MU_W_L2M0_TRK10	MUH3_LM6_TK12
MU_W_L2M3_TRK10	MUH4_LM15
MU_W_L2M5_TRK10	MUH4_TK10
MUH1_ILM15_a	MUH6_LM15
MUH1_ILM15_b	MUH6_TK10
MUH1_ITLM10_a	MUH6_TK12_TLM12_a
MUH1_ITLM10_b	MUH6_TK12_TLM12_b
MUH1_LM15	MUH7_LM15
MUH1_TK10	MUH7_TK10
MUH1_TK12	MUH7_TK12_h10
MUH1_TK12_TLM12_a	MUH7_TK12_h8
MUH1_TK12_TLM12_b	MUH8_ITLM10
MUH2_LM10_TK12	MUH8_TK12_TLM12
MUH2_LM3_TK12	MUW_A_L2M3_TRK10
MUH2_LM6_TK12	MUW_W_L2M3_TRK10
MUH3_LM10_TK12	MUW_W_L2M5_TRK10

Table F.4: The list of triggers included in the run2a "single muon triggers OR".

run2b Single Muon Triggers	
MUHI1_ITLM10_a	MUHI3_ILM15
MUHI2_ITLM10_a	MUHI1_ITLM10_b
MUHI2_ITLM10_b	MUHI1_ILM10
MUHI1_ILM15	MUHI1_TLM12
MUHI2_ILM10	MUHI2_TLM12
MUHI2_ILM15	MUHI1_MM10
MUHI1_TK12_TLM12	MUHI1_TMM10
MUHI2_TK12_TLM12	MUHI2_MM10
MUHI3_TK12_TLM12	MUHI1_TMM10
MUHI3_ITLM10	MUHI2_TMM10

Table F.5: The list of triggers included in the run2b "single muon triggers OR".